NMR methods for the characterization of mass transport and reaction processes in porous materials

Dissertation zur Erlangung des Doktorgrades der Naturwissenschaften

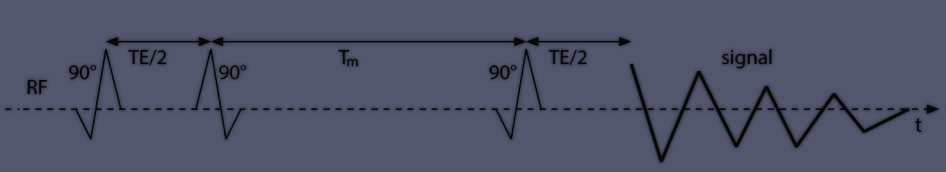

von
Mojtaba Mirdrikvand

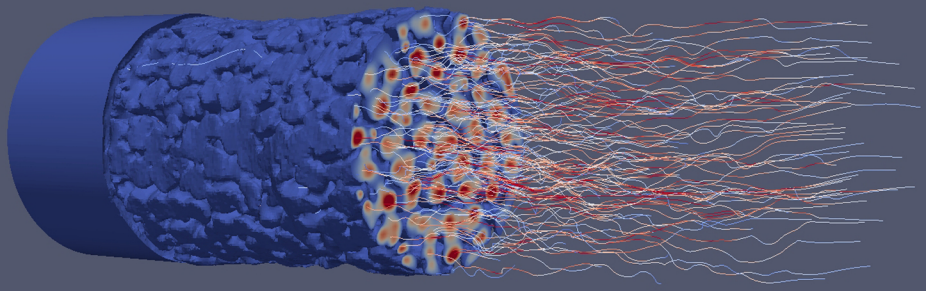

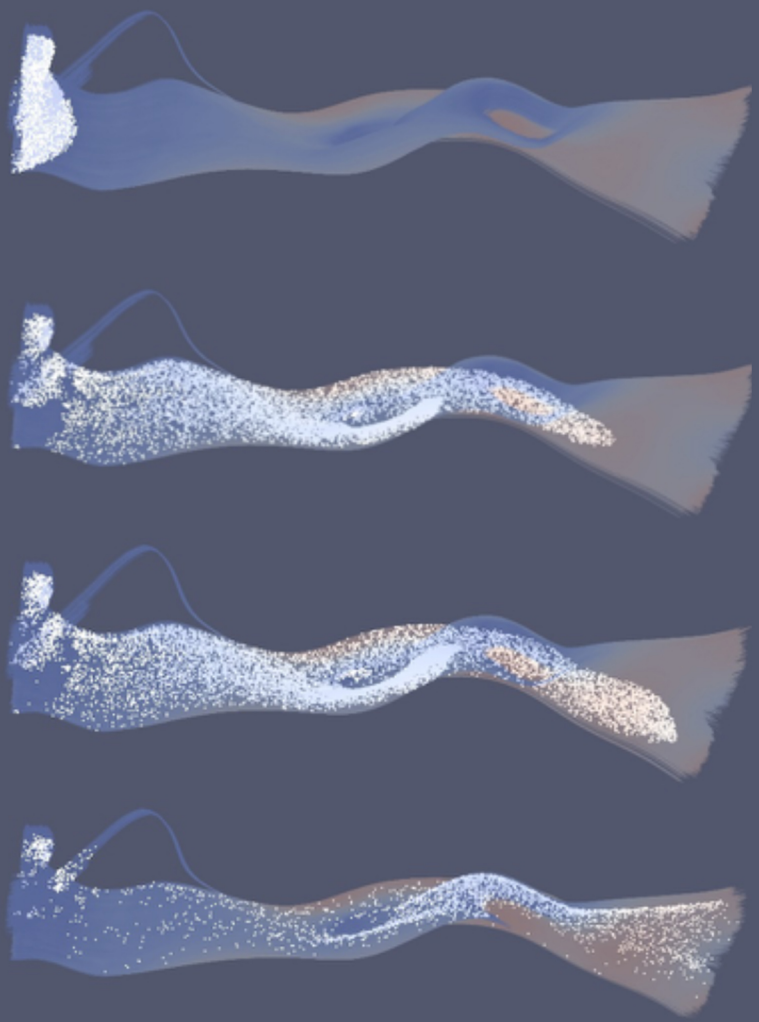

vorgelegt dem Fachbereich 02
(Biologie/Chemie)
der Universität Bremen

Bremen, 2020

NMR methods for the characterization of mass transport and reaction processes in porous materials

Dissertation

zur Erlangung des Doktorgrades der Naturwissenschaften

- Doctor rerum naturalium -

vorgelegt

dem Fachbereich 02 (Biologie/Chemie)

der Universität Bremen

von

Mojtaba Mirdrikvand, Master of Science,

geboren am 14. Juni 1989 in Andimeshk, Iran

Bremen, 2020

Gutachter/-innen:

Herr Priv.-Doz. Dr. Wolfgang Dreher
Arbeitsgruppe in-vivo-MR, FB Chemie/Biologie,
Universität Bremen

Dr. Carmine D'Agostino
School of Chemical engineering and Analytical Science,
University of Manchester

Weitere Mitglieder der Prüfungskommission:

Frau Prof. Dr. Petra Swiderek
FB Chemie/Biologie, Universität Bremen

Herr Prof. Dr. Jorg Thöming
FB Produktionstechnik, Universität Bremen

Herr Prof. Dr. Peter Spiteller
FB Chemie/Biologie, Universität Bremen

Promotionskolloquium am 17. 06. 2020

“The most personal is the most creative.”

Martin Scorsese

Abstract

NMR imaging (MRI) and localized NMR spectroscopy are powerful techniques for non-invasively characterizing fluids in opaque porous materials, particularly those used for gas phase catalytic reactions. Transport processes of gases such as diffusion, dispersion, and flow can be investigated by fast NMR methods despite short effective transverse relaxation times in porous media. This project aims at developing novel and optimizing existing NMR measurement methods for the non-invasive characterization of liquids and gases in porous materials. The project comprises the development and application of MRI, in particular diffusiometry and velocimetry techniques that allow investigations required for optimizing heterogeneous catalytic gas phase reactions. Thus, optimized NMR methods were applied to determine the local velocity fields, molecular diffusion, dispersion, and temperature.

Two major components of mass transport, diffusion and flow of gases, were investigated as preparatory studies for the analysis of gas phase reactions. To perform these investigations, measurement techniques were developed and optimized based on the specific demands in catalytic gas phase reactions taking place in monolithic structures. The measurements enabled the spatially resolved characterization of mass transport in such opaque systems by determining vital engineering parameters including temperature, composition of substances, velocity fields as well as molecular diffusion and dispersion of gas in catalyst supports. A 7-Tesla NMR imaging system (Bruker Biospec 70/20 USR) was used to develop methods and to perform measurements.

A spatially resolved NMR method for measuring the probability function of molecular displacement was developed to characterize diffusion and dispersion of thermally polarized gases in open-cell foams with different pore densities. The apparent diffusion coefficients and dispersion coefficients of thermally polarized methane were measured

under off-flow and flow conditions, respectively. Additionally, the influence of mechanical and diffusional dispersion at various flow rates (0.1-2.25 $L \cdot min^{-1}$, sample diameter: 25 mm) was investigated. The 3D MR velocimetry (MRV) measurements of gas flow in regular and irregular monolithic catalyst supports were conducted using an optimized spin-echo based phase-contrast MRV sequence. The obtained MRV data of thermally polarized methane gas were compared to numerical simulations performed for the identical samples. Finally, an optimized diffusion-weighted (DW) MRI technique was used for the *in situ* analysis of temperature in the catalyst supports. Using 3D DW-MRI to measure the temperature dependent diffusion coefficients of ethylene glycol, glycerol, and the temperature stable ionic liquid Pyr13 [TFSI] allowed to use capillaries filled with these liquids as NMR thermometers for a broad temperature range. Measurements were performed in a temperature range from 20 to 160 °C and allowed to obtain the axial temperature profiles in catalyst supports.

Zusammenfassung

NMR-Bildgebung (MRI) und lokalisierte NMR-Spektroskopie sind leistungsstarke Techniken zur nicht-invasiven Charakterisierung von Flüssigkeiten in opaken porösen Materialien, insbesondere solchen, die für katalytische Gasphasenreaktionen verwendet werden. Transportprozesse von Gasen wie Diffusion, Dispersion und Strömung können trotz kurzer effektiver transversaler Relaxationszeiten in porösen Medien mit schnellen NMR-Methoden untersucht werden. Ziel dieses Projektes ist die Entwicklung neuartiger und die Optimierung bekannter NMR-Messmethoden zur nicht-invasiven Charakterisierung von Flüssigkeiten und Gasen in porösen Materialien. Das Projekt umfasst die Entwicklung und Anwendung von Methoden der MRI, insbesondere zu Diffusions- und Geschwindigkeitsmessungen, die Untersuchungen zur Optimierung heterogener katalytischer Gasphasenreaktionen ermöglichen. So wurden optimierte NMR-Methoden zur Bestimmung der lokalen Geschwindigkeitsfelder, der molekularen Diffusion, der Dispersion und der Temperatur eingesetzt.

Zwei Hauptkomponenten des Massentransports, die Diffusion und die Strömung von Gasen, wurden als vorbereitende Studien für die Analyse von Gasphasenreaktionen untersucht. Zur Durchführung dieser Untersuchungen wurden Messtechniken entwickelt und optimiert, die die spezifischen Anforderungen bei katalytischen Gasphasenreaktionen in monolithischen Strukturen berücksichtigen. Die Messungen ermöglichten die ortsaufgelöste Charakterisierung des Massentransports in solchen opaken Systemen durch die Bestimmung wichtiger technischer Parameter wie Temperatur, Stoffzusammensetzung, Geschwindigkeit sowie molekulare Diffusion und Dispersion des Gases in den Katalysatorträgern. Zur Methodenentwicklung und zur Durchführung von Messungen wurde ein 7-Tesla-NMR-Tomograph (Bruker Biospec 70/20 USR) eingesetzt.

Eine ortsaufgelöste NMR-Methode zur Messung der Wahrscheinlichkeitsverteilung der Molekülverschiebung wurde entwickelt, um die Diffusion und Dispersion thermisch polarisierter Gase in offenzelligen Schäumen mit unterschiedlichen Porendichten zu charakterisieren. Die Diffusionskoeffizienten und Dispersionskoeffizienten von thermisch polarisiertem Methan wurden ohne und mit Fluss gemessen. Zusätzlich wurde der Einfluss der mechanischen und diffusionalen Dispersion bei verschiedenen Strömungsgeschwindigkeiten (0.1-2.25 L-min^{-1}, Probendurchmesser: 25 mm) untersucht. Die Messungen zur 3D-MR-Velocimetrie (MRV) von Gasströmen in regelmäßigen und unregelmäßigen monolithischen Katalysatorträgern wurden mit einer optimierten, auf einem Spin-Echo basierenden Phasenkontrast-MRV-Sequenz durchgeführt. Die an thermisch polarisiertem Methangas gemessenen MRV-Daten wurden mit für die identischen Proben durchgeführten numerischen Simulationen verglichen. Schließlich wurde eine optimierte diffusionsgewichtete (DW) MRI-Technik für die in-situ-Analyse der Temperatur in den Katalysatorträgern eingesetzt. Die 3D-DW-MRI-Messungen der temperaturabhängigen Diffusionskoeffizienten von Ethylenglykol, Glycerin und der temperaturstabilen ionischen Flüssigkeit Pyr13 [TFSI] ermöglichten es, mit diesen Flüssigkeiten gefüllte Kapillaren als NMR-Thermometer für einen breiten Temperaturbereich einzusetzen. Die Messungen wurden in einem Temperaturbereich von 20 bis 160 °C durchgeführt und ermöglichten, axiale Temperaturprofile in den Katalysatorträgern zu bestimmen.

Content

Preface

The present Ph.D. project entitled as 'NMR methods for the characterization of mass transport and reaction processes in porous materials' has been approved by the doctoral committee of the faculty of chemistry/biology at the University of Bremen in July 2017. The results of these investigations were obtained when I was an employee of the faculty as a research assistant from October 2016 to September 2019. The project aims at developing novel and optimizing existing NMR methods, including Magnetic Resonance Spectroscopic Imaging (MRSI), MR velocimetry (MRV), MR diffusiometry, and MR thermometry for the non-invasive characterization of thermally polarized gases in porous ceramics. The porous ceramics investigated in this project are mainly regular and irregular monolithic catalyst supports used in heterogeneously catalyzed gas phase reactions, such as methanation of CO or CO_2 or hydrogenation of ethylene. Liquids have also been investigated in some cases.

Being a chemical engineer, I have tried to answer some practical questions in the field of reaction engineering by developing NMR methods in an interdisciplinary group through learning NMR concepts and consequently finding potential solutions to investigate mass transport in heterogeneously catalyzed gas phase reactions. This work comprises both methodological developments and applications, in close cooperation with other colleagues in the graduate school supported by the German Research Foundation (DFG) in the frame of the Research Training Group GRK 1860 "Micro-, meso- and macro-porous nonmetallic Materials: Fundamentals and Applications" (MIMENIMA). The thesis is divided into seven chapters. The content of chapters 2, 3, and 5 have earlier been published by the author of this dissertation as the main contributor.

The basic principles of NMR are described in ***Chapter 1*** to help the readers who are not familiar with NMR better understand and follow the discussion and argumentation given in the next chapters. In addition, a brief overview on the necessity of investigating mass transport in the field of chemical engineering, such as diffusion, dispersion, flow, and temperature is given in this chapter.

Chapter 2 is intended to measure the most fundamental property of mass transport, effective diffusion in the absence of flow. An optimized pulsed field gradient stimulated echo (PFG-STE) pulse sequence with free volume selection is developed to investigate the propagator of thermally polarized methane gas within commercial monolithic catalyst supports, including open-cell foams and honeycombs. In this chapter, a clear effect of the type of monolith, its pore size and coating on the effective gas diffusion coefficient and the apparent tortuosity for a given observation time was found. The idea of developing such a local analysis is to extend the measurements to more complex flow conditions, i.e., flow of gas in the monoliths.

In ***Chapter 3*** a pore-scale analysis of axial and radial dispersion coefficients of the gas flow in macroporous foam monoliths using NMR-based displacement measurements is carried out. The influence of mechanical and diffusional dispersion at various flow rates in open-cell foams is also characterized. By observing the transition from diffusional dispersion to mechanically driven dispersion of gas, it is found that diffusional dispersion plays an important role, even at higher flow rates after a transition from Darcy to Darcy-Forchheimer regime. The comparative study between commercial foams shows the capacity of the optimized PFG-STE sequence in the investigation of morphological properties of open-cell foams such as open porosity, window size, and flow rate on gas dispersion.

Full field velocity mapping of thermally polarized gases in monolithic structures was performed in ***Chapter 4***. The NMR measurements aim at improving and validating numerical predictions for flow fields in monoliths. Regular and irregular monoliths were investigated by using an optimized phase contrast spin echo-based MRI sequence. Chapters 2 to 4 are complementary to the exhaustive analysis of mass transport in the monolithic catalyst supports both in macro- and micro-scale ranges.

A 3D DW-MRI approach is suggested for temperature measurements in heterogeneously catalyzed systems that occur at high temperature ranges in ***Chapter 5***. This approach introduces three liquids, ethylene glycol, glycerol, and the temperature stable ionic liquid Pyr_{13} [TFSI] (decomposition temperature 400 °C) as NMR thermometers to measure temperature profiles in catalyst supports in a broad temperature range (20-160 °C).

Some improvable aspects of each individual investigation explained in former chapters are discussed in ***Chapter 6***. Finally, two ideas for further investigation of mass transport in porous media are discussed in the outlook section (***Chapter 7***). The possibility of MRI of multiphase flow in porous media is discussed in the first part of the chapter. The obtained velocity fields for single-phase Newtonian and non-Newtonian liquids were compared to numerical simulations as a preparatory study to show the feasibility of the idea to extend the ongoing investigations in the future. Besides, NMR relaxation time measurements for supported catalysts used in methanation reaction are discussed. The results were obtained during a visit to the School of Chemical Engineering and Analytical Science at the University of Manchester in 2018. The idea of this investigation is to correlate relaxation times to the performance of supported catalysts as they are sensitive to their surrounding environment i.e., the interaction with pore walls.

Chapter 1

Introduction

1.1. NMR basics

NMR basics are introduced in this chapter. Three essential equations that allow understanding the principles behind an NMR measurement, Larmor equation, Curie's law, and Bloch equation are discussed. The introduction also covers the description of a simple spin-echo sequence to understand an NMR measurement using visualized and simplified schematic representations. Afterwards, NMR techniques for the investigation of mass transport in porous media are discussed; in our case, regular and irregular monolithic catalyst supports used in heterogeneously catalyzed gas phase reactions. Detailed descriptions of NMR principles can be found in the literature [1–4].

1.1.1. Nuclear spin and magnetic moment

In order to describe the properties of the nuclear spin angular momentum, quantum mechanics must be used. The spin exists as an inherent form of angular momentum carried by atomic nuclei [5], and can be described by the spin quantum number I, which is an integer multiple of $\frac{1}{2}$. In a magnetic field $\vec{B}_0 = (0,0,B_0)$, the component of the nuclear angular momentum in z-direction has only discrete values described by magnetic quantum number $m = -I, -I+1, \ldots, I-1, I$.

The magnitude of the nuclear angular momentum is given by

$$|L| = \sqrt{I(I+1)}\,\hbar \tag{1.1}$$

with the reduced Planck constant $\hbar = 6.5821 \cdot 10^{-16}$ eV·s.
The nuclear magnetic moment $\vec{\mu}$ is associated with the nuclear spin, where the gyromagnetic ratio γ is a characteristic quantity of the atomic nucleus.

$$\vec{\mu} = \gamma \vec{L} \tag{1.2}$$

In the present study, we focus on ^{1}H NMR based on two reasons. First, the ^{1}H atom is by far the most frequently existing atom in nature. The high abundance of ^{1}H in human cells has often been the basics for *in vivo* applications. This is also the case in many processes in the field of chemical engineering including reactions dealing with hydrogen containing materials. Second, ^{1}H has the largest gyromagnetic ratio of all stable isotopes which leads to a higher Signal-to-Noise ratio (SNR $\propto \gamma^3$). The gyromagnetic ratios of some nuclei are given in Table 1.1.

Table 1.1. Gyromagnetic ratios of nuclei used in NMR.

Nucleus	$\gamma / 2\pi$ **[MHz·T^{-1}]**
^{1}H	42.576
^{2}D	6.53593
^{3}He	-32.434
^{13}C	10.705
^{14}N	3.0766
^{15}N	-4.3156
^{17}O	-5.7716
^{19}F	40.0593
^{31}P	17.235

1.1.2. Atomic nucleus in a magnetic field

In a static magnetic field B_0, the nuclear spin precesses around the external magnetic field, since the external magnetic field exerts a torque on the magnetic moment. This phenomenon is called 'Larmor precession'.

The magnetic energy of the magnetic moment $\vec{\mu}$ in a magnetic field B_0 can be written as a function of magnetic moment

$$E = -\vec{\mu} \cdot \vec{B}_0 = -\gamma \, m \, \hbar \, B_0 \tag{1.3}$$

and the energy difference between the two states of a two-energy-level system ($I = \frac{1}{2}$) can be described by

$$\Delta E = \hbar \, \omega_0 = \hbar \cdot v_0 = \hbar \, \gamma \cdot B_0 \tag{1.4}$$

1.1.3. Macroscopic magnetization

The distribution of the magnetic moments in a macroscopic sample with different spin energy states is described by the Boltzmann statistics. In Eq. 1.5, $n_{\frac{-1}{2}}$ and $n_{\frac{1}{2}}$ describe the number of spins with high ($I = -\frac{1}{2}$) and low ($I = \frac{1}{2}$) energy level, respectively.

$$\frac{n_{\frac{-1}{2}}}{n_{\frac{1}{2}}} = exp\,(-\frac{\hbar\omega_0}{k_B T}) \tag{1.5}$$

with the Boltzmann constant k_B= 8.6173·10^{-5} eV·K^{-1}. Since in most of the cases $h\omega_0 \ll k_B \, T$ the above relations can be rewritten as:

$$\frac{n_{\frac{-1}{2}}}{n_{\frac{1}{2}}} = 1 - \frac{\hbar\omega_0}{k_B T} = 1 - \frac{\gamma\hbar B_0}{k_B T} \tag{1.6}$$

Accordingly, the spin population difference in the static magnetic field is given by

$$\Delta n = n_{\frac{1}{2}} - n_{\frac{-1}{2}} = n_{\frac{1}{2}} \cdot \left(1 - \frac{n_{\frac{-1}{2}}}{n_{\frac{1}{2}}}\right) \propto \frac{\gamma \hbar B_0}{k_B T} \tag{1.7}$$

It can be concluded that even at a very high external magnetic field just a few ppm of the total number of spins can be polarized at room temperature. This is why NMR is generally considered as an insensitive technique. However, the net magnetization vector which represents this small population difference can provide much useful information regarding the chemical structure, molecular dynamics, and spatial distribution.

The nuclear spin magnetization can be described by the Curie law (Eq. 1.8), which is based on nuclear spin and Boltzmann distribution. The equation defines the relation between equilibrium magnetization ($\vec{M}_0$) and the magnetic field strength ($\vec{B}_0$). In Eq. 1.8, T stands for temperature, and N is the number of nuclei. According to Curie's law, a linear relationship between $\vec{M}_0$ and the number of nuclei and B_0 can be assumed [2].

$$\vec{M}_0 = N \frac{\gamma^2 \hbar^2 \, I(I+1)}{3 \, k_B T} \, \vec{B}_0 \tag{1.8}$$

A higher magnetic field increases the population difference between the energy level of spins. Therefore, a stronger magnetic field may provide more information about a spin system by increasing the population difference. However, it should be mentioned, using low magnetic fields one can measure various transport properties in porous media, as it will be discussed later in the final chapter of this thesis (Chapter 7).

1.1.4. Dynamics of magnetization

So far, we have discussed the advantages of polarization of proton spins. However, merely polarizing the spins would not allow us to get the required information of the spin system. To acquire useful information in NMR measurements, precession of spins under the magnetization $\vec{M}_0$ needs to be disturbed for a certain period of time. Radio frequency (RF) pulses are used to cause the disturbance in the precession of spins around the static magnetic field. Therefore, according to the investigated system, symmetric or asymmetric pulses with a duration range of microseconds to some seconds are used. The

RF field imposes an additional resonant magnetic field B_1 acting perpendicular to the main static field B_0 and rotates the magnetization out of its equilibrium position along B_0. B_1 may be written as:

$$\vec{B}_1(t) = B_1\,(t)\,cos\omega t\,\vec{x} - B_1\,(t)\,sin\omega t\,\vec{y} \tag{1.9}$$

For spins with an angular frequency ω, a RF pulse of duration t_p flips the magnetization by a certain flip angle (FA) given by

$$\alpha = \gamma \int_0^{t_p} B_1(t)\,dt \tag{1.10}$$

The pulse duration and its shape can be customized based on application and material or system. As a result of a 90° RF excitation pulse, the macroscopic magnetization is flipped into the transversal plane (Fig. 1.1, a to b) precessing around the z-axis, i.e., $\vec{B}_0$ for a certain time until it returns the equilibrium state. Fig. 1.1b shows the net M_0 immediately after the RF pulse, where the magnetization vector performs a coherent or in phase precession in the xy-plane and around the z-axis. Soon after the net magnetization starts to de-phase and returns to the equilibrium state before an RF pulse applied again.

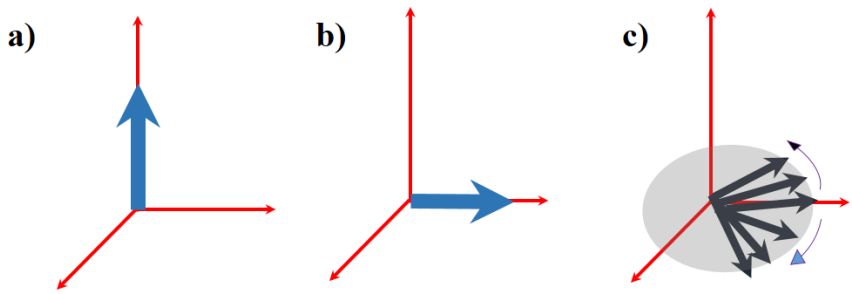

Figure 1.1. Effect of RF excitation pulse on the net magnetization in a coordinate system rotating with ω (c.f., Eq. 1.15).

Here, the next essential equation to understand NMR rises to describe time-dependence magnetization:

$$\frac{d\vec{M}}{dt} = \vec{M} \times \gamma \vec{B}(t) \tag{1.11}$$

The cross product of magnetic field and magnetization also shows that the magnetic moment can be described with angular resonance frequency. Solving Eq. 1.11 gives two components of magnetization vector in x- and y-axes

$$M_x = \vec{M}_0 \sin(\omega_0 t),\ M_y = \vec{M}_0 \cos(\omega_0 t) \tag{1.12}$$

The total magnetization vector can be written as a combination of both compounds as follows:

$$\vec{M}_{total} = \vec{M}_0 \exp(i\,\omega_0 t) \tag{1.13}$$

Under a static magnetic field B_0 and an applied RF pulse of strength B_1, the time dependency of magnetization vector can be described by

$$\begin{aligned}
\frac{dM_x(t)}{dt} &= \gamma[\big(M_y(t)B_0\big) - M_z(t)B_1\, sin\omega t\,] \\
\frac{dM_y(t)}{dt} &= \gamma[(M_z(t)B_1 cos\omega t) - M_x(t)B_0\, sin\omega t\,] \\
\tfrac{dM_z(t)}{dt} &= \gamma[\,M_x(t)B_1\, sin\omega t - (M_z(t)B_1 cos\omega t)]
\end{aligned} \tag{1.14}$$

In order to solve the system of equations, a coordinate system rotating with ω is often used (x', y', z).

$$\begin{aligned}
M'_x &= M_x\, cos\omega t - M_y\, sin\omega t \\
M'_y &= M_x\, sin\omega t + M_y\, cos\omega t \\
M'_z &= M_z
\end{aligned} \tag{1.15}$$

The components of magnetization after considering the rotating frame are given in Eq. 1.16:

$$\frac{dM'_x(t)}{dt} = (\omega_0 - \omega)M'_y(t)$$
$$\frac{dM'_y(t)}{dt} = (\omega_0 - \omega)M'_x(t) + \gamma M'_z(t)B_1$$
$$\frac{dM'_z(t)}{dt} = -\gamma M'_y(t)\, B_1 \quad (1.16)$$

1.1.5. Bloch equation and relaxation times

The temporal behavior of the macroscopic magnetization $M(t)$ during and after excitation is described in good approximation by the Bloch equation. The Bloch equation describes the magnetization ($\vec{M}$) as a vector and a function of NMR relaxation times T_1 and T_2 (Eq. 1.17). In Eq. 1.17 the vector product $\vec{M} \times \vec{B}_0$ corresponds to the torque exerted on the magnetization by the external magnetic field. After dislocation from the equilibrium position, the transverse component of the magnetization precedes with Larmor frequency $\omega_0 = \gamma\, B_0$, which is identical with the resonance excitation frequency.

$$\frac{d\vec{M}}{dt} = \gamma(\vec{M} \times \vec{B}_0) - \frac{\vec{M}_z - \vec{M}_0}{T_1} - \frac{\vec{M}_x + \vec{M}_y}{T_2} \quad (1.17)$$

The terms T_1 and T_2 are called longitudinal relaxation time and transversal relaxation time, respectively. NMR relaxation times can characterize the dynamics of molecules and are sensitive to the surrounding environment, which could be a human cell or a pore in porous media. Different porous structures will cause different relaxation properties based on the surface chemistry, pore size and, if present, paramagnetic species in the pores.

The longitudinal relaxation time or spin-lattice relaxation time T_1 is characteristic for the time needed for the net magnetization to recover after an RF pulse towards the equilibrium value M_0. In other words, T_1 shows the interaction or energy transfer between the spins and the surrounding. Considering Eq. 1.18, the longitudinal component of magnetization can be described as:

$$M_z(t) = M_z(0)e^{-\frac{t}{T_1}} + M_0(1 - e^{-\frac{t}{T_1}}) \quad (1.18)$$

The transversal relaxation time or spin-spin relaxation time T_2, however, describes the exponential decay of the transverse magnetization towards zero. Magnetization in the transverse plane can be described by a complex number, i.e.,

$$M_{xy} = M_x + iM_y \tag{1.19}$$

With resonance frequency $\vartheta_0 = \frac{\omega_0}{2\pi}$, T_2 can be described as following:

$$M_{xy}(t) = M_{xy}(0)\, i \exp\left(-\frac{t}{T_2} - i2\pi\vartheta_0 t\right) \tag{1.20}$$

T_1 and T_2 are critical parameters in investigating heterogeneous catalysts since the catalyst pores have impact on species flowing inside them acting as reactants or products. Thus, one can describe the interaction of materials in the pores by measuring NMR relaxation times [6].

1.1.6. Application of NMR gradient coils in NMR measurements

An additional magnetic field in the z-direction is generated by a magnetic field gradient $\vec{G} = (G_x, G_y, G_z)$. In the presence of such a gradient an additional magnetic field $B = B_0 + B_G$ is expected at coordinate $\vec{r} = (x, y, z)$ given by

$$B(\vec{r}) = B_0 + \vec{G} \cdot \vec{r} \tag{1.21}$$

By multiplying with ɣ, the angular momentum frequency is given by

$$\omega(\vec{r}) = \gamma\, |B(\vec{r})| = \gamma\, (|\vec{B}_0| + \vec{G} \cdot \vec{r}\,) \tag{1.22}$$

Using magnetic field gradients one can obtain useful information on spatial displacement or spatial distribution of spins in an arbitrary orientation. Thus, the usage of gradients allows for 3D characterization of flow and diffusion of liquid or gases in porous media. Details are described in Chapters 2, 3, and 4.

1.1.7. Signal detection

In an NMR measurement, the signal is obtained as an electrical voltage induced in the receiver coil by the precession of the net magnetization after RF excitation and is stored as a Free Induction Decay (FID). In other words, the transverse components of magnetization induce a sine wave voltage into the receiver coil with Larmor frequency (ω_0).
To address some of the discussed NMR basics, a simple spin-echo sequence is explained here [7]. This helps understanding the necessity and importance of RF pulses and their flip angle, and finally the correct design of an NMR experiment. Fig. 1.3 displays a spin-echo sequence, consisting of a 90° pulse followed by a 180° pulse for one repetition time (TR) of the NMR sequence. The sequence is repeated after TR to store measurement data in an array of numbers representing, e.g., the influence of different magnetic field gradients applied. The time interval between the 90° pulse and the appeared signal peak is called echo time (TE). After the 90° pulse the net magnetization is flipped into the xy-plane and precesses around the z-axis (a-b in Fig. 1.2). Soon after, the transversal magnetization tends to de-phase (b-c). Then, the 180° is applied to refocus a portion of de-phased spins that have lost phase coherence (d). Before reaching the 180° pulse, magnetization has partially lost its coherence. After the 180° pulse, each magnetization component still maintains the same (slightly different) frequency corresponding to the local fields (d). At a time corresponding to twice the pulse spacing ($2\times TE/2$), all partial magnetization vectors are in phase again, and their signal contributions sum up to generate a spin echo (e).

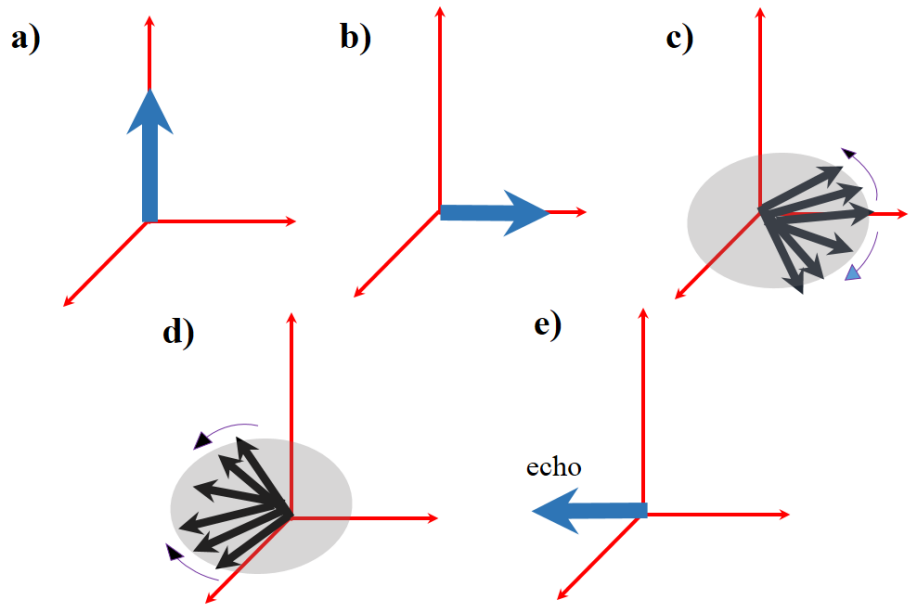

Figure 1.2. Schematic representation of magnetization after a 90° RF pulse (b) followed by 180° RF pulse (d).

If such a spin echo experiment is used, generally, three essential steps should be considered to generate an image as shown in Fig. 1.3, phase encoding, frequency encoding and slice selection. These three steps are briefly explained below.

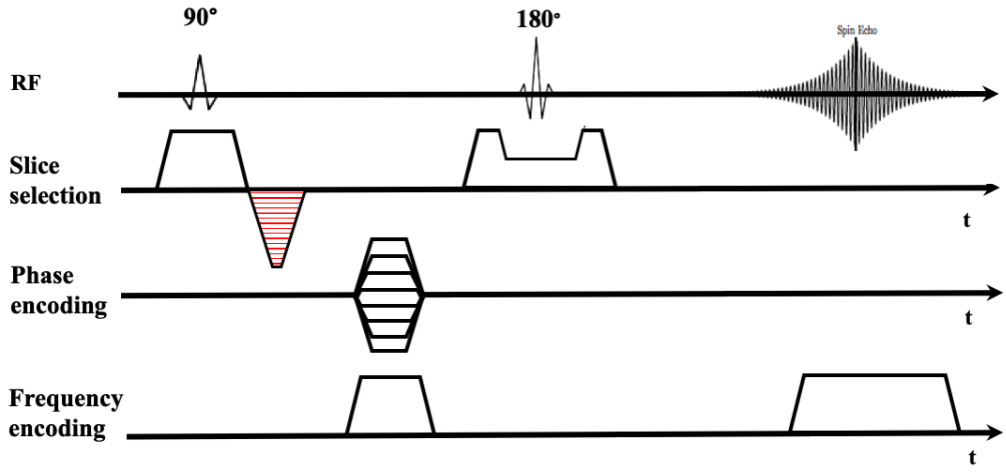

Figure 1.3. Spin-echo sequence (not to scale). Slice selection is implemented while the 90° and 180° pulses are applied.

Phase encoding: A phase-encoding gradient is implemented after the RF excitation pulse and before the readout step. Phase encoding can be applied by implementing incremental changes in the area of gradients. It reveals spatial information about the sample and is typically combined with a frequency encoding gradient to generate an NMR image.

Frequency encoding: In NMR imaging, frequency encoding reveals information on the location of certain spins in the space, as the resonance frequency of the spins is linearly related to their location in the direction of the gradients.

Slice selection: Slice selection is achieved by using slice selection gradients. The slice gradient is applied with selective RF pulse and is typically followed by a slice rephasing lobe to recover phase coherence of transverse magnetization and avoid signal losses.

1.2. Investigation of mass transport in heterogenous systems

The *in situ* analysis of catalyzed gas phase reactions offers not only an accurate characterization of the reactions but also the possibility to validate numerical simulations. The latter allows optimizing operational performance and reducing industrial costs as well as predicting possible risks at scaled up reactors. NMR can be used as a non-invasive method for the *in situ* analysis of velocity, diffusion, temperature, and concentration of species in heterogeneously catalyzed systems [8–13]. The possibility of monitoring the crucial reaction parameters online and simultaneously in an opaque reactor turns NMR into a powerful toolkit for the operando analysis of reactions. To determine each parameter, optimized NMR techniques are required.

This project shows practical and methodological examples of NMR methods in the field of reaction engineering with emphasis on the methanation reaction. It also includes NMR velocimetry of methane gases in foam catalyst carriers followed by an analysis of diffusion and dispersion of gas in monolithic structures. Furthermore, NMR thermometry will be discussed in order to show how the temperature profile of a catalyst bed can be determined in highly exothermic reactions such as methanation or Fischer-Tropsch reaction. On the other hand, the analysis of tortuosity and diffusion in micro- and macrospores illustrates to which extent can NMR characterize heterogeneous catalysts coated on foams or pellets. The obtained results may directly improve numerical micro- or macro-scale simulations.

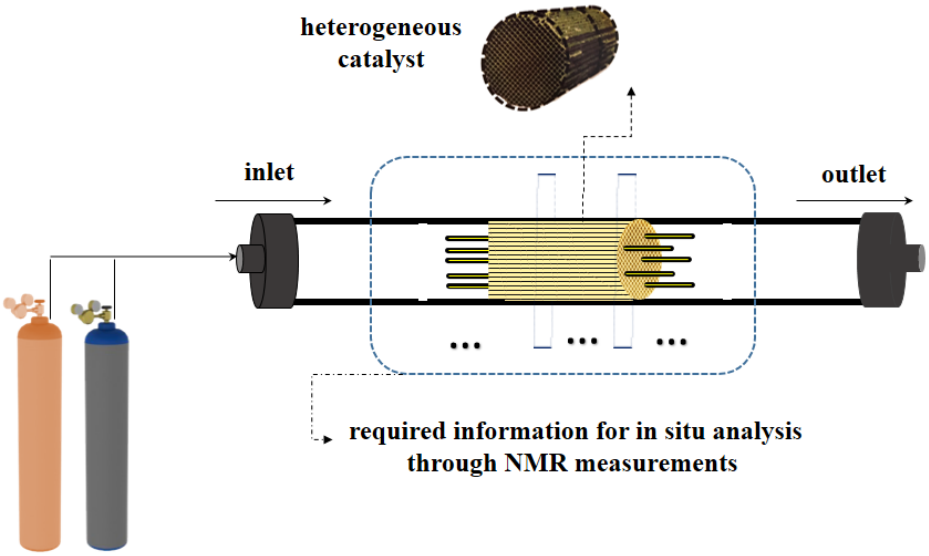

Figure 1.4. *In situ* analysis of performing heterogeneously catalyzed reactors in an NMR system.

The following information were extracted from a heterogeneously catalyzed systems in this project:

- Diffusion and dispersion of gas, with and without flow **(sections 1.2.2 and 1.2.3)**
- Full field velocity analysis of gas in monolithic structures **(section 1.2.4)**
- *In situ* measurement of temperature profiles in catalyst supports **(section 1.2.5)**

Before we explain the applied NMR methods in this dissertation, it is necessary to know in which kind of porous structures these reactions occur. Therefore, a brief introduction of monolithic supports used in heterogenous system is given in the following section. Afterwards, the implemented NMR techniques in this project and some essential facts regarding the experimental approaches are given. Later on, a detailed description of the design and optimization of the NMR measurements is specified in each particular chapter.

1.2.1. Monolithic structures as catalyst support

Open cell foams have been increasingly considered in process engineering applications during the past 20 years [14–20]. The foams are used as catalyst carriers in heterogeneously catalyzed gas phase reactions because of their low pressure drop, high specific surface area and, most importantly, excellent mass and heat transport properties, which enhance the local rate of the heterogeneous reactions [14,17,20]. The investigation of gas mass transport in opaque foams can directly benefit simulations using pseudo-heterogeneous models to predict gas phase reactions such as methanation of CO or CO_2. Among mass transport properties, dispersion coefficients in both radial and axial directions are of high interest to be used in the numerical simulations [21].

1.2.1.1. Production of foam monoliths

Solid foams are typically produced by Schwarzwalder process [22,23], in which a polyurethane (PU) template is usually coated with the ceramic slurry. Then, the coated template undergoes a drying process. Finally, the dried slurry is sintered at a specific temperature. At this stage, struts and pores in open-cell foams gain their solid body. Typically, commercial samples are named based on their PU template and the window size and pore size do not precisely match the nominal values used for the samples, which is due to the production process. The generated solid foams have slightly different pores, windows, and struts as compared to the PU frame, because the material expands during the sintering process. Therefore, the produced foam needs to be carefully studied before they are applied in a process. For more information on the production of foams, one can refer to Studart et al. [24].

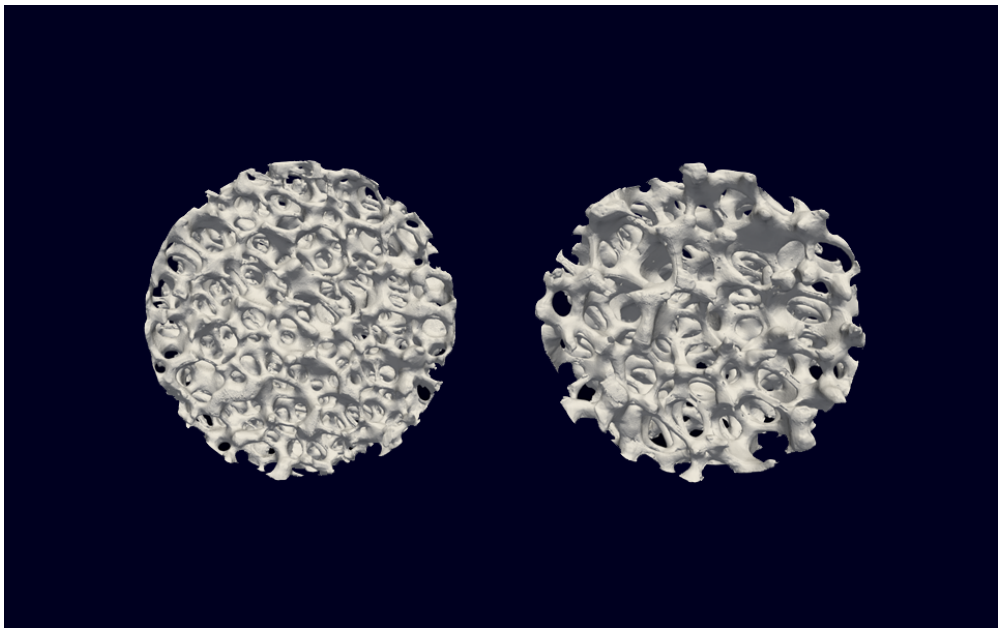

Figure 1.5. Two foam monoliths with different pore size density, pore, and window size. The left-hand and the right-hand porous structure display 20 ppi 10 ppi (pores per inch) foams, respectively.

1.2.1.2. Morphology and geometrical characterization

Al_2O_3 foams (length: 23 mm, diameter: 25 mm, 10, 20, and 40 ppi; Hofmann CERAMIC GmbH, Breitscheid, Germany) and cordierite honeycomb monolith (length: 38 mm, diameter: 25 mm, 600 cell per square inch (cpsi), NGK, Poland) were used for all NMR measurements. Table 1.2 details brief information on the open-cell foams. However, the geometrical characteristics of the samples used in this dissertation were obtained by μ-CT imaging and are detailed in each specific chapter. Window diameter, pore density, strut diameter and open porosity of the samples were the most important characteristics that were computed from the μ-CT data. More explanation on the geometrical properties of the structures can be found in Chapters 2 and 3.

Table 1.2. Characteristics of foams (a: μ-CT, b: tetrakaidecahedral unit cell model).

Sample / Pore density (ppi)	Open porosity [a] (ε)	Pore diameter [a] (d_p) (mm)	Window diameter [a] (d_w) (mm)	Strut diameter [b] (d_s) (mm)	Specific surface area [a] (S_v) ($m^2 \cdot m^{-3}$)
Al_2O_3(10)	0.67	5.35±0.38	3.20±0.77	2.21	544.48[a], 595.11[b]
Al_2O_3(20)	0.77	3.45±0.16	2.40±0.58	1.10	785.71[a], 797.59[b]
Al_2O_3(40)	0.79	2.37±0.30	1.43±0.39	0.73	1105.80[a], (866.00)[b]

1.2.2. Local diffusion measurement in porous media

NMR provides a very exciting research field in measuring static and dynamic properties of porous materials. The porous samples can be characterized by performing MRI and therein flowing species can be analyzed by various NMR measurements techniques. Among the dynamic properties, diffusion and flow are of importance. In particular, when the thermo-physical behavior of gases and translational (or Brownian) motion of their molecules such as diffusion or flow is considered, implementation of powerful in-situ measuring techniques is demanding. Before we turn to the methods applied in this project for characterizing mass transport in heterogeneously catalyzed systems, it is necessary to define and clarify one important concept measured in NMR diffusiometry measurements, 'self-diffusion'.

In general, two types of diffusion processes can be assumed, self-diffusion and mutual diffusion. The former means a type of diffusion that occurs in the absence of any macroscopic gradient that is typically considered as the driving force for diffusion process, such as temperature, pressure, and concentration gradients. The latter diffusion type, mutual diffusion, occurs in a macroscopic mixing that leads to diffusion between two or more fluids. In the following, we focus on self-diffusion measurements. This is a critical point for those chemical/mechanical engineers who are looking for gradients and the resulting transport, while in our diffusion measurements no macroscopic gradients

in temperature or pressure and concentration or chemical potential between two materials occur. In the next section a brief definition of self-diffusion is given to better clarify this term.

1.2.2.1. Self-diffusion

Gas molecules move and change their positions with specific trajectories even in equilibrium condition, which does not offer any concentration gradient. This translational movement of the particles is called self-diffusion [25,26]. Two different conditions are illustrated in Fig. 1.6, which are addressing diffusion in non-equilibrium and equilibrium conditions, respectively. The right-hand side image shows the random motion of a marked molecule (black points) in an environment that continues its motion.

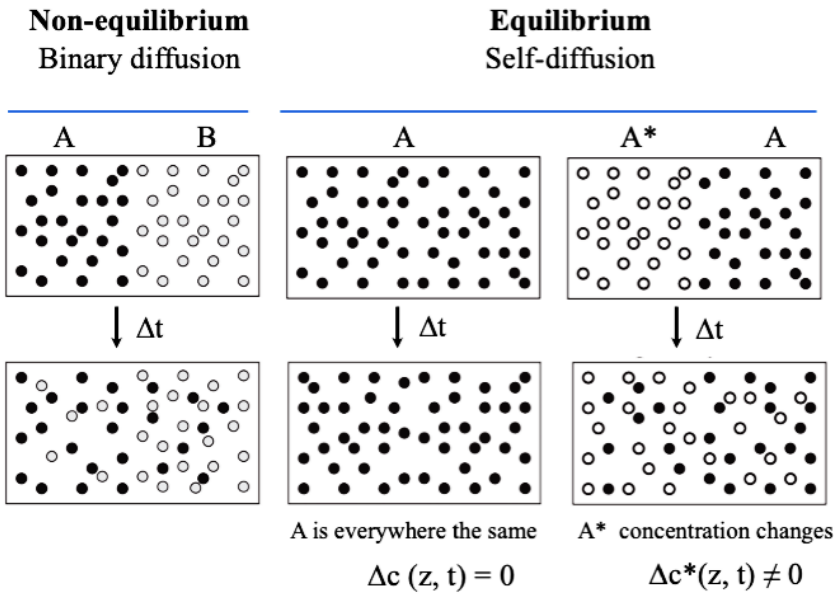

Figure 1.6. Schematic presentation of diffusion in macroscopic non-equilibrium and equilibrium conditions [26,27].

The measured self-diffusion coefficient can provide beneficial information about the restriction in diffusion in transport phenomena [27,28]. Due to the existence of the pore walls, the diffusion of gas in porous media is hindered and restricted. Then, the diffusion

coefficient can be named by another term, effective diffusion coefficient D_{eff}. In porous structures, pore surfaces play a significant role in the hindrance and restriction of diffusion phenomena [27]. The hindrance result from the reflection on the walls and windows of pores affect free diffusion process of the guest materials i.e., gas or liquid molecules inside the porous media. Therefore, even minor difference in self-diffusion, now called 'effective diffusion' values of gas or liquids, can be distinguished. This explanation may be grasped better using Fig. 1.7 that shows how some of the gas molecules can be reflected, hindered or stocked during their pathways through an open-cell foam within a given diffusion time.

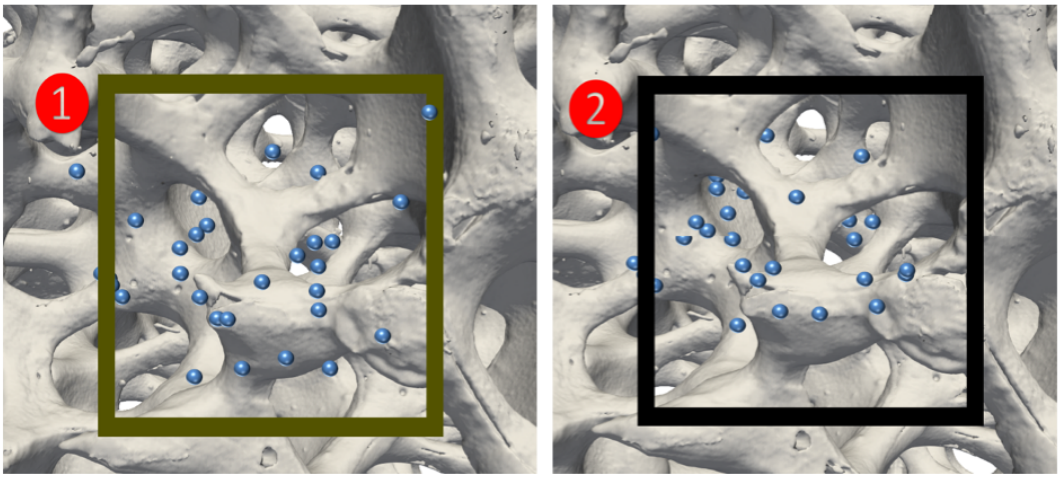

Figure 1.7. A scheme of localized labelling of an ensemble of gas molecules in open-cell foams. Gas molecules experience hindrance and reflection while moving in the foam. Effective diffusion can be characterized by measuring the propagator of gas molecules within the time interval between 1 and 2 to comprehend the effect of pore and window size on the mass transport.

One of the most important parameters influencing mass transport in ceramic foam catalysts is pore window size. It is promising to use NMR spectroscopy and imaging techniques as powerful characterization methods to investigate the effect of pore window size on the propagator function of gases in catalytic gas phase systems. These techniques provide information for designing new tailored structures that offer higher mass

transport efficiency. In our study, commercial ceramic structures were experimentally investigated via an optimized localized Pulsed Field Gradient Stimulated Echo (PFG-STE) method to demonstrate the powerful advantages of using NMR for non-invasively characterizing opaque systems. The measurements show the local variations of the gas displacement function and diffusion coefficients measured in an arbitrary volume element and in arbitrary spatial direction. The results can be used for determining effective diffusion and comparing the results with average dispersion coefficient of gases predicted by numerical simulations of heterogeneous systems. The optimized PFG-STE method was applied on a 7T MRI system using a broad range of diffusion observation times (3.5-30 ms). Raw and coated ceramic structures were characterized at 1.3 bar pressure and ambient temperature. The study allowed a comparative investigation of the gas propagator, diffusion coefficient and tortuosity for the structures in a local manner.
After describing the concept of self-diffusion, it is essential how the molecules can be labeled for a self-diffusion study. In PFG-STE, labeling of molecules is performed by coding and encoding gradient pulses [25,29,30]. This makes PFGs an effective measuring technique due to the direct investigation of self-diffusion parameters such as a mean square of displacement and diffusion coefficient without solving the Fick's law.
The results of these investigations have been published by the author of this dissertation as the first contributor in a research article in *Chemical Engineering & Technology* to primarily develop a method for volume selective NMR displacement measurements of thermally polarized gas, showing its accuracy by a comparative study of effective diffusion in open-cell foam. A detailed description of the results is given in Chapter 2 of this dissertation.

1.2.3. Dispersion of flowing gas in the monolithic structures

Although the effect of the foam’s geometry on mass transport properties has already been recognized [31,32], radial and axial dispersion coefficients have been predicted by merely using the analogy between heat and mass transfer or conventional pulse tracer measurement methods. This is due to the great difficulties in precise measurements of gas dispersion to give a pore-scale analysis of gas spreading in foams. An exhaustive

dispersion analysis for gas flow is yet to be done to investigate a possible correlation between gas dispersion and the foam topology; both in transversal and in axial direction. Furthermore, NMR promises to allow correlating the effect of Reynolds number Re in Darcy and Darcy-Forchheimer regime on the dispersion to the foam morphology with a higher certainty compared to the traditional measurement methods (see Fig. 1.8).

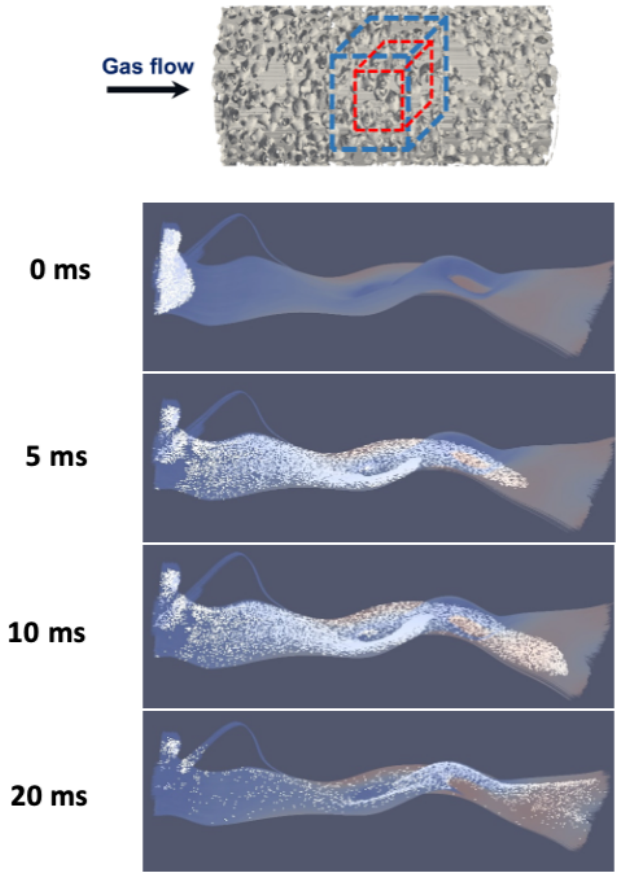

Figure 1.8. A conceptual Computational Fluid Dynamics (CFD) simulation of massless particles using Open-Foam software to show dispersion of gas in an open-cell ceramic foam within 20 ms. The schematic view is merely used to visualize the gas dispersion in foam network over time. While the given simulation result is unable to include diffusional dispersion, a designed NMR measurement can precisely reveal information on both mechanical and diffusional dispersion.

The obtained results in these measurements enabled us to contrast diffusional and mechanical driven dispersion for all foam structures. In particular, it is possible to discuss the transition from Darcy to Darcy-Forchheimer regime. Besides, the accuracy of the current data also enabled us to analyze the effect of window size, flow rate, and open porosity on mass transport in foam samples. The obtained data can directly be used for simulations of mass transport in foams, which is an ongoing topic of research in a specific volume element of the catalyst support or a representative volume element of foam samples. The results of these investigations have been published by the author of this dissertation as the first contributor in a research article in *Chemical Engineering Journal* and are presented in Chapter 3 of this thesis.

1.2.4. Flow of gas in monolithic structures

1.2.4.1. Open-cell foams

In situ analysis of the gas-solid phase helps better understand the mass transport mechanism of gases throughout the monolithic supports in gaseous reactions. Such analysis also facilitates reassessment of the theoretical assumptions. It can be shown that mass transport of gas is extremely affected by minor geometrical alteration of monolith structures, including open cell foams and regular honeycomb monoliths. On one hand, the investigation of mass transport in monoliths usually demands sophisticated experimental setups. On the other hand, numerical simulations can be validated by experimental methods specially where the effect of diffusion, bypassed and flow recirculation zones is highlighted. In this project, Magnetic Resonance Velocimetry (MRV) was applied for flow measurements within solid foams and the obtained data were compared to the flow fields and velocity profiles of CFD simulations. The CFD simulations were carried by Mr. Mehrdad Sadeghi from the Chemical Process Engineering department at the Center for Environmental Research and Sustainable Technology, Faculty 04 (Production Engineering), University of Bremen.

The results have been published in the journal of *Experiments in Fluids*. The manuscript includes both experimental and numerical results (Fig. 1.9). Full field comparison of

MRV data and CFD simulation allowed to investigate velocity of methane in monoliths as a reaction engineering related gas used in methanation reaction.

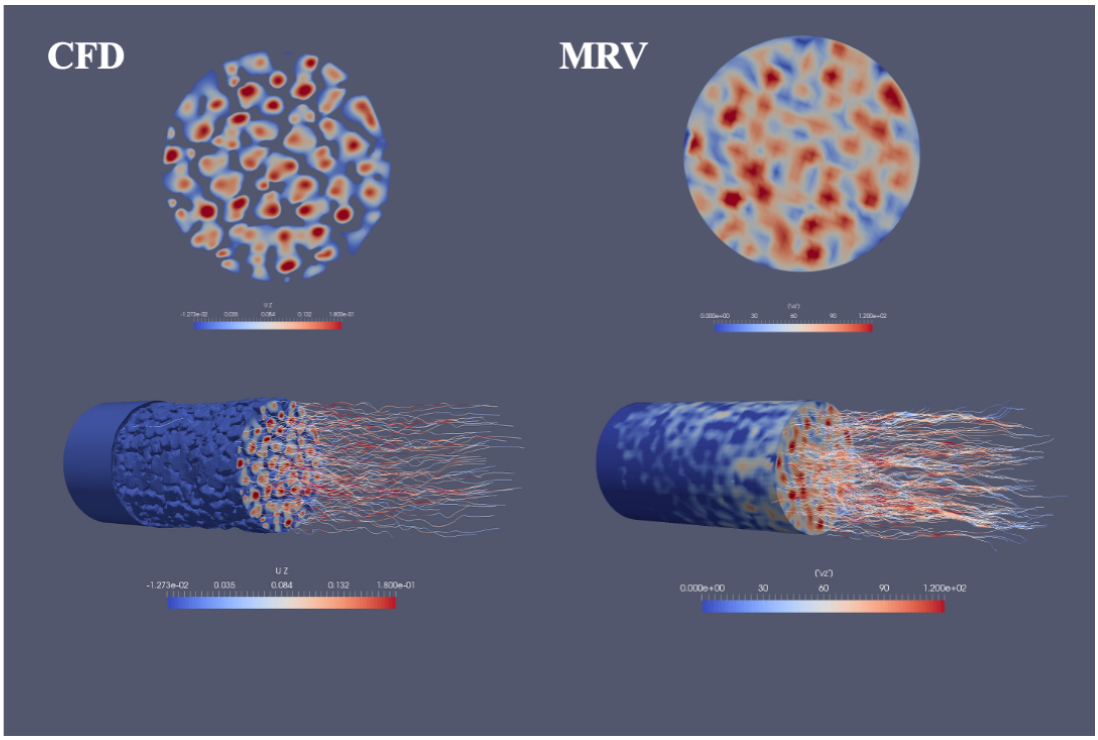

Figure 1.9. Axial velocity obtained in CFD and MRV. A cross-sectional cut of an arbitrary slice of the foams is shown at top to compare the both results.

1.2.4.2. Honeycomb monoliths

Gas velocity was also measured in regularly structured monoliths using MRV. The results were compared to μ-CT based CFD simulations shown in Fig. 1.10. In the performed numerical simulations one presumes that the monoliths are a bundle of ideal and identical channels. This presumption ignores the mal-distribution occurs in the monoliths under a practical process condition. A detailed comparison of the MRV and CFD velocity fields at the entrance, throughout, and the exit region of honeycomb monoliths helped improve simulations and better predict flow behavior in such structures. A manuscript in which the obtained results are described is ready for submission in the journal *Chemical Engineering & Technology*. A detailed comparison of CFD and MRV is elucidated in Chapter 4.

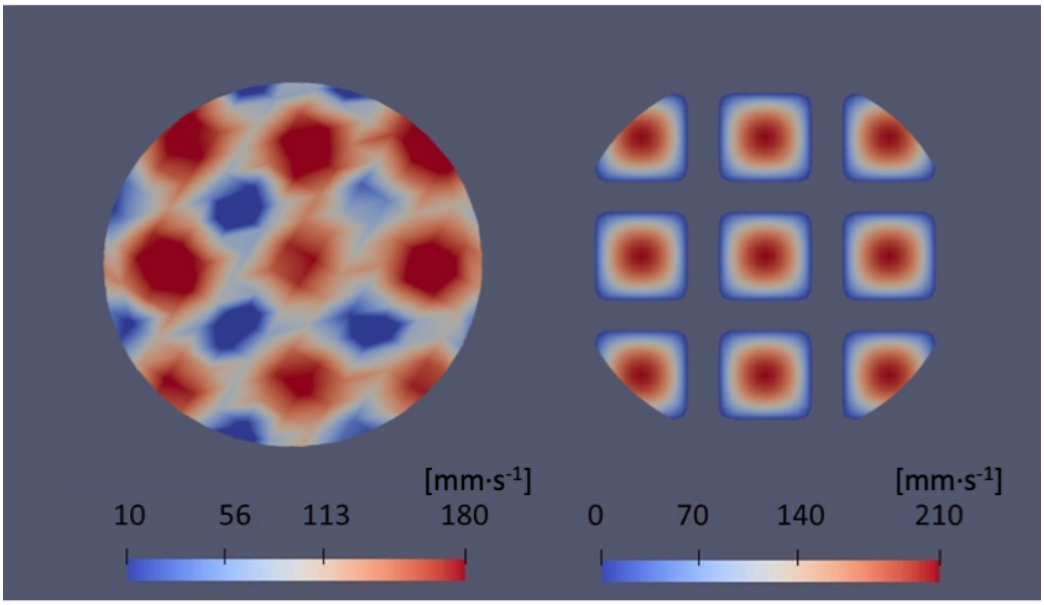

Figure 1.10. Channel-wise comparison of axial velocity in MRV (left) and CFD (right) results in a regular monolithic structure is illustrated.

1.2.5. *In situ* temperature measurement in monoliths

The *in situ* analysis of catalytic gas phase reactions offers not only an accurate characterization of the reactions but also the possibility to validate numerical simulations. The latter allows optimizing operational performance and reducing industrial costs as well as predicting possible risks at scaled up reactors. Accurate measurement of temperature profiles along radial and axial direction of the reactor requires non-invasive approaches to obtain a realistic assessment of the operating systems, without interfering with the process. Among *in situ* approaches, NMR offers a huge flexibility to perform various direct and indirect spatio-temporal measurements for heterogeneous systems. In the current project, two NMR techniques were implemented to obtain a quantitative temperature analysis for a broad temperature range. Magnetic Resonance Spectroscopic Imaging (MRSI) and Diffusion Weighted Magnetic Resonance Imaging (DW-MRI) were applied on a 7T MRI system to assess temperature profiles in the reactor environment and the catalyst bed at high temperatures. The first approach, MRSI, uses capillaries

(OD = 0.7 mm, ID = 0.55 mm) filled with ethylene glycol as thermometers for temperature measurements in the range of 20-150 °C by evaluating the chemical shift difference between the CH_3 and the OH signal. However, the MRSI approach depends on a sufficient spatial homogeneity of the magnetic field, which limits the applicability in some cases (see Fig. 1.11).

Therefore, the second method, DW-MRI, was implemented as a fast and robust toolkit for measurements in a broader temperature range (T < 350 °C), being more robust against magnetic field inhomogeneities than MRSI. The optimized 3D DW-MRI method acquires images with high spatial resolution (~ 0.5×0.5×1.5 mm^3) using four different diffusion sensitizing gradients corresponding to different diffusion weightings (b-values). Fitting the measured signal intensities $S(b)$ in each voxel according to $S = S_0 \cdot exp(-b \cdot D)$ allows to determine the temperature dependent diffusion coefficient D, and thus the temperature. Initial experiments used ethylene glycol and glycerol as probing liquids. To enable measurements of temperature up to 350 °C, ionized fluids with very high decomposition temperature were investigated in this project as well.

In Chapter 5 of this thesis the details of the method developments for temperature measurement of highly exothermic reaction are described. The results of these investigations have been published by the author of this dissertation as the first contributor in a research article in *Reaction Chemistry and Engineering* (Royal Society of Chemistry).

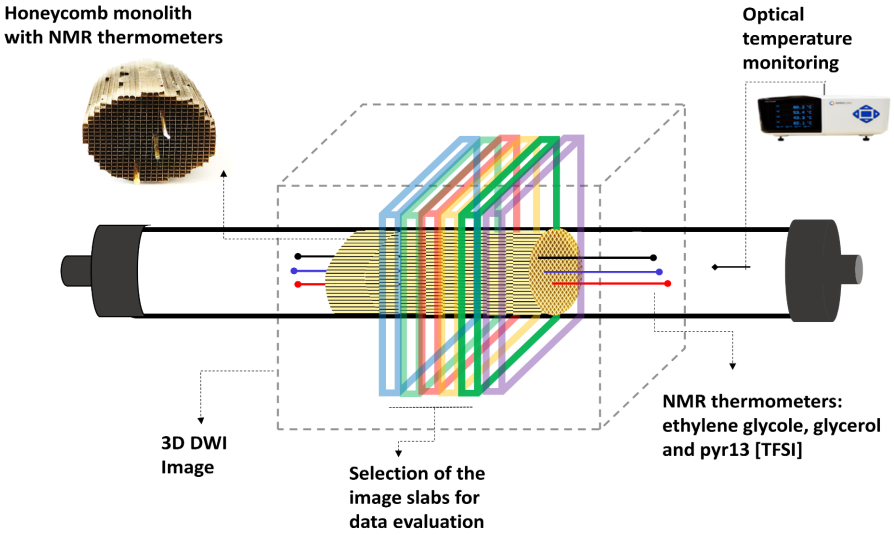

Figure 1.11. Schematic of a model reactor filled with NMR thermometers to measure temperature in a system exposed with axial gas flow. The setup was used in the NMR method developments for *in situ* analysis of temperature.

1.2.6. Mass transport of liquid in porous media

1.2.6.1. Zero Echo Time (ZTE) MRI for distribution of water in porous media

MRI measurements can be conducted by an optimized ZTE MRI pulse sequence [33] to measure water distribution in green bodies of ceramics (Fig. 1.12). This method is of high importance for MRI measurements of water in dense ceramic samples due to very short effective transverse relaxation time (T_2^*). In ZTE MRI measurements, frequency encoding gradients are switched on before the excitation pulse is applied. In a series of measurements with short repetition time TR, data are acquired with different gradient orientation allowing the reconstruction of a 3D image by 3D FFT after gridding the measured data on a cartesian grid. The dead time between the end of the RF excitation pulse and the start of data acquisition was minimized (8 µs) to avoid signal losses by T_2^* relaxation. Thus, the image intensity is primarily determined by spin density, i.e., water content in the current measurements.

Suppression of background signals originate from NMR hardware components (e.g., supporting material and electronic parts of the RF coil) outside the Field-of-View (FOV) and thus the removal of unwanted wave-pattern image artifacts was achieved

by applying an Outer Volume Suppression (OVS) module prior to RF excitation of the sample [34].

The obtained results of this investigation were published in the *Journal of European Ceramics Society* in a research paper entitled as 'Distribution of water in ceramic green bodies during drying'. The author of this dissertation was a co-author in this manuscript [35].

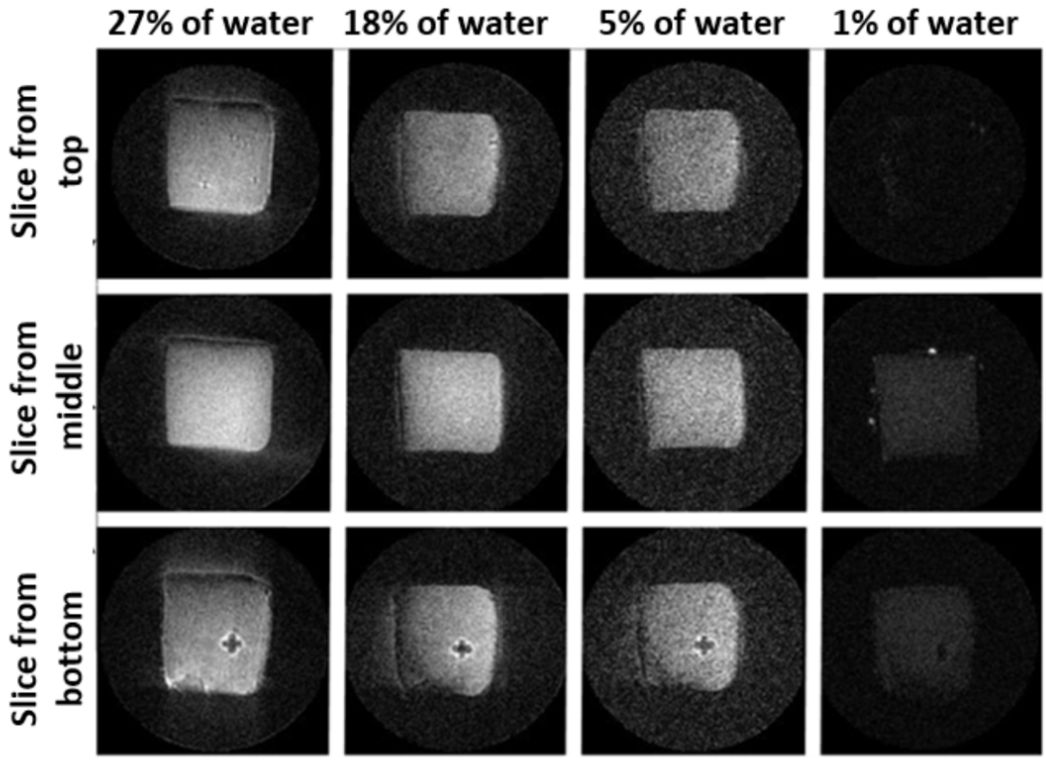

Figure 1.12. MRI of an alumina green body at different positions for total water contents of 27%, 18%, 5% and 1% using ZTE MRI [35].

1.3. NMR facilities

All NMR experiments in this project were performed on a 7 Tesla (Fig. 1.13) preclinical NMR imaging system (Biospec 70/20, Bruker Biospin GmbH, Ettlingen, Germany) equipped with the gradient system BGA12S2 (maximum gradient strength: 441 $mT \cdot m^{-1}$ in each direction, rise time 130 µs). A quadrature birdcage RF coil (inner diameter of 72 mm) was used for RF excitation and signal detection. The NMR pulse sequences were implemented using Paravision 5.1.

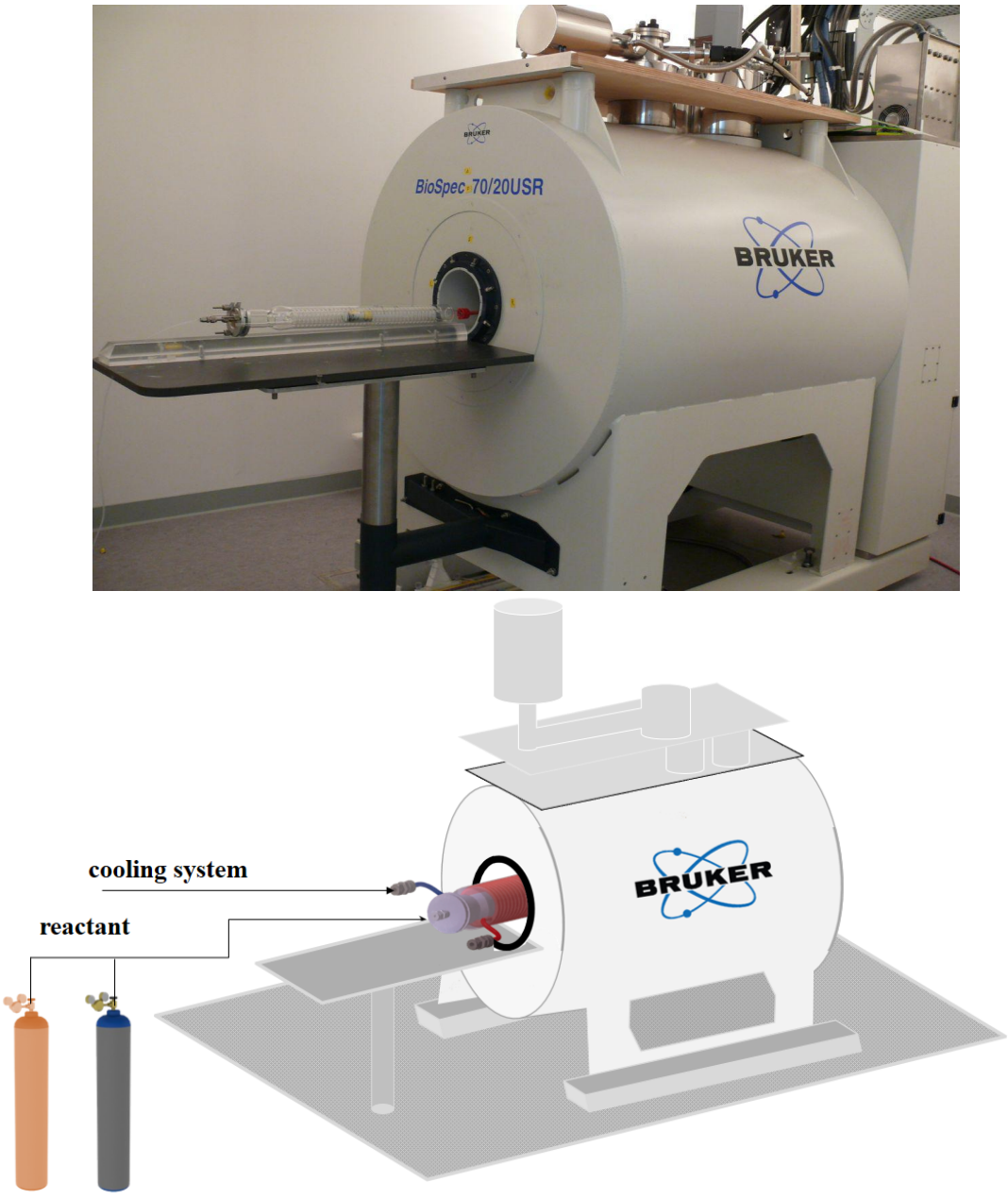

Figure 1.13. (a) 7T NMR scanner. (b) A schematic view of an NMR compatible reactor inserted into the magnet bore of 7-Tesla super-conducting magnet available in in-vivo-MR group of the University of Bremen.

References

[1] M.A. Bernstein, K.F. King, X.J. Zhou, Handbook of MRI Pulse Sequences, 2004. https://doi.org/10.1016/B978-0-12-092861-3.X5000-6.

[2] S. Stapf, S. Han, NMR Imaging in Chemical Engineering, 2007. https://doi.org/10.1016/S1351-4180(07)70357-4.

[3] B. Blümich, P. T. Callaghan. Principles of nuclear magnetic resonance microscopy. Oxford University Press, Oxford, 1993, 492 pp, £25. ISBN 0 198 53997 5, Magn. Reson. Chem. (1995). https://doi.org/10.1002/mrc.1260330417.

[4] J.M. Walker, S.E.E. Ditor, Magnetic Resonance Imaging: Physical Principles and Sequence Design, 2014. https://doi.org/10.1002/9781118633953.

[5] D.J. Griffiths, D.F. Schroeter, Introduction to Quantum Mechanics, 2018. https://doi.org/10.1017/9781316995433.

[6] C. D'Agostino, J. Mitchell, L.F. Gladden, M.D. Mantle, Hydrogen bonding network disruption in mesoporous catalyst supports probed by PFG-NMR diffusometry and NMR relaxometry, J. Phys. Chem. C. 116 (2012) 8975–8982. https://doi.org/10.1021/jp2123295.

[7] E. Hahn, Spin echoes, Phys. Rev. 80 (1950) 580–594. http://link.aps.org/doi/10.1103/PhysRev.80.580.

[8] A.A. Lysova, A. V. Kulikov, V.N. Parmon, R.Z. Sagdeev, I. V. Koptyug, Quantitative temperature mapping within an operating catalyst by spatially resolved ^{27}Al NMR, Chem. Commun. (2012). https://doi.org/10.1039/c2cc31260c.

[9] I. V. Koptyug, Magnetic resonance imaging methods in heterogeneous catalysis, Spectrosc. Prop. Inorg. Organomet. Compd. 39 (2014) 1–42. https://doi.org/10.1039/9781782621485-00001.

[10] I. V. Koptyug, A.A. Lysova, A. V. Kulikov, V.A. Kirillov, V.N. Parmon, R.Z. Sagdeev, Functional imaging and NMR spectroscopy of an operating gas-liquid-solid catalytic reactor, Appl. Catal. A Gen. 267 (2004) 143–148. https://doi.org/10.1016/j.apcata.2004.02.040.

[11] L.F. Gladden, Magnetic Resonance: Ongoing and Future Role in Chemical

Engineering Research, AIChE J. 49 (2003) 2–9. https://doi.org/10.1002/aic.690490102.

[12] L.F. Gladden, M.D. Mantle, A.J. Sederman, Magnetic resonance imaging of catalysts and catalytic processes, Adv. Catal. 50 (2006) 1–75. https://doi.org/10.1016/S0360-0564(06)50001-X.

[13] J. Ulpts, W. Dreher, L. Kiewidt, M. Schubert, J. Thöming, In situ analysis of gas phase reaction processes within monolithic catalyst supports by applying NMR imaging methods, Catal. Today. 273 (2016) 91–98. https://doi.org/10.1016/j.cattod.2016.02.062.

[14] P.D. Eggenschwiler, D.N. Tsinoglou, J. Seyfert, C. Bach, U. Vogt, M. Gorbar, Ceramic foam substrates for automotive catalyst applications: Fluid mechanic analysis, Exp. Fluids. 47 (2009) 209–222. https://doi.org/10.1007/s00348-009-0653-2.

[15] M.V. Twigg, J.T. Richardson, Theory and applications of ceramic foam catalysts, Trans IChemE. 80 (2002) 183–189. https://doi.org/https://doi.org/10.1205/026387602753501906.

[16] Y. Peng, J.T. Richardson, Properties of ceramic foam catalyst supports: one-dimensional and two-dimensional heat transfer correlations, Appl. Catal. A Gen. 266 (2004) 235–244. https://doi.org/10.1016/j.apcata.2004.02.012.

[17] S. Zuercher, K. Pabst, G. Schaub, Ceramic foams as structured catalyst inserts in gas-particle filters for gas reactions-Effect of backmixing, Appl. Catal. A Gen. 357 (2009) 85–92. https://doi.org/10.1016/j.apcata.2009.01.020.

[18] M. V. Twigg, J.T. Richardson, Fundamentals and applications of structured ceramic foam catalysts, Ind. Eng. Chem. Res. 46 (2007) 4166–4177. https://doi.org/10.1021/ie061122o.

[19] F. Lucci, A. Della Torre, G. Montenegro, P.D. Eggenschwiler, On the catalytic performance of open cell structures versus honeycombs, Chem. Eng. J. 264 (2015) 514–521. https://doi.org/10.1016/j.cej.2014.11.080.

[20] R.M. Heck, S. Gulati, R.J. Farrauto, The application of monoliths for gas phase catalytic reactions, Chem. Eng. J. 82 (2001) 149–156.

https://doi.org/https://doi.org/10.1016/S1385-8947(00)00365-X.

[21] B. Kreitz, G.D. Wehinger, T. Turek, Dynamic simulation of the CO_2 methanation in a micro-structured fixed-bed reactor, Chem. Eng. Sci. 195 (2019) 541–552. https://doi.org/10.1016/j.ces.2018.09.053.

[22] L. Kiewidt, Solid sponges as support for heterogeneous catalysts in gas-phase reactions, Doctoral dissertation, University of Bremen, 2017. https://d-nb.info/1150833947/34.

[23] K. Schwartzwalder, Method of Making Ceramic Articles, 1963.

[24] A.R. Studart, U.T. Gonzenbach, E. Tervoort, L.J. Gauckler, Processing routes to macroporous ceramics: A review, J. Am. Ceram. Soc. 89 (2006) 1771–1789. https://doi.org/10.1111/j.1551-2916.2006.01044.x.

[25] J.E. Tanner, Use of the Stimulated Echo in NMR Diffusion Studies, J. Chem. Phys. 52 (1970) 2523–2526. https://doi.org/10.1063/1.1673336.

[26] F. Stallmach, P. Galvosas, Spin Echo NMR Diffusion Studies, Annu. Reports NMR Spectrosc. 61 (2007) 51–131. https://doi.org/10.1016/S0066-4103(07)61102-8.

[27] W.S. Price, NMR studies of translational motion, Cambridge University Press, 2009. https://doi.org/10.1017/CBO9780511770487.

[28] I. Chang, H. Sillescu, Heterogeneity at the Glass Transition: Translational and Rotational Self-Diffusion, J. Phys. Chem. B. 101 (1997) 8794–8801. https://doi.org/10.1021/jp9640989.

[29] P.T. Callaghan, D. MacGowan, K.J. Packer, F.O. Zelaya, High-resolution q-space imaging in porous structures, J. Magn. Reson. 90 (1990) 177–182. https://doi.org/10.1016/0022-2364(90)90376-K.

[30] J.E. Tanner, E.O. Stejskal, Restricted self-diffusion of protons in colloidal systems by the pulsed-gradient, spin-echo method, J. Chem. Phys. 49 (1968) 1768–1777. https://doi.org/10.1063/1.1670306.

[31] L. Kiewidt, J. Thöming, Multiscale modeling of monolithic sponges as catalyst carrier for the methanation of carbon dioxide, Chem. Eng. Sci. X. 2 (2019) 100016. https://doi.org/10.1016/j.cesx.2019.100016.

[32] L. Kiewidt, J. Thöming, Pareto-optimal design and assessment of monolithic sponges as catalyst carriers for exothermic reactions, Chem. Eng. J. (2019) 496–504. https://doi.org/10.1016/j.cej.2018.11.109.

[33] M. Weiger, K.P. Pruessmann, MRI with Zero Echo Time, EMagRes. 1 (2012) 311–322. https://doi.org/10.1002/9780470034590.emrstm1292.

[34] W. Dreher, I. Bardenhagen, L. Huang, M. Bäumer, On the suppression of background signals originating from NMR hardware components. Application to zero echo time imaging and relaxation time analysis, Magn. Reson. Imaging. 34 (2016) 264–270. https://doi.org/10.1016/j.mri.2015.10.008.

[35] S. OUMMADI, B. Nait-Ali, A. Alzina, J.L. Victor, Y. Launay, M. Mirdrikvand, W. Dreher, K. Rezwan, D.S. Smith, Distribution of water in ceramic green bodies during drying, J. Eur. Ceram. Soc. 39 (2019) 3164–3172. https://doi.org/10.1016/j.jeurceramsoc.2019.04.005.

Chapter 2

Diffusion*

Abstract: Gas diffusivity measurements in opaque porous media have been performed using NMR. An optimized pulsed field gradient stimulated echo (PFG-STE) method with free volume selection was used to investigate the propagator of thermally polarized methane gas within commercial monolithic catalyst supports. Since signal losses due to T_2 relaxation were minimized by using a short echo time, diffusion processes could be characterized by the measured propagator functions and effective diffusion coefficients were determined for a broad range of observation times (3.5-30 ms) and in different spatial directions. The potential of this non-invasive characterization of gas diffusion was demonstrated within honeycombs (600 cpsi) as well as sponges with pore densities of 10, 20, 30 and 40 ppi, either uncoated or coated with a washcoat of 6 wt% Ni/Al_2O_3. In this study, a clear effect of type of monolith, its pore size and coating on effective gas diffusion coefficient and the apparent tortuosity for a given observation time was found.

Keywords: thermally polarized gas, diffusion, heterogeneous catalysis, propagator, tortuosity

* The content of this chapter has already been published: **Mirdrikvand, M.**, Ilsemann, J., Thöming, J. and Dreher, W., 2018. Spatially Resolved Characterization of the Gas Propagator in Monolithic Structured Catalysts Using NMR Diffusiometry. *Chemical Engineering & Technology*, *41*(9), pp.1871-1880.

2.1. Introduction

Nuclear Magnetic Resonance (NMR) provides a fascinating research field for measuring static and dynamic properties of porous structures. In particular, when the thermophysical behavior of gases and the translational motion of the molecules in porous structures such as catalyst carriers are considered, the implementation of a robust *in-situ* measuring technique is of high importance [1–4]. In porous media, pore surfaces play a significant role in the restriction or hindrance of diffusion. This causes a change in the diffusion coefficient D of the guest molecules inside the structure resulting in the effective diffusion coefficient D_{eff}. Although optical *in situ* techniques reveal information on some transport properties in porous media at a molecular level, they are limited to optically accessible systems and unable to measure self-diffusion [2]. NMR, however, is suitable to measure also in case of opaque systems such as catalyst pellets and open porous foams. Moreover, the flexibility of NMR, which allows the combination of spatial resolution with diffusiometry, relaxometry, or spectroscopy, makes spatially resolved NMR measurements even more attractive, allowing a better understanding of the effect of geometry on mass transport in porous structures. It is worth mentioning that NMR diffusiometry enables the detection of the spatial displacement of molecules far below the spatial resolution obtained in magnetic resonance imaging (MRI) or spatially resolved NMR spectroscopy [5-6] .

The application of monolithic ceramic catalyst supports has tremendously grown in recent years [7]. The interconnected network of ceramic sponges named as foams offers less pressure drop and enhanced heat transfer properties as compared to packed beds [7–9]. Therefore, it is promising to use NMR techniques to investigate the effect of pore window size and struts on the propagator function of gases in catalytic gas phase systems.

Recently, some NMR based morphological studies of regular and irregular monolithic structures have been reported [10–19]. Grosse et al. investigated the porosity, pore size distribution and other properties of heterogeneous structures [12]. They described a volume selective NMR imaging study on ceramic sponges to determine the pore size distribution. In another study, Gulijk et al. pointed out that NMR analysis of gaseous

flow in honeycomb channels would be expensive and time consuming compared to local pressure drop measurements [10]. In case of irregular pore structures, however, such local pressure drop measurements are impossible. Codd and Altobelli showed in their case study on glass spheres with a diameter of 300-500 µm that diffusion and flow measurements by NMR can facilitate the investigation of porous structures [1]. Their work confirmed that a global gas propagator analysis yields structural information for a chosen observation time [1,2,11]. Koptyug et al. performed NMR measurements for studying structured catalysts and related transport phenomena in liquids and gases [13, 14]. Changes in the structure of catalyst supports over the operating time of the reactor can also be evaluated [14]. A similar approach, but in the liquid phase and not spatially resolved, was used by Ren et al. on deactivated catalyst samples to show the self-diffusion and tortuosity in naphtha reforming catalyst pellets by ^{1}H NMR on heptane [15]. In addition, Youngs et al. applied PFG NMR for studying the diffusion of liquid isopropanol in an alumina structure to show the interaction of molecules with the surface of the alumina [16].

NMR of thermally polarized gases is more challenging in comparison with liquids due to reduced spin density, faster movements of molecules, and the short transversal relaxation time T_2, which cause a considerably reduced signal-to-noise ratio (SNR) in gas phase NMR [1,17,18]. As a solution, studies on hyperpolarized gases have been published [22]. Although hyperpolarization is a powerful approach, the study of thermally polarized gases is also attractive because the rather expensive hyperpolarization techniques as well as the inherent signal losses by T_1 relaxation during longer experiments are avoided. Additionally, the rather short ^{1}H NMR spin-lattice relaxation time T_1 of thermally polarized gases allow the use of short repetition times TR leading to improved SNR per unit measurement time. Fukushima et al. showed the advantage of measuring thermally polarized gases in porous structures in some instances on Y-TZP ceramic samples and lungs [23]. Additionally, flow studies on hydrogen containing gases in supported catalysts have been performed by Koptyug et al.[24], but, to the best of our knowledge, a spatially resolved study on the diffusion of thermally

polarized gases in monolithic structures with different pore sizes has not been reported yet.

In our work, we demonstrate that such a quantitative analysis can be performed by optimized NMR diffusiometry within a moderate measurement time. The mass transport properties of different monolithic catalyst supports were determined using optimized NMR sequences with a customizable volume of interest offering a spatially resolved detection of the gas propagator in monolithic structures. These measurements can answer the question to which extent self-diffusion of gas molecules varies for different diffusion times and along different spatial directions. Besides, the study was performed on coated and uncoated structures of irregular and regular monolithic supports to reveal characteristic differences, which are relevant for practical applications. The results can also be used for validating the numerical simulation of heterogeneous gas-phase systems both on micro and macro level.

2.2. Theory and Method

2.4.2. PFG-STE measurements

Since Stejskal and Tanner have proposed PFG-NMR experiments for determining diffusion coefficients, spin echo (SE) [4] or stimulated echo (STE) [25] based PFG-NMR measurements have been used in numerous applications [26, 27]. STE pulses sequences exhibit an inherent 50% SNR loss as compared to SE pulses sequences, because signal refocusing is performed by 90° radio frequency (RF) pulses, and not by 180° RF pulses as in SE sequences (cf., Fig. 2.1). However, STE based approaches are often preferred for diffusion studies to minimize relaxation losses (cf., Eq. 2.1). In particular, this applies to gas phase ^{1}H NMR because short spin-spin relaxation times T_2 are found in most cases, while the spin-lattice relaxation time T_1 is much longer than T_2 [27,28].

A volume selective STE pulse sequence [29,30] was implemented on our 7T MRI system to restrict the measurements to a volume element (voxel) with well-defined size and arbitrary voxel orientation. As proposed by Tkáč et al., asymmetric RF pulses were used for reducing the minimum echo time and thus signal losses by T_2 relaxation [31].

Diffusion sensitizing gradients of arbitrary orientation can be applied between the first and the second RF pulse as well as between the third RF pulse and the start of data acquisition. A scheme of the pulse sequence is shown in Fig. 2.1, with δ being the duration and G_d the resulting amplitude of the two diffusion sensitizing gradient pulses applied in x, y and z-direction, and Δ being the delay between these gradient pulses. Note that during the mixing time T_m, i.e., between the second and the third RF pulse the magnetization experiences only T_1 relaxation, thus allowing measurements with a rather long diffusion time.

Assuming Gaussian diffusion, the diffusion coefficient D can be determined by two or more measurements performed with different diffusion weighting expressed by the so-called b-value $b = \gamma^2 \delta^2 {G_d}^2 \left(\Delta - \frac{\delta}{3}\right)$, but with constant TE and T_m. The amplitude of the measured STE signal is given by

$$S = S_0 e^{\frac{-TE}{T_2}} e^{\frac{-T_m}{T_1}} e^{-bD} \quad . \tag{2.1}$$

In the more general approach of 'q-space imaging' proposed by Cory and Garroway [32] as well as Callaghan et al. [33] a series of measurements is performed by incrementing the q-values defined by $q = \gamma \delta G_d$. If $\delta \ll \Delta$ the echo signal is given by

$$S(q) = \int \rho(r_0) \int P(r_0|r, \Delta)\, e^{iq(r-r_0)} dr dr_0 \quad . \tag{2.2}$$

Here r_0 and r denote the position of the spins at the beginning and the end of the observation respectively diffusion time, Δ. Thus, the displacement function P, averaged over the measured sample, can be determined by Fourier transformation of the measured data $S(q)$. P describes the probability that spins have moved during the observation time Δ by the distance $r - r_0$ along the direction of the diffusion gradients.

In case of Gaussian diffusion, the diffusion coefficient D can be determined from the full-width half maximum (FWHM) value of the gas propagator using

$$D = \frac{(FWHM)^2}{(16\, ln(2)\ \Delta)} \qquad (2.3).$$

However, note that rather small differences in FWHM values result in large differences in the diffusion coefficient. The transition from free to increasingly hindered diffusion can be observed by performing measurements with increasing Δ. Considering spherical pores with radius a as a simple model, the dimensionless parameter $\varepsilon = \frac{D\Delta}{a^2}$ helps to distinguish three time regimes [2]: (i) short observation time for $\varepsilon \ll 1$ corresponding to free diffusion and yielding the free diffusion coefficient D_0, (ii) 'crossover' regime for $\varepsilon \approx 1$, in which a certain number of the particles will experience restrictions such as reflections on the pore surface, and (iii) long observation time if $\varepsilon \gg 1$, where for hindered diffusion the diffusion coefficient determined for increasing Δ converges to a value D_∞. The tortuosity, interpreted as a path-length multiplication factor in the long observation time regime, can be calculated by $\frac{D_0}{D_\infty}$. The transition from the crossover regime to the long observation time regime and the corresponding increase in the path-length multiplication factor can be characterized by measuring $\frac{D_0}{D_{\mathrm{eff}}}$ as a function of diffusion time, corresponding to an apparent tortuosity for a given observation time.

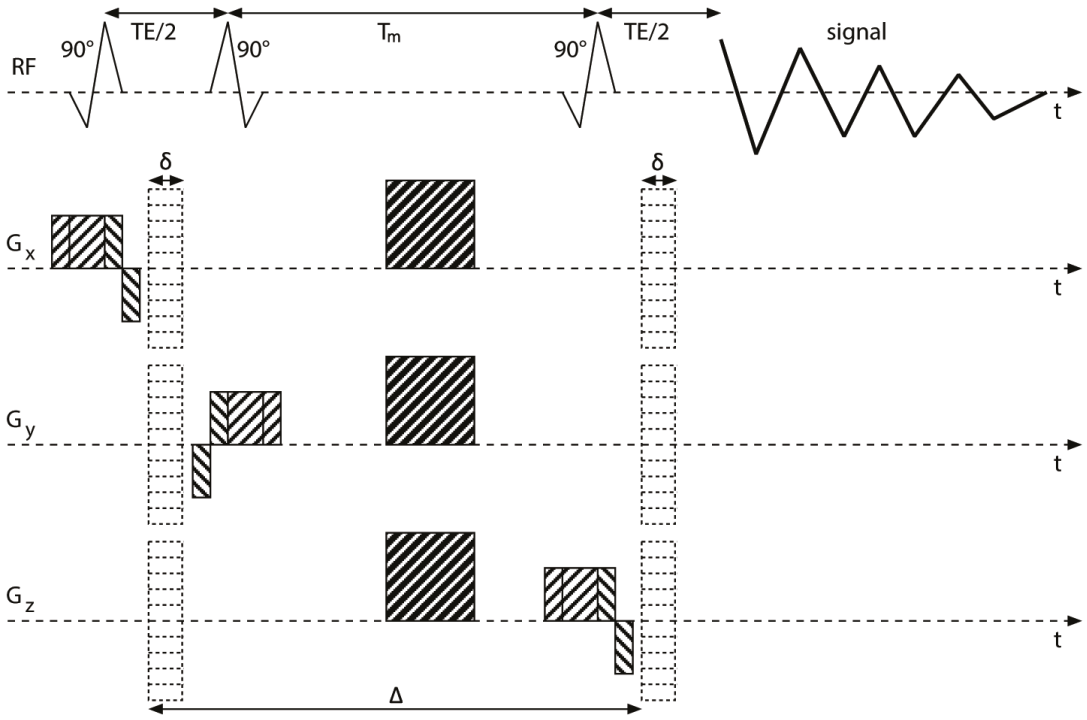

Figure 2.1. Scheme of the optimized PFG-STE imaging sequence (not to scale) used for localized q-space measurements. During the mixing time T_m, spoiler gradients are applied to suppress unwanted coherence pathways. A two-step phase cycle (0°-180°) was applied for the third 90° pulse to suppress the signal excited by this RF pulse.

2.3. Experimental

2.3.1. Materials

Four different Al_2O_3-sponge segments (length: 23 mm, diameter of 25 mm, 10, 20, 30 or 40 pores per inch (ppi); Drache GmbH, Diez, Germany) were used as raw ceramic sponges, and a cordierite honeycomb monolith (length: 38 mm, diameter: 25 mm, 600 cpsi, NGK, Poland) was used as monolithic catalyst support. The morphological characteristics of the samples are given in Table 2.1.

Table 2.1. Properties of the used sponges [34].

Sample	Window diameter (mm)	Strut diameter (mm)	Open porosity ξ	Surface area ($m^2 \cdot m^{-3}$)
10 ppi	3.30 ± 0.98	1.83	0.77	521.3
20 ppi	2.04 ± 0.48	1.22	0.75	852.3
30 ppi	1.92 ± 0.46	1.11	0.76	862.5
40 ppi	1.43 ± 0.39	0.73	0.79	1105.8

The sponge with 20 ppi and the honeycomb were coated as described in the catalyst preparation section. Methane was used as probing gas, because this molecule is of particular interest in our current research on methanation reactions. The samples were positioned in a batch glass tube container (length: 250 mm, diameter: 25 mm) equipped with a pressure valve for the filling process.

Special valves and O-rings (Schott AG, Germany) were used, and leakage tests were conducted to ensure that the gas container was completely sealed.

The gas filling was conducted using a flow meter (One OMEGA FMA-2605 OMEGA Engineering, Norwalk, USA). The pressure in the gas mouse was set to 1.5 bar and temperature during the NMR measurements was 16 °C. The temperature was monitored during all NMR measurements. The gas container was held firmly within the RF coil in order to prevent motional artifacts.

2.3.2. Catalyst preparation

All monolithic substrates were coated with a 6 wt% Ni/Al_2O_3 catalyst layer. Nickel nitrate hexahydrate (Prolabo, 97%) was dissolved in deionized water and mixed with an aqueous γ-Al_2O_3 slurry. The substrates were dipped into the mixed slurry, and excessive material was subsequently blown off using compressed air. The coated samples were dried at 393 K for 1 h and further calcined at 873 K for 2 h (heating ramp 1 $K \cdot min^{-1}$). Comparing the weights of the uncoated and calcined samples, the amount of coating material was determined to be approximately 3.6 g for the honeycomb sample and 1.7

g for the sponge. By evaporation of the liquid phase, the solid fraction of the slurry was determined to be 43.4%. In order to achieve a loading of 6 wt% Ni, 17.94 g of $Ni(NO_3)_2$*$6H_2O$ was dissolved in 16 ml deionized H_2O.

N_2 physisorption: N_2 physisorption measurements were conducted using a NOVA 4000e gas sorption system (Quantachrome Instruments, Florida, USA) to determine the pore size distribution. Prior to each analysis, the powders were degassed at 473 K for at least 2 hours, whereas the subsequent isotherm measurements were conducted at 77 K for a relative pressure p/p_0 in the range of 0.1 to 0.99.

2.3.3. NMR Measurements

Hardware: All NMR experiments were performed on a 7 Tesla preclinical NMR imaging system (Biospec 70/20, Bruker Biospin GmbH, Ettlingen, Germany) equipped with the gradient system BGA12S2 (maximum gradient strength: 441 $mT \cdot m^{-1}$ in each direction, rise time 130 µs). A quadrature birdcage RF coil (inner diameter of 72 mm) was used for RF excitation and signal detection. The NMR pulse sequences were implemented using Paravision 5.1.

MRI: To define the orientation of the samples and to position the voxel for subsequent PFG-NMR measurements, an optimized 3D gradient echo [29] imaging sequence was used with the following protocol: repetition time TR: 25 ms, echo time TE: 0.5 ms, flip angle 45°, field-of-view (FOV): 64×64×96 mm^3, 192×192×16 matrix size, two averages, total measurement time: 2 min 33 s.

Localized PFG-NMR: Localized measurements of displacement profiles were performed with an optimized PFG-STE sequence (cf., Fig. 2.1). Rephasing or dephasing gradients were applied immediately after or prior to the slice selective RF pulses, respectively, to minimize the diffusion weighting. To suppress unwanted signals, spoiler gradients were employed during the mixing time T_m, and a two-step phase cycle (0°-180°) for the third 90° pulse was used. The pulse sequence was used with the following parameters: Asymmetric 90° RF pulses of 500 µs duration calculated by the RF pulse module of the free software suite VESPA [35] (version 0.8, http://scion.duhs.duke.edu/vespa/project), voxel size: 12×12×12 mm^3, repetition time

TR = 250 ms, 64 equidistant q-space values, displacement range +/-5 mm, 1024 complex data points sampled with 25 kHz. Measurements were performed with a TE of 2.6 ms and diffusion times Δ ranging from 3.51 ms to 50 ms. For each set of parameters, six measurements were performed for error estimation and improved accuracy. Optionally, the data sets were averaged to increase the SNR. Three measurements were conducted for each observation time using diffusion sensitizing gradients in x-, y- or z-direction, where z corresponds to the axial direction of cylindrical samples. The measurement time for each measurement was 8 min 23 s.

Data evaluation: The time domain signals were analyzed using self-written MATLAB (R2017b, The MathWorks, Inc., Natick, USA) scripts. The propagator was calculated from the time domain signal applying the following steps Hamming apodization, 1D Fourier transformation along the time domain, magnitude calculation, peak integration and subsequent 1D Fourier transformation along the variable q. Note that magnitude calculation avoids phase errors during phase correction of FT spectra, but suppresses flow effects overlaid on diffusion processes. However, flow is not expected for the current experimental setup.

2.4. Results and discussion

The results are presented in two main parts. First, we analyzed the raw regular and irregular monolithic structures. While the spatial dependence of the gas propagator was studied for the regular structure, the gas propagator was compared between irregular samples with 10, 20, 30 and 40 ppi, and the effective diffusion constants and the apparent tortuosity values were determined at diffusion times from 3.5 ms to 30 ms. Second, the differences in gas diffusion between coated and uncoated honeycomb and sponge samples were analyzed.

Before measuring diffusion in porous structures, the diffusion coefficients of free methane (16 °C, 1.5 bar) was determined. The value of $(2.24 \pm 0.006)\times10^{-5}$ $m^2 \cdot s^{-1}$ is in good agreement with the literature value [36] and remained unchanged after several weeks proving the tightness of the gas container. In addition, the BET surface area of the coated catalyst is found to be 135 $m^2 \cdot g^{-1}$ with a total pore volume of 0.44 $cm^3 \cdot g^{-1}$.

The pore size distribution was calculated by the Barret-Joyner-Halenda model using the desorption branch, showing a maximum at a radius of 4.1 nm.

2.4.1. Raw honeycomb structure

The propagators of methane gas in the raw honeycomb are illustrated in Fig. 2.2. The measurements were conducted with short (5 ms, Fig. 2.2a) and long (30 ms, Fig. 2.2b) diffusion time. A Gaussian fit is superimposed as a reference indicating possible effects of hindered or restricted diffusion. Along longitudinal direction, the diffusion coefficient and the displacement function of the gas were close to the results obtained for freely diffusing gas, slightly affected by the channel-like structure of honeycomb.

At short diffusion time (Δ = 3.5 ms), the diffusion coefficient of gas in longitudinal direction is $D = (2.22 \pm 0.03)\times10^{-5}$ $m^2 \cdot s^{-1}$ showing a difference of < 1% from the free gas value. The diffusion coefficient remains almost constant in longitudinal direction even in long diffusion time measurements (Δ = 30 ms) where $D = (2.11 \pm 0.01)\times10^{-5}$ $m^2 \cdot s^{-1}$ was calculated. The fact that the effective diffusion coefficient is almost independent of the diffusion time is due to unrestricted motion of gas molecules along z-axis and the minor reduction in the diffusion coefficient can be explained by reflected or stagnant gas molecules at the channel walls in the honeycomb. Conversely, in the transversal direction, a significantly narrower curve shows more restricted gas displacement behavior. According to the intrinsic square-like channels of the honeycomb sample, both transversal (in x and y) measurements yield similar, but lower diffusion coefficients. At longer diffusion time, where more interactions between gas molecules and the walls of honeycomb channels are expected, the methane propagator shows a remarkable deviation from the fitted Gaussian curve (cf., Fig. 2.2b). The averaged value for gas diffusion coefficient in transversal direction were $D = (1.12 \pm 0.008)\times10^{-5}$ $m^2 \cdot s^{-1}$ and $(6.26 \pm 0.2)\times10^{-6}$ $m^2 \cdot s^{-1}$, for the short and the long diffusion time, respectively. It is remarkable that the largest displacements of the gas molecules observed in transversal direction at Δ = 30 ms are larger than the width of honeycomb channels length (1 mm), meaning that the gas molecules are still visible in the measurements after having crossed the channel walls.

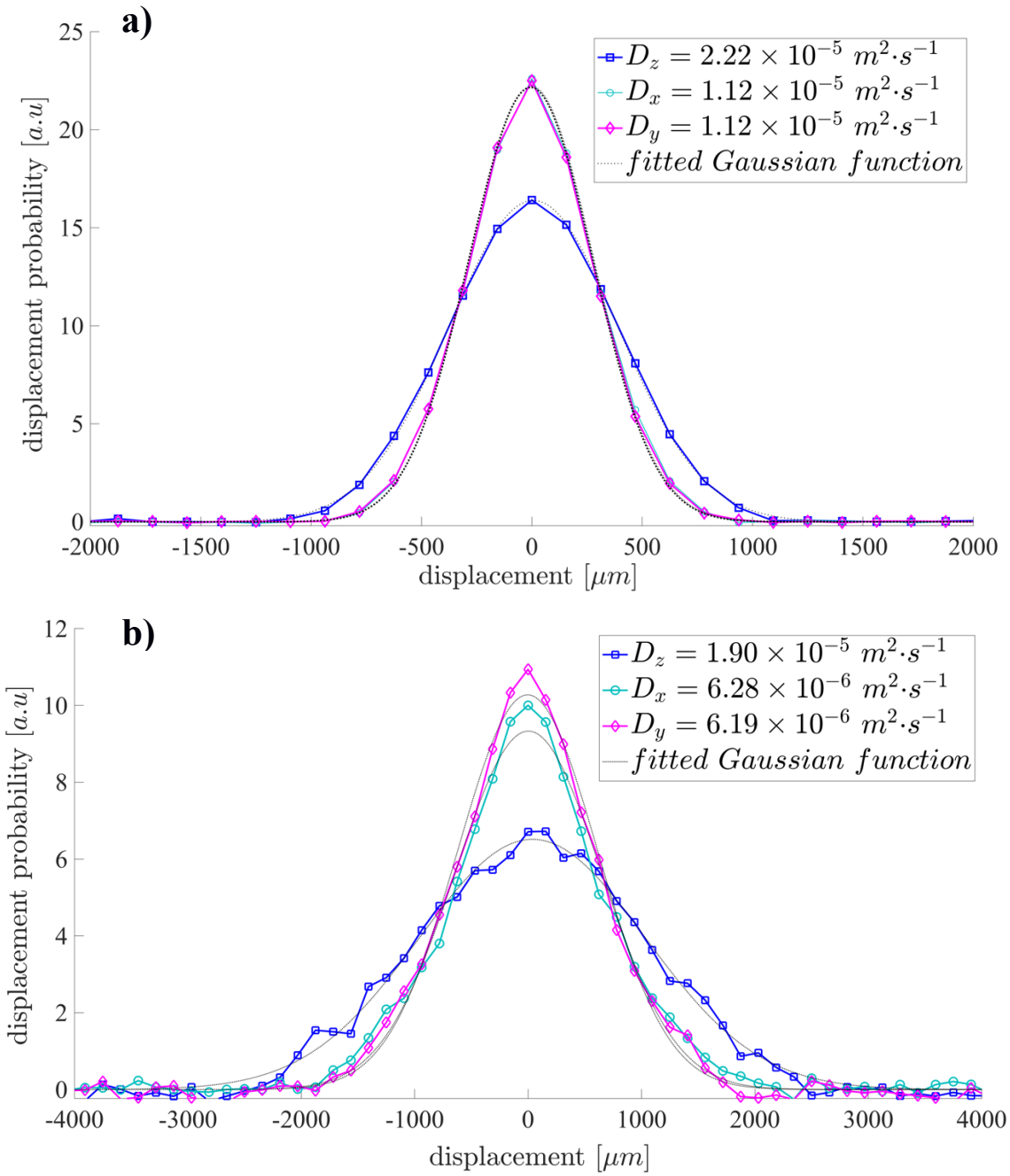

Figure 2.2. The propagators represent the methane gas displacement function in the 600 cpsi honeycomb monolith at (a) Δ = 5 ms and (b) Δ = 30 ms. For comparison, a fitted Gaussian function is overlaid in the same color as used for the measured data.

2.4.2. Analysis of sponge samples with different pore density

Sponges with different pore density were analyzed in order to show the differences in the diffusion coefficient of the probing gas and to determine the apparent tortuosity of the catalyst supports. While Table 2.2 gives the diffusion coefficients in x-, y-, and z-direction, an average value is depicted on each graph in Fig. 2.3. Although the average values for the diffusion coefficients for the propagators in Fig. 2.3 withhold the anisotropic behavior of the diffusion process in the porous sample, they represent the average properties of the samples based on their pore density and heterogeneity.

Table 2.2. Effective diffusion coefficients ($D_{\mathrm{eff,i}}$ $\times 10^5/\,\mathrm{m^2\cdot s^{-1}}$) versus diffusion times. The values state the computed diffusion coefficients along the spatial directions $i = z$, x and y for 10-40 ppi sponge samples.

	10 ppi			**20 ppi**			**30 ppi**			**40 ppi**		
Δ	$D_{\mathrm{eff,z}}$	$D_{\mathrm{eff,x}}$	$D_{\mathrm{eff,y}}$	$D_{\mathrm{eff,z}}$	$D_{\mathrm{eff,x}}$	$D_{\mathrm{eff,y}}$	$D_{\mathrm{eff,z}}$	$D_{\mathrm{eff,x}}$	$D_{\mathrm{eff,y}}$	$D_{\mathrm{eff,z}}$	$D_{\mathrm{eff,x}}$	$D_{\mathrm{eff,y}}$
3.5 ms	1.96± 0.01	2.01± 0.02	2.01± 0.02	1.79± 0.02	1.87± 0.01	1.87± 0.01	1.74± 0.01	1.84± 0.01	1.83± 0.01	1.69± 0.01	1.79± 0.01	1.74± 0.02
5 ms	1.91± 0.02	1.96± 0.02	1.96± 0.02	1.68± 0.02	1.78± 0.03	1.78± 0.03	1.63± 0.02	1.77± 0.01	1.73± 0.01	1.59± 0.01	1.71± 0.01	1.66± 0.01
10 ms	1.73± 0.02	1.82± 0.02	1.82± 0.01	1.53± 0.05	1.63± 0.04	1.63± 0.02	1.45± 0.02	1.61± 0.02	1.59± 0.02	1.48± 0.03	1.61± 0.04	1.51± 0.02
20 ms	1.52± 0.02	1.65± 0.06	1.63± 0.02	1.34± 0.07	1.47± 0.07	1.56± 0.05	1.32± 0.09	1.51± 0.07	1.43± 0.04	1.42± 0.02	1.61± 0.07	1.42± 0.06
30 ms	1.46± 0.06	1.52± 0.07	1.62± 0.11	1.32± 0.15	1.38± 0.15	1.40± 0.10	1.34± 0.05	1.46± 0.10	1.36± 0.04	1.45± 0.09	1.61± 0.08	1.36± 0.10

At short diffusion times (3.5 ms), the propagators of all sponges show hindered motion influenced by pore walls resulting in narrower peaks compared to the propagator measured for free gas. Even at this rather short diffusion time the sponges with higher pore density are already considerably affected by the interaction with pore walls. Only the 10 ppi sponge shows less hindrance and thus smaller differences to the data from free gas. This remaining difference can also be recognized by comparing the baselines of the displacement functions of free gas and the 10 ppi sample. The displacement

function of free gas reaches the baseline at ~1.5 mm at 3.5 ms diffusion time (Fig. 2.3a), while the gas propagator of the 10 ppi sample reaches the baseline at ~1.2 mm. These findings are consistent with the different values of the windows diameter of the samples (cf., Table 2.1), which is 3.3 mm for the 10 ppi sample, explaining the observed differences from the propagator of free gas. The smaller window size of pores in the 20, 30 and 40 ppi samples hinders the gas more than in the 10 ppi sponge, resulting in narrower propagators and smaller diffusion coefficients (cf., Table 2.2). Although, at a first glance, the gas propagator of samples possessing higher pore density values (20, 30 and 40 ppi) seem to be almost identical, some differences appear in the determined FWHM values of their displacement functions. In addition, at diffusion time of 5 ms to 10 ms, the gas molecules in the 10 ppi sample show broader displacement compared with the other sponges (20-40 ppi) (cf., Fig. 2.3b and Fig. 2.3c).

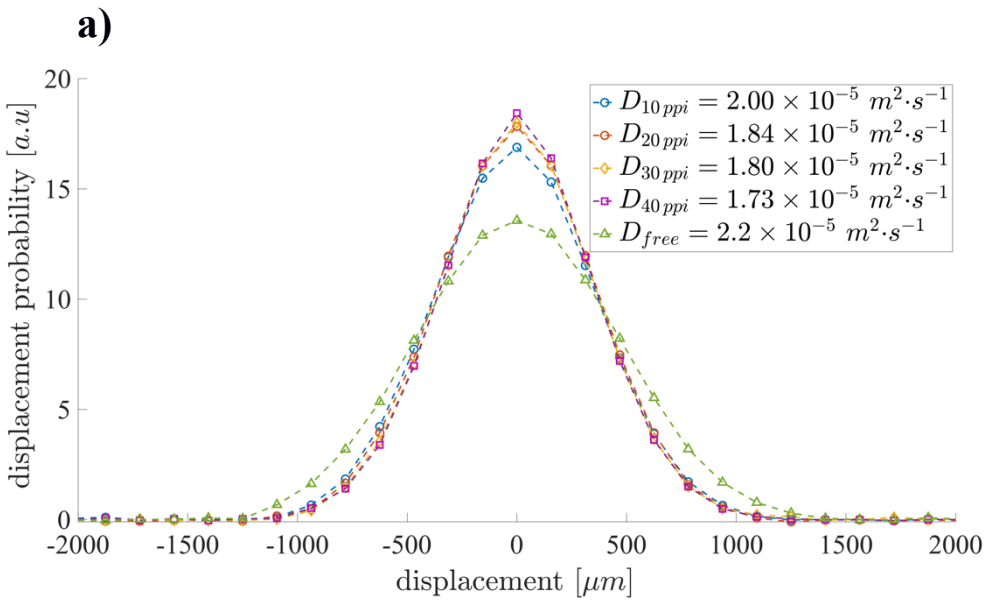

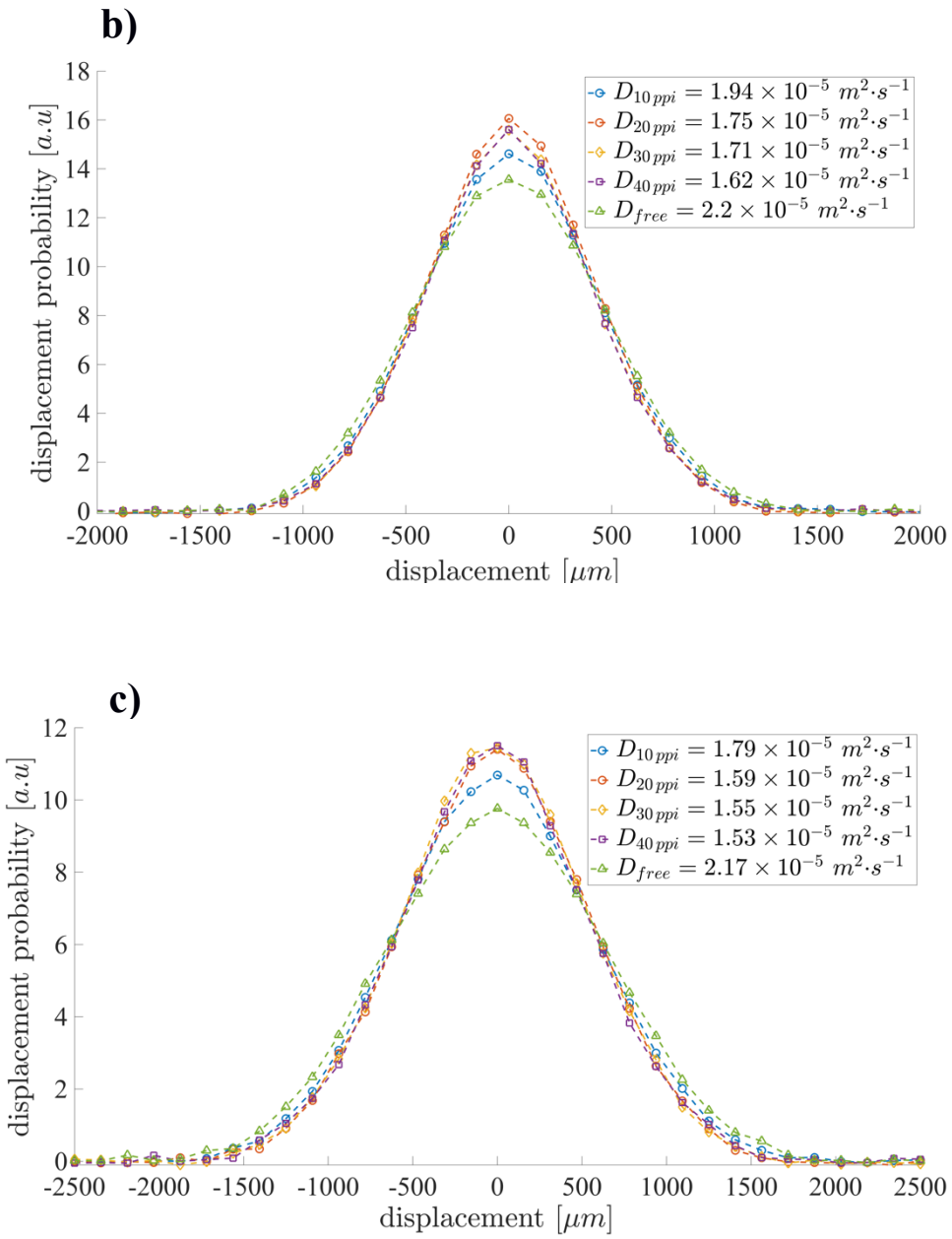

Figure 2.3. Gas displacement function for irregular monolithic structures at (a) Δ = 3.5 ms, (b) Δ = 5 ms and (c) Δ = 10 ms. Average values of diffusion coefficients are added to the figures for comparison.

As shown in Table 2.2, the diffusion coefficient is decreased for the samples of higher pore density at each observation time. Thus, the highest and lowest diffusion

coefficients belong to the 10 ppi and the 40 ppi samples, respectively. As an example for the trend of diffusion coefficient versus diffusion time, Fig. 2.4 shows the diffusion coefficients measured in y-direction. For all sponges, the observed effective diffusion coefficient decreases steadily with increasing diffusion time converging to different D_∞ values. Already at a short observation time (3.5 ms), the gas propagators are affected by the macroscopic morphology of the sponges. As expected, the diffusion process is more influenced in the samples with smaller pore sizes, not only in y-direction (cf., Fig. 2.4), but in all directions (cf., Table 2.2, Δ = 20-30 ms). For longer diffusion times, the effect of different mean pore density of the sponges increases with increasing diffusion time. Consequently, the diffusion coefficients decrease with longer observation times (cf., Fig. 2.4). At diffusion times of Δ = 20-30 ms, the time dependence of the diffusion coefficients starts to reach a plateau. This behavior can be regarded as a consequence of both the long interconnected network of pores and the related tortuosity [1].

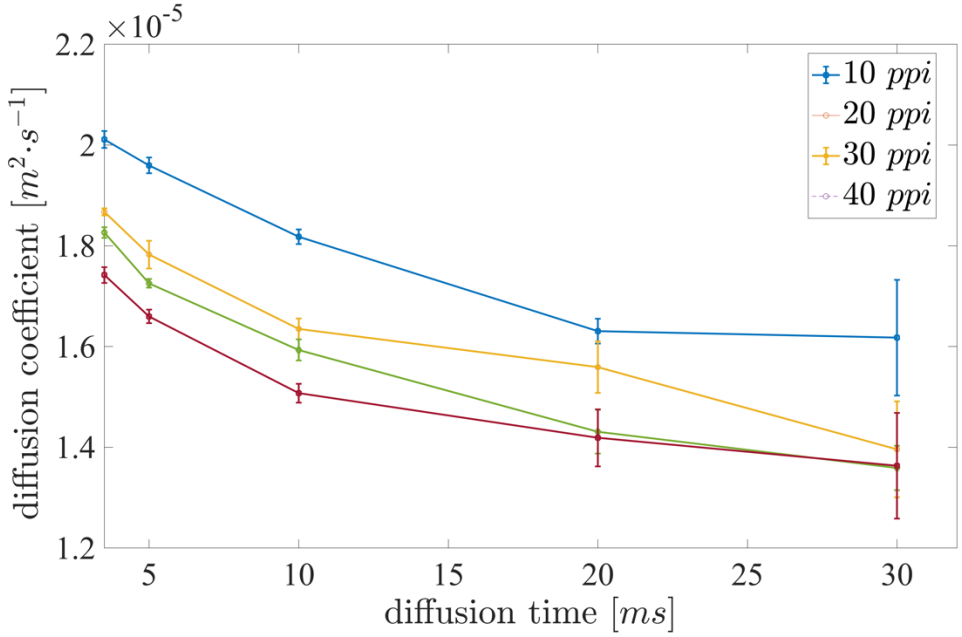

Figure 2.4. Plot of the effective diffusion coefficient in y-direction in ceramic sponges versus diffusion time.

It should be emphasized that each individual sample has its inherent geometrical properties and tortuosity. These inherent properties in the geometry result from the fabrication process and sintering of the ceramics green body, which may cause some deviations in the diffusion coefficient for different samples and along different directions. In addition, the measurement error increases with increasing diffusion time due to reduced SNR.

The determined diffusion coefficients of the 20 and 30 ppi samples have similar values at each observation time. This can be due to rather similar strut diameter of these structures, where the strut diameter of the 20 ppi sample (1.11 mm) is in close proximity to the strut diameter of the 30 ppi (1.22 mm) sponges (see Table 2.1).

The spatially resolved diffusion measurements reveal information about the structure of the ceramic sponges. The method has the flexibility of characterizing an arbitrary voxel element of the sample. Thus, in the future more systematic diffusion studies on a sample can be done (i.e., center versus the edges of the sample). Another advantage of the method is that it is a non-destructive approach using a thermally polarized gas as probing material. Therefore, the characterized structure remains unchanged, which facilitates the analysis of the sample by measurements after certain operating times. Based on this, the alteration of the sample can be quantified before and after the operation. Another interesting application of the current method are measurements on hierarchically supported catalysts, where the spatially resolved approach of the technique may extract important information from these structures. Furthermore, using a gas as probing material with its inherently large diffusion lengths, as done in the presented measurements, allows diffusion studies and the determination of the apparent tortuosity of samples with rather large pores (mm range). Such measurements are not possible with liquids because of the limited diffusion lengths (µm range).

2.4.3. Tortuosity

The tortuosity τ describes the order of hindrance in the sponges as a path-length factor [1,36]. Previously, some values were reported for the tortuosity of 45 ppi sponges in a range between 1.4 to 1.6 using computational fluid dynamic (CFD) [38]. Another study

on solid metal sponges using a numerical approach has estimated the tortuosity for the sponges in a range from 1.179 to 1.208. In their study, no clear effect of pore size on tortuosity was found [39]. Although usually a constant value is reported for the long diffusion time limit, an apparent tortuosity can also be defined dependent on the observation time. This approach facilitates observing the transition from free diffusion to hindered diffusion caused by interaction of the gas molecules with the pore walls. This transition is of great interest for characterizing solid-gas systems, in which both diffusion and flow determine the displacement function.

As the diffusion process in the sponges is influenced by the local heterogeneity and pore distribution, we measured the apparent tortuosity at each diffusion time. The measured values show the effect of macroscopic structure on the transport phenomena in the sponges (cf., Table 2.3). An average diffusion D_{eff} coefficient was calculated for each sponge according to the reported values for three spatial directions in Table 2.2. The diffusion coefficient of free gas was also measured at each observation time Δ, and the apparent tortuosity was calculated by $\frac{D_0}{D_{\mathrm{eff}}}$. However, the spatially resolved approach of the current method allows the investigation of local apparent tortuosity to extract more information about the topology of the volume of interest. Furthermore, the apparent tortuosity can be measured along different directions of the sponges based on the obtained diffusion coefficients (cf., Table 2.2) in order to show the effect of the macroscopic structure of the samples on the apparent tortuosity in an arbitrary direction.

Table 2.3. Apparent tortuosity for the sponge structures determined at various observation times.

	Δ = 5 ms	Δ = 10 ms	Δ = 20 ms	Δ = 30 ms
τ 10 ppi	1.16	1.21	1.40	1.50
τ 20 ppi	1.27	1.32	1.50	1.65
τ 30 ppi	1.30	1.36	1.55	1.64
τ 40 ppi	1.35	1.39	1.52	1.56

2.4.4. Analysis of coated structures

An investigation of coated and uncoated honeycomb and sponge samples was conducted to show the differences between the propagators of both structures. The gas propagators of the raw and coated honeycomb structures are depicted Fig. 2.5 for comparison. The diffusion time was Δ = 10 ms for both samples. Measurements show a remarkable difference between the obtained gas diffusion coefficients along the transversal directions. Diffusion coefficients show a reduction by 37-40% in the coated sample along the transversal direction compared to the raw honeycomb. In addition, the comparison between the baseline values of the propagators in radial direction shows ~500 µm gas displacement difference between the coated and uncoated samples. The narrower peak at zero shows a bigger fraction of trapped methane molecules in the coated honeycomb along each direction (cf., Fig. 2.5). In z-direction, the difference between the gas propagators for coated and uncoated honeycomb is smaller, but the diffusion coefficient is reduced by ~10 % in the coated sample.

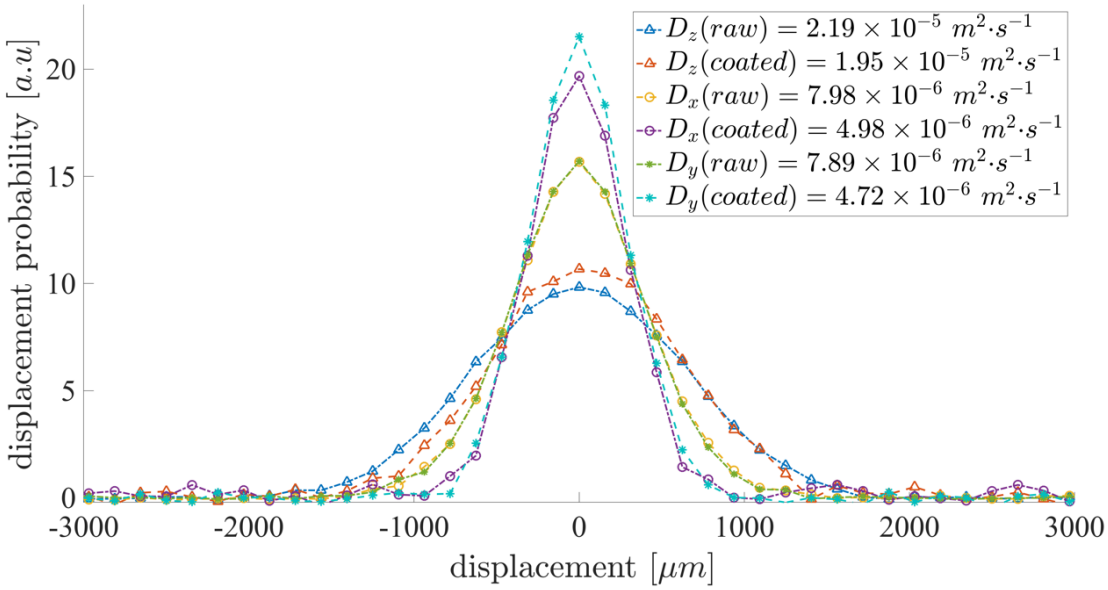

Figure 2.5. Displacement function of methane gas in coated and uncoated honeycomb monoliths at Δ = 10 ms.

The same approach was applied to the coated and uncoated 20 ppi sponge samples using Δ = 5 ms and Δ = 10 ms. A significant difference between the displacement functions of the probing gas in coated and uncoated samples can be observed. The gas propagator shows a transition from a Gaussian to a non-Gaussian displacement function as a result of the increased reflections of the gas on the pore surface. As expected, a lower SNR was obtained for longer diffusion time due to T_1 relaxation losses and shortened transversal relaxation times T_2 and T_2^* in the nickel oxide-alumina coated sample (cf., Fig. 2.6b).

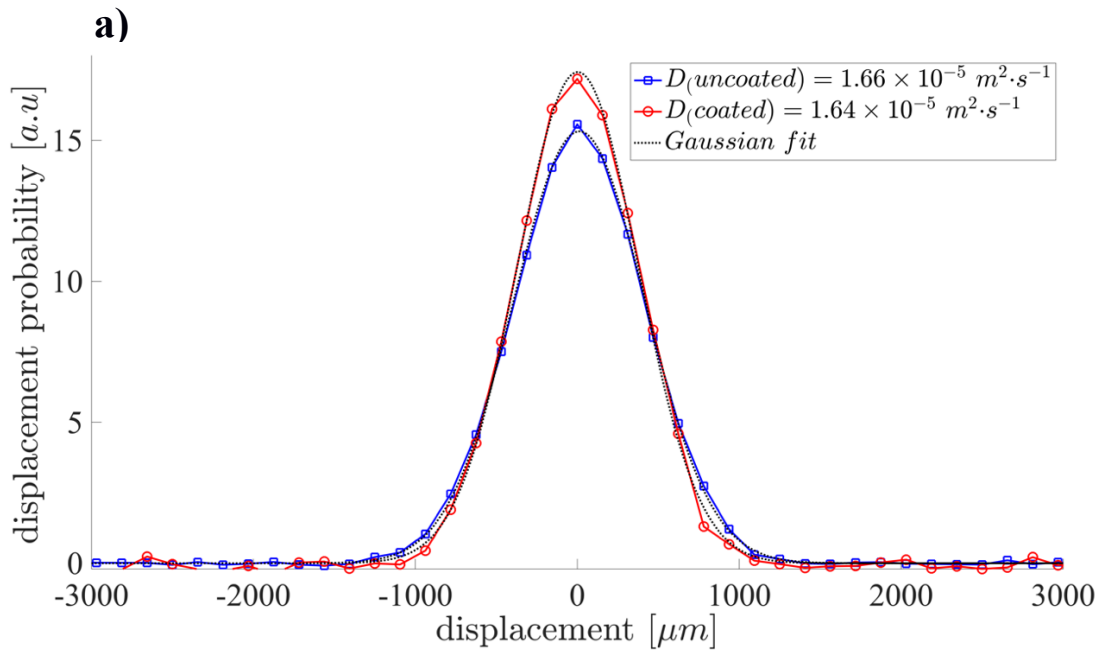

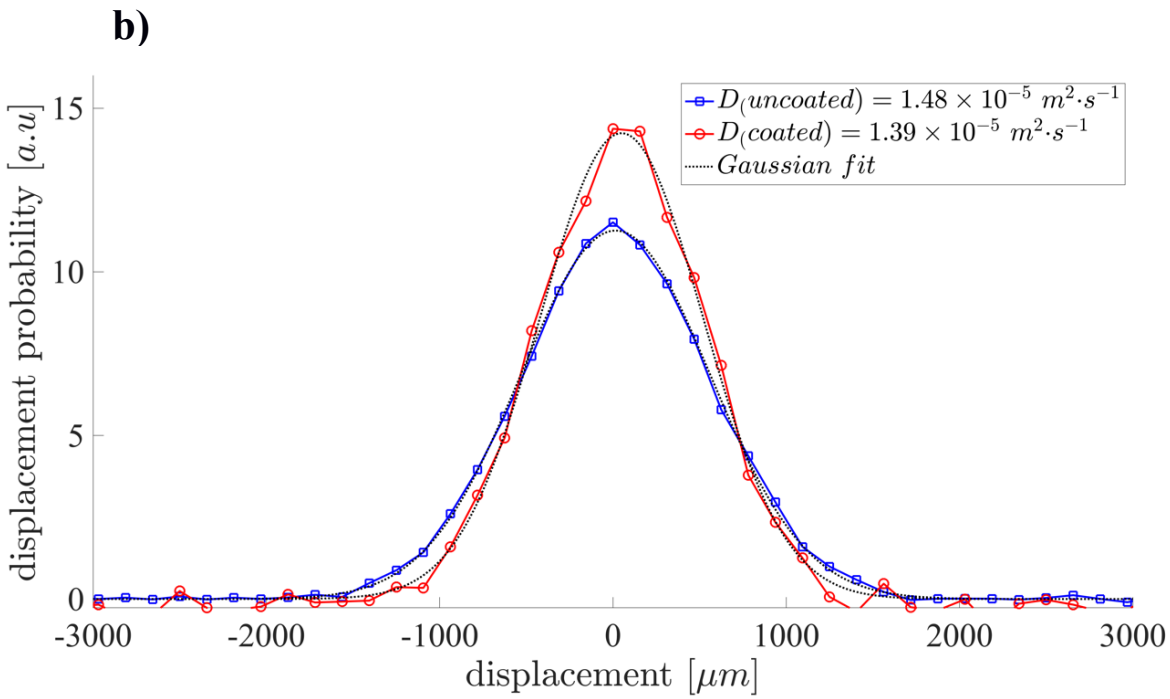

Figure 2.6. Propagators of methane in coated 20 ppi sponge and uncoated 20 ppi at (a) Δ = 5 ms and (b) Δ = 10 ms.

At extended diffusion observation times (Fig. 2.6b) the reduced diffusion coefficients reflect more hindrance than at Δ = 5 ms. For the coated structure, the baseline of the gas propagator, which shows the maximum distance that molecules can travel within the time Δ, is reached at around 1500 µm in in comparison with 2000 µm for the uncoated structure.

2.5. Conclusion

A spatially resolved PFG-STE sequence was successfully applied to monolithic catalyst supports to obtain the displacement function of thermally polarized gas. The diffusion coefficients of gas and the apparent tortuosity of the porous sponges were investigated based on the molecular interaction of gas molecules with the pore walls in an arbitrary volume element of the porous samples for a broad range of diffusion times. While tortuosity is typically understood as a property of pores being tortuous, the apparent tortuosity serves here as a description of the influence the wall interaction has on the particles' diffusion for a given observation time. The method allowed diffusion studies

of methane gas by measuring propagators to characterize the porous samples. The analysis of the gas propagator revealed the effect of the structure on the mean displacement of gas molecules and the diffusion coefficients. The comparative study of coated samples with raw catalyst supports proved the potential of the method by showing even minor changes in displacement functions after adding a thin layer of washcoat on catalyst supports, both in regular or irregular monolithic samples.

Acknowledgments

The project was supported by German Research Foundation (DFG) in the frame of Research Training Group GRK 1860 “Micro-, meso- and macro-porous nonmetallic Materials: Fundamentals and Applications” (MIMENIMA). We are grateful to Dr. Lars Kiewidt for the characterization of sponges and to Dr. Peter Erhard for helpful comments on the manuscript.

References

[1] S.L. Codd, S.A. Altobelli, A PGSE study of propane gas flow through model porous bead packs, J. Magn. Reson. 163 (2003) 16–22. https://doi.org/10.1016/S1090-7807(03)00111-3.

[2] W.S. Price, NMR studies of translational motion, Cambridge University Press, 2009. https://doi.org/10.1017/CBO9780511770487.

[3] J. Wood, L.F. Gladden, Effect of coke deposition upon pore structure and self-diffusion in deactivated industrial hydroprocessing catalysts, Appl. Catal. A Gen. 249 (2003) 241–253. https://doi.org/10.1016/S0926-860X(03)00200-X.

[4] E.O. Stejskal, J.E. Tanner, Spin diffusion measurements: Spin echoes in the presence of a time-dependent field gradient, J. Chem. Phys. 42 (1965) 288–292. https://doi.org/10.1063/1.1695690.

[5] R. Dawson, F. Khoury, R. Kobayashi, Self-diffusion measurements in methane by pulsed nuclear magnetic resonance, AIChE J. 16 (1970) 725–729. https://doi.org/10.1002/aic.690160507.

[6] L.F. Gladden, J. Mitchell, Measuring adsorption, diffusion and flow in chemical engineering: Applications of magnetic resonance to porous media, New J. Phys. 13 (2011) 035001. https://doi.org/10.1088/1367-2630/13/3/035001.

[7] M. V. Twigg, J.T. Richardson, Fundamentals and applications of structured ceramic foam catalysts, Ind. Eng. Chem. Res. 46 (2007) 4166–4177. https://doi.org/10.1021/ie061122o.

[8] G. Groppi, E. Tronconi, Honeycomb supports with high thermal conductivity for gas/solid chemical processes, Catal. Today. 105 (2005) 297–304. https://doi.org/10.1016/J.CATTOD.2005.06.041.

[9] J. Große, B. Dietrich, H. Martin, M. Kind, J. Vicente, E.H. Hardy, Volume image analysis of ceramic sponges, Chem. Eng. Technol. 31 (2008) 307–314. https://doi.org/10.1002/ceat.200700403.

[10] C. Van Gulijk, M.J.G. Linders, T. Valdés-Solís, F. Kapteijn, Intrinsic channel maldistribution in monolithic catalyst support structures, Chem. Eng. J. 109 (2005) 89–96. https://doi.org/10.1016/j.cej.2005.03.013.

[11] I. V. Koptyug, L.Y. Khitrina, V.N. Parmon, R.Z. Sagdeev, NMR imaging of mass transport and related phenomena in porous catalysts and sorbents, in: Magn. Reson. Imaging, 2001: pp. 531–534. https://doi.org/10.1016/S0730-725X(01)00286-7.

[12] J. Grosse, B. Dietrich, G.I. Garrido, P. Habisreuther, N. Zarzalis, H. Martin, M. Kind, K.C. Bettina, Morphological characterization of ceramic sponges for applications in chemical engineering, Ind. Eng. Chem. Res. 48 (2009) 10395–10401. https://doi.org/10.1021/ie900651c.

[13] A.A. Lysova, J.A. Bergwerff, L. Espinosa-Alonso, B.M. Weckhuysen, I. V. Koptyug, Magnetic resonance imaging as an emerging tool for studying the preparation of supported catalysts, Appl. Catal. A Gen. 374 (2010) 126–136. https://doi.org/10.1016/j.apcata.2009.11.038.

[14] I. V. Koptyug, L.Y. Ilyina, A. V. Matveev, R.Z. Sagdeev, V.N. Parmon, S.A. Altobelli, Liquid and gas flow and related phenomena in monolithic catalysts studied by1H NMR microimaging, Catal. Today. 69 (2001) 385–392. https://doi.org/10.1016/S0920-5861(01)00396-0.

[15] X.H. Ren, M. Bertmer, S. Stapf, D.E. Demco, B. Blümich, C. Kern, A. Jess, Deactivation and regeneration of a naphtha reforming catalyst, Appl. Catal. A Gen. 228 (2002) 39–52. https://doi.org/10.1016/S0926-860X(01)00958-9.

[16] T.G.A. Youngs, D. Weber, L.F. Gladden, C. Hardacre, Liquid structure and dynamics of aqueous isopropanol over γ-alumina, J. Phys. Chem. C. 113 (2009) 21342–21352. https://doi.org/10.1021/jp906677c.

[17] M.H. Haider, C. D'Agostino, N.F. Dummer, M.D. Mantle, L.F. Gladden, D.W. Knight, D.J. Willock, D.J. Morgan, S.H. Taylor, G.J. Hutchings, The effect of grafting zirconia and ceria onto alumina as a support for silicotungstic acid for the catalytic dehydration of glycerol to acrolein, Chem. - A Eur. J. 24 (2014) 1743–1752. https://doi.org/10.1002/chem.201302348.

[18] C. D'Agostino, Y. Ryabenkova, P.J. Miedziak, S.H. Taylor, G.J. Hutchings, L.F. Gladden, M.D. Mantle, Deactivation studies of a carbon supported AuPt nanoparticulate catalyst in the liquid-phase aerobic oxidation of 1,2-

propanediol, Catal. Sci. Technol. (2014) 1313–1322. https://doi.org/10.1039/c4cy00027g.

[19] Y. Zhang, L. Xiao, G. Liao, Y.Q. Song, Direct correlation of diffusion and pore size distributions with low field NMR, J. Magn. Reson. 269 (2016) 196–202. https://doi.org/10.1016/j.jmr.2016.06.013.

[20] M. Terekhov, D. Höpfel, Investigation of polymer structure and properties with solid-state and gaseous MRI methods, Chem. Eng. Technol. 29 (2006) 807–815. https://doi.org/10.1002/ceat.200600053.

[21] E.H. Hardy, Magnetic Resonance Imaging in Chemical Engineering: Basics and Practical Aspects, Chem. Eng. Technol. 29 (2006) 785–795. https://doi.org/10.1002/ceat.200600046.

[22] A. Caprihan, C.F.M. Clewett, D.O. Kuethe, E. Fukushima, S.J. Glass, Characterization of partially sintered ceramic powder compacts using fluorinated gas NMR imaging, in: Magn. Reson. Imaging, 2001: pp. 311–317. https://doi.org/10.1016/S0730-725X(01)00242-9.

[23] S.D. Beyea, S.L. Codd, D.O. Kuethe, E. Fukushima, Studies of porous media by thermally polarized gas NMR: Current status, in: Magn. Reson. Imaging, 2003: pp. 201–205. https://doi.org/10.1016/S0730-725X(03)00125-5.

[24] I. V Koptyug, S.A. Altobelli, E. Fukushima, A. V Matveev, R.Z. Sagdeev, Thermally Polarized 1H NMR Microimaging Studies of Liquid and Gas Flow in Monolithic Catalysts, J. Magn. Reson. 147 (2000) 36–42. https://doi.org/10.1006/jmre.2000.2186.

[25] J.E. Tanner, Use of the stimulated echo in nmr diffusion studies, J. Chem. Phys. 52 (1970) 2523–2526. https://doi.org/10.1063/1.1673336.

[26] M. Valentini, Applications of pulsed field gradient spin-echo measurements to the determination of molecular diffusion (and thus size) in organometallic chemistry, Organometallics. 19 (2000) 2551–2555. https://doi.org/10.1021/om000104i.

[27] F. Stallmach, J. Kärger, The potentials of pulsed field gradient NMR for investigation of porous media, Adsorption. 133 (1999) 117–133.

https://doi.org/10.1023/A:1008949607093.

[28] N. Hedin, G.J. DeMartin, K.G. Strohmaier, S.C. Reyes, PFG NMR self-diffusion of propylene in ITQ-29, CaA and NaCaA: Window size and cation effects, Microporous Mesoporous Mater. 98 (2007) 182–188. https://doi.org/10.1016/j.micromeso.2006.08.017.

[29] A. Haase, J. Frahm, D. Matthaei, W. Hanicke, K.D. Merboldt, FLASH imaging. Rapid NMR imaging using low flip-angle pulses, J. Magn. Reson. 67 (1986) 258–266. https://doi.org/10.1016/0022-2364(86)90433-6.

[30] R. Kimmich, F. Winter, W. Nusser, K.H. Spohn, Interactions and fluctuations deduced from proton field-cycling relaxation spectroscopy of polypeptides, DNA, muscles, and algae, J. Magn. Reson. 68 (1986) 263–282. https://doi.org/10.1016/0022-2364(86)90243-X.

[31] I. Tkáč, Z. Starčuk, I.Y. Choi, R. Gruetter, In vivo ^{1}H NMR spectroscopy of rat brain at 1 ms echo time, Magn. Reson. Med. 41 (1999) 649–656. https://doi.org/10.1002/(SICI)1522-2594(199904)41:4<649::AID-MRM2>3.0.CO;2-G.

[32] D.G. Cory, A.N. Garroway, Measurement of translational displacement probabilities by NMR: An indicator of compartmentation, Magn. Reson. Med. 14 (1990) 435–444. https://doi.org/10.1002/mrm.1910140303.

[33] P.T. Callaghan, D. MacGowan, K.J. Packer, F.O. Zelaya, High-resolution q-space imaging in porous structures, J. Magn. Reson. 90 (1990) 177–182. https://doi.org/10.1016/0022-2364(90)90376-K.

[34] L. Kiewidt, J. Thöming, Predicting optimal temperature profiles in single-stage fixed-bed reactors for CO2 methanation, Chem. Eng. Sci. 132 (2015) 59–71. https://doi.org/10.1016/j.ces.2015.03.068.

[35] B. Soher, D. Semanchuk, D. Todd, J. Steinberg, K. Young, VESPA: Integrated applications for RF pulse design, spectral simulation and MRS data analysis, Proc. 19th Annu. Meet. ISMRM. 19 (2011) 1410. http://scion.duhs.duke.edu/vespa/%0Ahttp://www.swig.org.

[36] J.W. M.D. Lechner, Gases in Gases, Liquids and their Mixtures, 2007.

[37] A.H. Kristensen, A. Thorbjørn, M.P. Jensen, M. Pedersen, P. Moldrup, Gas-phase diffusivity and tortuosity of structured soils, J. Contam. Hydrol. 115 (2010) 26–33. https://doi.org/10.1016/j.jconhyd.2010.03.003.

[38] P. Habisreuther, N. Djordjevic, N. Zarzalis, Statistical distribution of residence time and tortuosity of flow through open-cell foams, Chem. Eng. Sci. 64 (2009) 4943–4954. https://doi.org/10.1016/j.ces.2009.07.033.

[39] J. Vicente, F. Topin, J.-V. Daurelle, Open Celled Material Structural Properties Measurement: From Morphology To Transport Properties, Mater. Trans. 47 (2006) 2195–2202. https://doi.org/10.2320/matertrans.47.2195.

Chapter 3

Dispersion*

Abstract: A micro-scale analysis of mass transport in ceramic foams that are used as catalyst supports in gas phase reactions is of high interest. Although the effects of flow rate and foam parameters on the radial and axial dispersion are known for liquid flows, no pore-scale experimental analysis has been yet reported to correlate the mechanical and diffusional dispersion of gas flows to the geometry of open-cell foams. Here, a spatially resolved Pulsed Field Gradient NMR method is applied to determine dispersion coefficients of thermally polarized gas along axial and transversal directions of open-cell foams. The comparative study of three commercial foam samples with different morphologies shows the effect of open porosity, window size, and flow rate on gas dispersion. Additionally, the influence of mechanical and diffusional dispersion at each flow rate is investigated for individual samples. By observing the transition from diffusional dispersion to mechanically driven dispersion of gas, it is found that diffusional dispersion plays an important role, even at higher flow rates after a transition from Darcy to Darcy-Forchheimer regime occurs. The measured values for dispersion coefficients of methane can be directly used in pseudo-heterogeneous models for the methanation reaction.

Keywords: dispersion coefficient, axial and radial dispersion, NMR, foam catalyst support, gas.

* The content of this chapter has already been published: **Mirdrikvand, M.**, Sadeghi, M., Karim, M.N., Thöming, J. and Dreher, W., 2020. Pore-scale analysis of axial and radial dispersion coefficients of gas flow in macroporous foam monoliths using NMR-based displacement measurements. *Chemical Engineering Journal*, *388*, p.124234.

3.1. Introduction

Open-cell foams have been increasingly considered in process engineering applications during the past 20 years [1–7]. The foams are being used as catalyst carriers in heterogeneously catalyzed gas phase reactions because of their low pressure drop, high specific surface area, and most importantly excellent mass and heat transport properties which enhance the local rate of the heterogeneous reactions [1,4,7]. The investigation of gas mass transport in opaque foams can directly support simulations using pseudo-heterogeneous models to predict gas phase reactions such as methanation of CO or CO_2. Among mass transport properties, dispersion coefficients in both radial and axial directions are of high interest to be used in the numerical simulations [8]. At macroscopic level, axial and radial dispersions of gas flow contribute to mass transport based on two-dimensional convection-diffusion equation (Eq. 3.1) in cylindrical coordinates (r, φ, z), where $D_{\parallel}$ and $D_{\perp}$ are the axial and radial dispersion coefficient, respectively.

$$\frac{\partial C}{\partial t} = D_{\parallel}\frac{\partial^2 C}{\partial z^2} - \bar{u}\frac{\partial C}{\partial z} + D_{\perp}\left(\frac{\partial^2 C}{\partial r^2} + \frac{1}{r}\frac{\partial C}{\partial r}\right). \tag{3.1}$$

The equation remains valid as long as mass transport occurs in path lengths greater than the characteristic pore size. In Eq. 3.1, C stands for concentration, and $\bar{u}$ for average velocity [9–11]. Thus, the dispersion of gas in foams in both radial and axial direction is characterized by the dispersion coefficient (D_{disp}) and can be associated with contributions of diffusional and mechanical dispersion [12]. If an analytical method allows to measure dispersion coefficients in the validity range of Eq. 3.1, the results can be used in numerical solutions based on Eq. 3.1.

Although the effect of the foam's geometry on the mass transport properties has already been recognized [13,14], most often radial and axial dispersion coefficients have been predicted using merely the analogy between heat and mass transfer or conventional pulse tracer measurement methods. This is due to the great difficulties in precise measurements of gas dispersion to give a pore-scale analysis of gas spreading in foams.

Nevertheless, several studies aimed to overcome these problems and described some geometry-dispersion related aspects using conventional tracer experiments, optical measurements such as particle image velocimetry (PIV), point-wise injection of a tracer, or spectroscopic methods like laser-induced fluorescence (LIF) [4,5,15–18]. For instance, the point-wise injection method was implemented to measure radial dispersion coefficients using various tracers [15,16]. Benz et al. injected methane as tracer to measure radial dispersion coefficients for 10, 20, 30, and 50 ppi foams [15]. Smoke, as another tracer, was used in short ceramic foams with different pore sizes measured at higher flow rates. Conventional tracer experiments were also used to measure the axial dispersion coefficients [4,18,19]. In these studies, axial dispersion was measured based on the tracer residence time and its distribution curves. Häfeli et al. used wire-mesh sensors as well as laser induced fluorescence in porous media, but no distinction in flow behavior was found to relate it to foams' geometrical properties [18,20,21]. PIV [1] and LIF [21] have also been applied to obtain radial dispersion coefficients of water flow in glass made foams with a certain scale-up factor. Although the mentioned studies reported verified values for low Peclet numbers Pe, lower accuracy and scarce experimental data yielded for higher flow rates a correlation between the velocity, and the characteristic pore diameter with ±40% accuracy. In addition, no clear effect of window size, velocity and pore size on gas/liquid flow has been investigated in previous studies, as the majority of the methods focused on downstream and upstream flow and not on flow through the foams. Recently, a promising work has shown the use of magnetic resonance velocimetry (MRV) for water flow in a 40 ppi open-cell foam [22]. The 3D velocity map was used to investigate radial mixing. The effect of geometry on dispersion mechanisms was described to better understand the mechanisms of mass transport in foams for a single Re number. Streamline displacement was extracted to compute mechanical dispersion coefficients after post-processing of the full field MRV results. An exhaustive dispersion analysis for gas flow has still to be done to investigate a possible correlation between gas flow and the foam topology, both in transversal and in axial direction. Furthermore, velocity measurements allow to correlate the effect of

Re numbers in Darcy and Darcy-Forchheimer regime on the dispersion to the foam morphology with a higher certainty compared to the traditional measurement methods.
Nuclear Magnetic Resonance (NMR) offers a variety of approaches in order to measure diffusion, flow, and dispersion of gases in porous media. An advantage of the NMR displacement measurements is their use of a Lagrangian coordinate system [23] by encoding the position of gas molecules prior to and after a certain displacement time, respectively. Labeling and de-labeling the gas molecules allow correlating fluid hydrodynamics to window size, pore diameter, and the open porosity of foams for a very short contact time between gas and solid. While often specific dispersion models are used in the field of chemical engineering [24,25], NMR directly reveals the information on path length of gas flow through the porous sample. In contrast to most measurement approaches, NMR keeps the measured system intact without tracers and no specially designed foam sample is needed in contrast to LIF.
Pulsed field gradient (PFG) sequences have already been used to map flow displacement, diffusion, and dispersion in porous media [26–28]. Since Seymour and Callaghan presented general approaches for flow dispersion measurement [29], several studies have been conducted to determine flow in porous media such as rocks or glass beads [12,30]. This approach has also been applied by other authors for water flow for Stokes regime [9]. Recently, Ferrari et al. have reported a dispersion analysis of water flow in packed bed at low flow rates [26]. Our study is mainly inspired by the work of Seymour and Callaghan [29], in which the dispersion of liquids was investigated in the axial and radial directions. However, this approach is applied to thermally polarized gas and a spatially resolved analysis is performed to observe the dispersion of gas in foams. Since the NMR displacement measurements label ^{1}H protons of methane, no tracer is required in contrast to measurement techniques commonly used in the field of chemical engineering; thus, avoiding a disturbance in flow and making the measurement non-invasive. Accordingly, our recently optimized NMR sequence [31] was used in the current study to investigate mass transport of gas through monolithic foam supports with high accuracy. Here we report on the application of that method for gaining new insights into the combined effects of diffusion and flow (with different flow rates) on the

displacement of molecules. In addition, we quantify the influence of window size, porosity, and intrinsic velocity of the gas on mass transport. In this study, the flow regime covers low and high Pe numbers for foams with different pore densities (10, 20, and 40 ppi) in order to analyze a broad range of gas flow similar to flow rates applied in the methanation reaction. In contrast to traditional measurements for foams (analysis at inlet and outlet), we determine pore-scale dispersion coefficients within the structures using a spatially resolved approach, which allows cross-validation of numerical simulations with the NMR results.

3.2. Theory and Method

The resolution of PFG NMR displacement measurements (in micrometer range) exceeds the conventional spatial resolution that can be achieved in Magnetic Resonance Imaging (MRI). The PFG NMR with the capability of measuring displacements in a volume-of-interest (VOI) can be employed to conduct measurements in a certain part of a catalysts support in the reactor. This is contrary to common applications of PFG methods used for a global analysis of whole samples. Thus, the localized PFG NMR method is a powerful toolkit for measuring dispersion coefficients of gas in a certain VOI of open-cell foams [31] by tracking hydrogen (^{1}H) containing materials flowing through the porous medium. For thermally polarized gases, a considerably lower Signal-to-Noise Ratio (SNR) is expected as compared to liquids. This is mainly due to lower spin density and shorter transversal relaxation times T_2 in gases. Therefore, optimized PFG sequences are essential to minimize SNR losses to provide precise information on diffusion and flow in foams in µm range.

In this study a volume selective stimulated echo (STE) pulse sequence [32] was employed to measure displacement of gas in a desired volume element (Voxel) with arbitrary orientation. Fig. 3.1 displays the applied PFG-STE sequence. Asymmetric RF pulses were used to reduce the minimum echo time TE and consequently signal losses by T_2 relaxation [33]. Diffusion sensitizing gradients (columns with horizontal dashed lines in Fig. 3.1) in axial and radial direction are used between the first and the second 90° RF pulse as well as between the third RF pulse and the beginning of data acquisition.

Rephasing or dephasing gradients were applied immediately after or prior to the slice selection gradients (cf. Fig. 3.1) to reduce diffusion weighting effects during slice selection. In addition, spoiler gradients were applied during the mixing time (T_m) and a two-step phase cycle was used for the first 90° pulse to suppress unwanted signal contributions. A detailed description of the optimized pulse sequence was given in a previous study on diffusiometry of methane gas in foams [31]. The basic principles of measuring translational displacement probabilities by NMR are described in previous studies [34–36]. For most measurements, a VOI of 12×12×12 mm^3 was chosen to measure gas dispersion in a representative volume of the sample, including the sample center, where the flow mixes in the interconnected network of the foam's pores (cf. Fig. 3.2). Additionally, another VOI size of 16×16×16 mm^3 was used to evaluate to what extent the voxel size affects the estimated radial and axial dispersion coefficients.

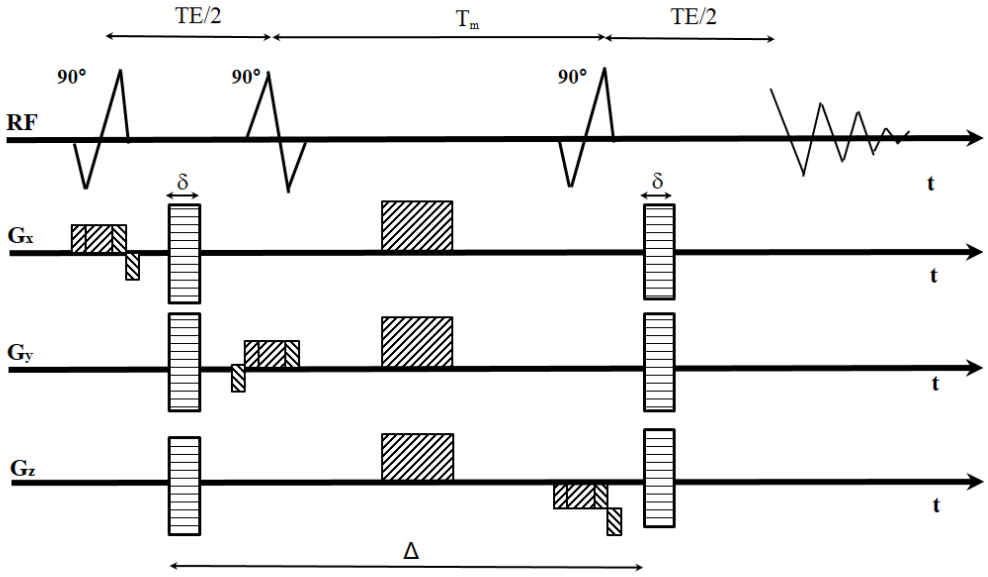

Figure 3.1. Scheme of the applied PFG-STE sequence used for displacement measurements (not to scale). Voxel selection is performed by the three 90° pulses with orthogonal slice orientation. A two-step phase cycle and spoiler gradients within the mixing time T_m. are used to eliminate signals other than the stimulated echo.

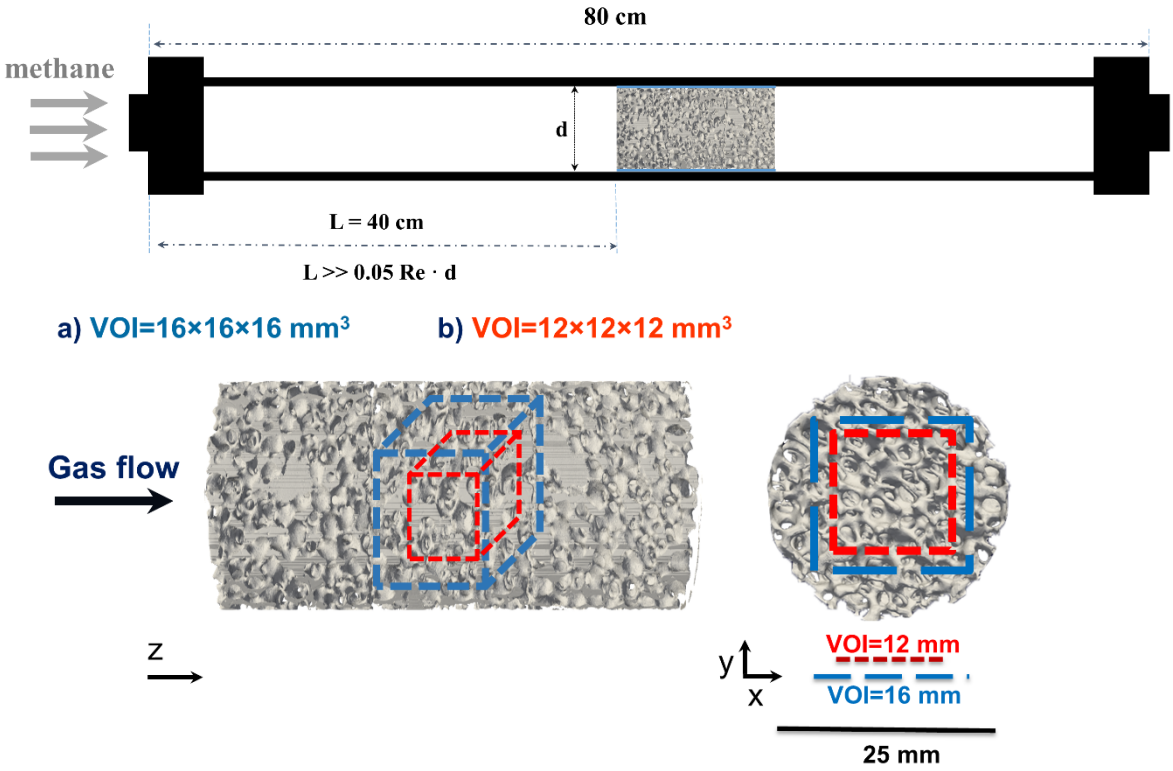

Figure 3.2. Experimental setup and volumes-of-interest used for the PFG-STE measurements. a) VOI = 16×16×16 mm^3 and b) VOI = 12×12×12 mm^3.

In case of unrestricted Gaussian diffusion, the diffusion coefficient or, more generally, the dispersion coefficient can be obtained from at least two measurements performed with different diffusion weighting described by the so-called b-value $b = \gamma^2 \cdot \delta^2 \cdot {G_d}^2 \left(\Delta - \frac{\delta}{3}\right)$, where G_d is the amplitude of the two identical diffusion weighting gradients, δ is the duration of the diffusion sensitizing gradients, and $\Delta - \delta/3$ is the observation time. However, in this study the observation time can be approximated by Δ because $\frac{\delta}{3} \ll \Delta$ (cf. section 3.3.2). The amplitude of the measured *STE* signal is given as a function of the dispersion coefficient D by

$$S = S_0 \cdot e^{\frac{-TE}{T_2}} \cdot e^{\frac{-T_m}{T_1}} \cdot e^{-b \cdot D} \tag{3.2}$$

S_0 is the signal amplitude if relaxation losses and diffusion weighting are negligible. Relaxation losses during the echo time TE are determined by the transverse relaxation time T_2, while during the mixing time T_m the relaxation related signal decay depends on the longitudinal relaxation time T_1 (cf., Fig. 3.1).
By incrementing the q-value defined in Eq. 3.3, the echo signal may be written as a function of q and the displacement probability P [23,34,36] for the time interval Δ.

$$q = \gamma \cdot \delta \cdot G_d \tag{3.3}$$

$$S(q) = \int \rho(r_0) \int P(r_0|r, \Delta)\, e^{iq(r-r_0)}\, dr dr_0 \tag{3.4}$$

Note that in all measurements $\delta \ll \Delta$ should be satisfied.
Displacement function: The displacement probability or, in other words, the gas propagator can be derived by Fourier transformation of the STE signal as function of q. Thus, the probability that spins have been displaced by the path length $(r - r_0)$ during the observation time Δ can be calculated. Some characteristic values can be used for the description of the gas propagators. For instance, the full width at half maximum (FWHM) $\Delta\nu_{1/2}$ is a characteristic that describes how wide the displacement is. The maximum displacement length ($\Delta L_{\max}$) can be calculated from the tails of the displacement probability, where the function approaches the x-axis. $\Delta L_{\max}$ indicates the maximal displacement of the gas ensemble within the given observation time for NMR measurement. This length can be compared to the window diameter of the foams samples at different flow rates.
Dispersion coefficient: In case of a Gaussian distribution, the dispersion coefficient D can be calculated in two ways. Using the probability density for 1-dimensional Gaussian diffusion [37] the dispersion coefficient can be estimated by using its dependence on $\Delta\nu_{1/2}$:

$$D = (\Delta \nu_{1/2})^2/(16 \log(2)(\Delta - \delta/3)), \quad (3.5)$$

or D can be calculated by fitting the measured data to Eq. 3.2. If a log-linear fit of the initial time-domain signal or the peak area in the frequency domain versus b-values is used, data measured at large b-values should be excluded because deviations from the expected log-linear fit will occur at low SNR. In case of expected non-Gaussian probability distributions, the restriction to low q-values ("low q-value limit") is of particular importance because this range of q-values allows to estimate dispersion coefficients using only the data for $b \cdot D \ll 1$ as proposed by Seymour and Callaghan [23]. Alternatively, as mentioned before, the FWHM value of the probability distribution can be used to estimate D.

3.3. Materials and methods

3.3.1. Ceramic foams

Al_2O_3 foams (length: 23 mm, diameter: 25 mm, 10, 20, and 40 pores per inch (ppi); Hofmann CERAMIC GmbH, Breitscheid, Germany) were inserted into a cylindrical glass model reactor (length: 80 cm, inner diameter: 26 mm). Methane was supplied as probing gas through a mass flow controller (Bronkhorst Deutschland Nord GmbH, Kamen, Germany). The pressure was measured at the inlet and outlet of the experimental setup. In all measurements, the operational pressure and the temperature were 1.3 bar and 16-17 °C, respectively. The geometrical characteristics of the samples were obtained by μ-CT imaging (see Table 3.1, Fig. 3.3). The size of window diameter, pore density, strut diameter, and open porosity of the samples are given in Table 3.1. The samples were inserted tightly into the model reactor to prevent unwanted bypass flow through the free space between the samples and the reactor wall. The hydrodynamic entry length was long enough to ensure that the flow is fully developed when it enters the structure.

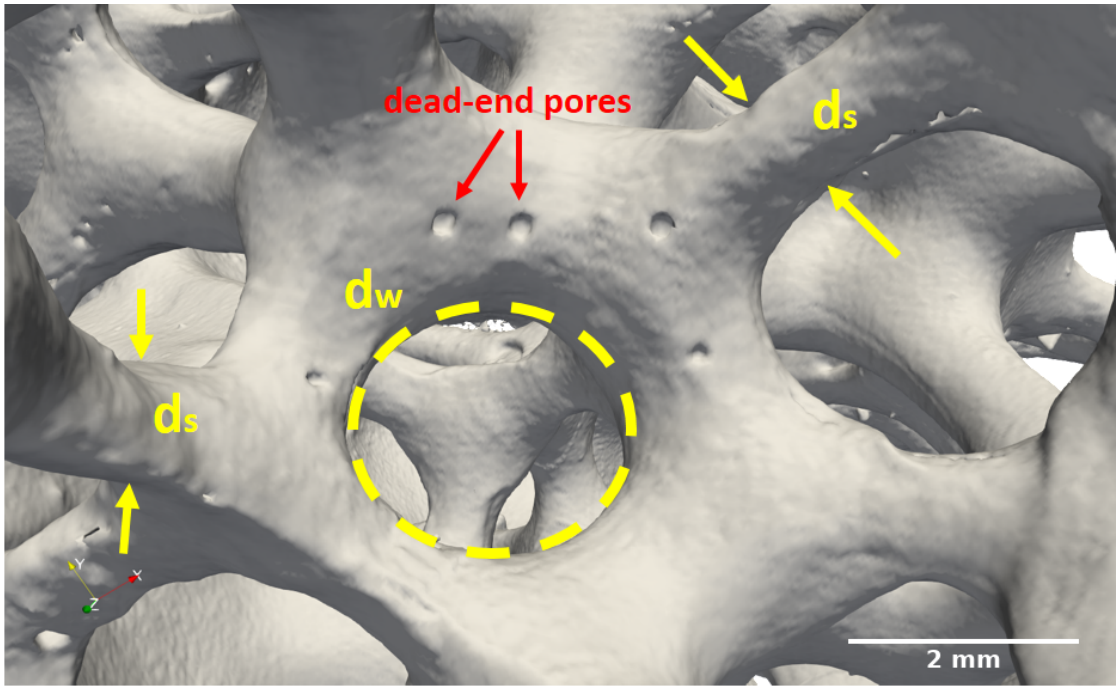

Figure 3.3. Characteristics of foam in a typical µ-CT image: window diameter (d_w), strut diameter (d_s), and dead-end pores.

3.3.1.1. Ceramic foam morphology

Different methods such as gravimetric analysis, tetrakaidecahedral unit cell model, and µ-CT volume imaging technique were utilized to characterize the morphological properties of the samples. The mass and volume of samples were measured by standard lab-scale and caliper. The open porosity, specific surface area, window, and pore distribution of samples were determined via image processing of a set of 2D µ-CT images. In this method, 3D representative elementary volumes of the sponges were reconstructed and then analyzed. The pore diameter was defined as mean diameter of spheres of equivalent volume. Finally, the strut diameter and the specific surface area of the foams were calculated from µ-CT data using the proposed unit cell model by Inayat et al. [38].

Table 3.1. Characteristics of foams (a: µ-CT, b: tetrakaidecahedral unit cell model).

Sample / Pore density (ppi)	Open porosity [a] (ε)	Pore diameter [a] (d_p) (mm)	Window diameter [a] (d_w) (mm)	Strut diameter [b] (d_s) (mm)	Specific surface area [a] (S_v) ($m^2 \cdot m^{-3}$)
10 ppi	0.67	5.35±0.38	3.20±0.77	2.21	544.48[a], 595.11[b]
20 ppi	0.77	3.45±0.16	2.40±0.58	1.10	785.71[a], 797.59[b]
40 ppi	0.79	2.37±0.30	1.43±0.39	0.73	1105.80 [a], (866.00)[b]

3.3.2. Flow characteristics

Various flow rates ranging from 0.10 to 2.25 $L \cdot min^{-1}$ (inlet superficial velocity: 3.39-76.39 $mm \cdot s^{-1}$) were applied to investigate gas dispersion in axial and radial direction. The flow regime can be described with dimensionless numbers. The calculation of the Reynolds number Re *and* Re_p, is based on Eq. 3.6 using u for the intrinsic velocity of gas bulk, ν for the dynamic viscosity, and either the diameter of the reactor d or the mean pore diameter d_p of each foam. The Peclet number Pe is defined by Eq. 3.7 with D_eff being the effective diffusion constant of methane in the absence of flow.

$$Re_{(p)} = \frac{u_{bulk} \cdot d_{(p)}}{\nu} \tag{3.6}$$

$$Pe = \frac{u_{bulk} \cdot d}{D_{eff}} \tag{3.7}$$

The calculated pore Reynolds number (Re_p) values are in a range of 0.48 to 24.51. The applied flow rates correspond to Reynold numbers (Re) based on the reactor diameter ranging from 5 to 114 and Pe numbers of 3.85-86 for the bulk flow. Therefore, the bulk flow remains in the Darcy and Darcy-Forchheimer regime, wherein the flow is dominated by inertial forces [39–41].

3.3.3. NMR displacement measurements

A 7 Tesla preclinical NMR imaging system (Biospec 70/20, Bruker Biospin GmbH, Ettlingen, Germany) equipped with a gradient system BGA12S2 (maximum gradient strength of 441 $mT \cdot m^{-1}$ in each direction, rise time 130 µs) was used for all measurements. For RF excitation and signal detection a quadrature birdcage RF coil (inner diameter of 72 mm) was used. Paravision 5.1 was used as the interface for implementing the pulse sequence and performing the PFG NMR measurements.

Prior to each measurement the samples were imaged using a 3D gradient-echo MRI sequence in order to adjust the VOI. The parameters were as follows: Repetition time TR: 25 ms, echo time TE: 0.5 ms, flip angle: 45°, two averages, Field-of-View (FOV): 64×64×96 mm^3, matrix size: 192×192×16, total measurement time: 2 min 33 s.

The volume selective PFG-STE sequence used asymmetric 90° RF pulses of 500 µs duration, voxel size: 12×12×12 or 16×16×16 mm^3, 64 equidistant q-space values, displacement range +/-5 mm, 1024 complex data points sampled with 25 kHz. For ^1H measurements of methane performed at 300 MHz, ambient temperature, and atmospheric pressure, a T_1 value of 20-25 ms is expected [42]. Thus, saturation effects were avoided by using a repetition time of 250 ms.

Measurements were performed with a TE of 2.6 ms, δ of 0.25 ms, and Δ of 10 ms. Additionally, in some measurements a Δ *of* 20 ms was used. In order to increase the SNR, 32 averages were used for all the measurements with encoding gradients in axial and radial direction, where z corresponds to the axial direction and y corresponds to the radial direction of the foams. The total measurement time of each measurement was 8 min 23 s.

An in-house MATLAB (R2017b, The MathWorks, Inc., Natick, USA) script was used for processing the time-domain data. The propagator was calculated from the time-domain signal applying Hamming apodization and 1D Fourier transformation along the time domain, followed by peak integration and 1D Fourier transformation along variable q.

In order to estimate dispersion coefficients, several processing steps were performed. The baseline of the Fourier transformed spectra was corrected using a fifth-order

function. Then, zero-order phase correction was applied for the one half (32 q-steps) of the spectra. Subsequently, the peak area was integrated and the obtained values were plotted against b-values to determine the dispersion coefficient at each flow rate. Alternatively, the dispersion coefficient was estimated from the FWHM value.

3.4. Result and discussion

The results are divided into two sections. Firstly, axial dispersion coefficients and secondly radial dispersion coefficients are investigated. In each section, the effect of flow rate, window size, strut diameter, open porosity, and VOI on gas displacement is evaluated.

3.4.1. Axial dispersion

3.4.1.1. Flow rate effect

In Fig. 3.4, the gas propagators measured for 10, 20, and 40 ppi samples are normalized to constant area for better comparison. While the gas propagators form Gaussian distributions for lower flow rates, increasing asymmetry of the propagators is observed at higher flow rates. The calculated $\Delta L_{\max}$ values show that in each sample the flow reaches the long displacement regime at higher flow rates [9]. Therefore, the dispersion coefficients, which have been obtained in the current analysis by measurements as described below, are suitable to be used in the convection diffusion equation (Eq. 3.1) in numerical simulations.

As can be seen in Fig. 3.4, the propagators of all samples shift toward the flow direction and create peaks with positive displacement lengths. No stagnant peak and separation of flow due to dead pores occur as only one peak for each propagator is observed. The peaks of the propagators slightly move toward the flow direction as flow increases from 0.1-0.5 L·min^{-1}. In this range (0.1 to 0.5 L·min^{-1}) the $\Delta L_{\max}$ of the gas ensemble is shorter or comparable to the window size of the foams, used as a characteristic length of the open-cell foams, indicating low interaction of gas flow with pore walls. In this stage the gas propagators indicate that only a small part of the gas molecules interacts with the sample [43]. The stepwise increase of the flow rate gradually affects the mixing

length [12] and the displacement path of the gas in the foams. The peak of the propagators is continuously shifted toward the net flow direction. For higher flow rates, in particular for flow rates above 1.25 L·min^{-1}, the propagators show a wing or shoulder toward the flow direction and form asymmetrical displacement probabilities. For these flow rates, the $\Delta L_{\max}$ is already longer than the window size of all the foams. The asymmetrical distribution of gas displacement corresponds to the transition between Gaussian distributions expected for low and sufficiently high flow rates [43].

In this study, no flow rate > 2.25 L·min^{-1} was measured. However, it can be expected that at longer observation times the propagators again form a Gaussian distribution again indicating enough interactions of gas with the interconnected network of the foams. Such a transition was observed by Koptyug et al. for the case of butane flow through glass beads [43]. Although the short T_1 relaxation time of methane severely affects the SNR, which thus limits the observation time, measurements performed at Δ = 20 ms show a tendency of forming Gaussian displacement functions (c.f. Appendix Fig. S1). For all measured flow rates, the $\Delta L_{\max}$ of gas molecules increases with decreasing pore density ($\Delta L_{max(10\ ppi)} > \Delta L_{\max(20\ \text{ppi})} > \Delta L_{\max(40\ \text{ppi})}$), reflecting the different window size of samples obtained in µ-CT measurements ($d_{\text{w(10 ppi)= 3.2 mm}} > d_{\text{w(20 ppi) = 2.4 mm}} > d_{\text{w(40 ppi) =1.8 mm}}$).

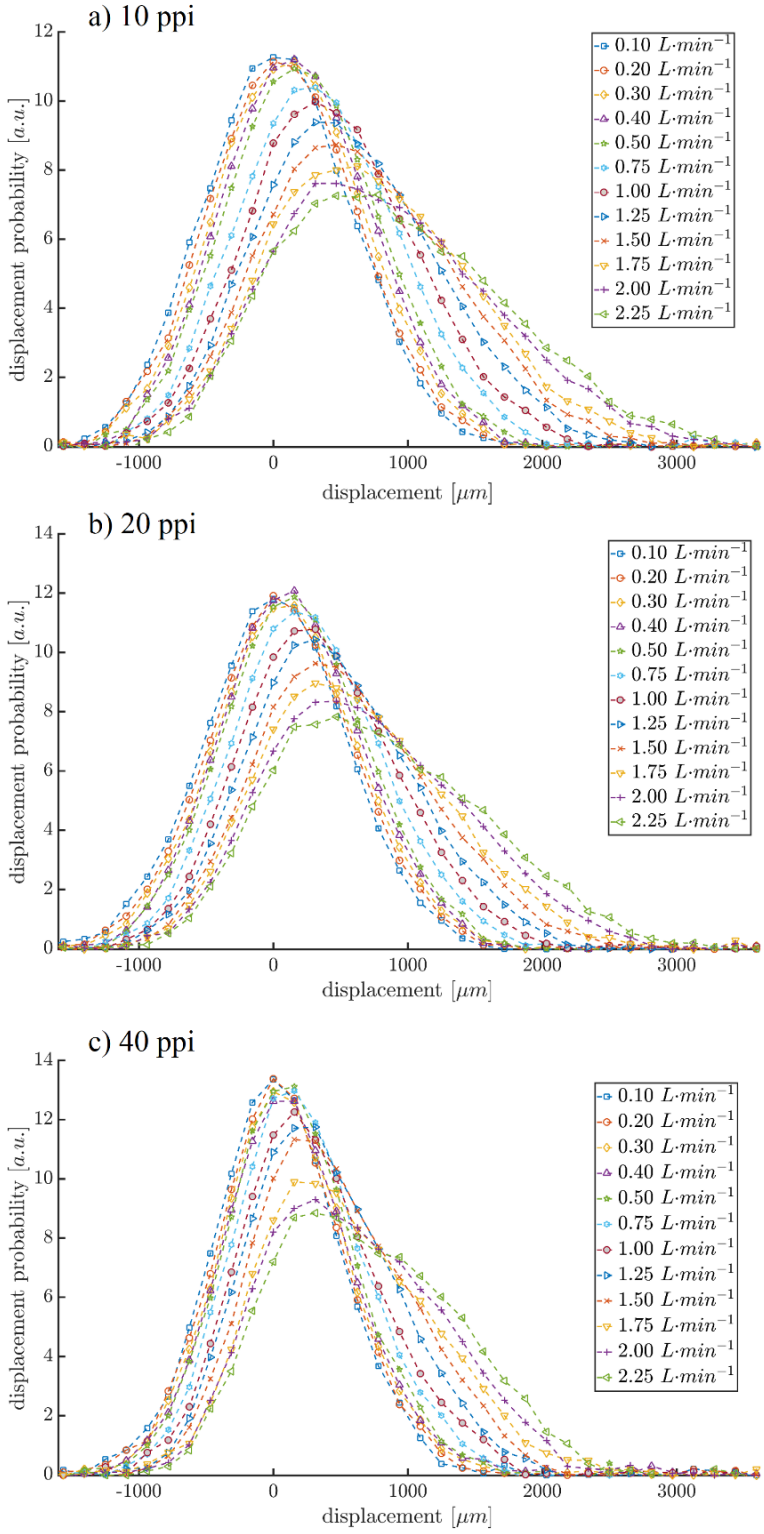

Figure 3.4. Displacement probability at different flow rates for (a) 10 ppi, (b) 20 ppi, and (c) 40 ppi samples.

For a quantitative comparison of all gas propagators FWHM values were used as an indicator of displacement width of the gas ensemble through the foams (c.f. Fig. 3.5). With increasing flow rate, FWHM increases non-linearly. The FWHM value allows to estimate the 'apparent dispersion coefficient' at the measured observation time using Eq. 3.5 derived from a Gaussian distribution. Of course, using D_{app}, i.e., a single scalar parameter, simplifies the characterization of a complex, asymmetric displacement function. However, D_{app} can be used in the numerical solution of the convection-diffusion equation (Eq. 3.1). In the next subsection (3.4.1.2) we use D_{app} to compare the dispersion process of gas for different foam samples, and a detailed description of the calculated axial dispersion coefficients is given in Section 3.4.1.3.

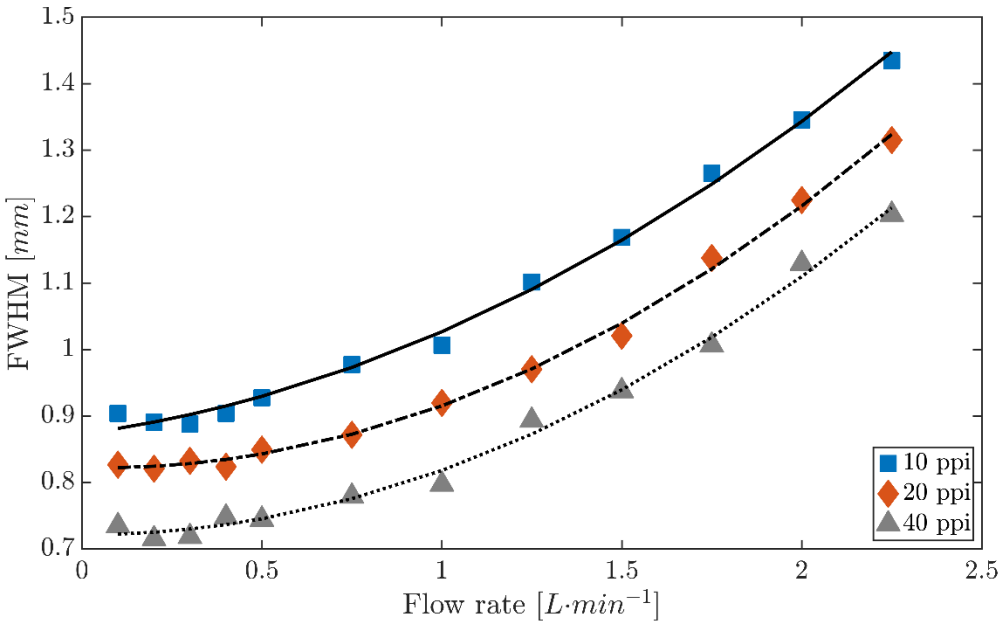

Figure 3.5. FWHM of gas propagators at different flow rates in foams. The dashed lines show an exponential fit to the data obtained for each sample.

3.4.1.2. Diffusion and mechanically induced dispersion

Compared to turbulent flow, much smaller dispersion is expected for laminar flow. This is due to the non-mixing nature of the laminar gas flow. Dispersion consists of two components, diffusion and advection. The accuracy obtained in NMR measurements

enables us to distinguish differences between dispersion mechanisms at different flow rates. The gradual increase in flow rate of foams (c.f., Fig. 3.4) helps to better distinguish the effects of diffusion and advection components on the displacement functions. Although the mean displacement path of gas generally increases when the flow rate increases, at very low flow rates ranging between 0.1 to 0.5 L·min^{-1} (for all samples) no significant mechanically driven dispersion was observed. This finding can be better discussed when the apparent dispersion coefficients D_{app} measured with flow are compared to effective diffusion coefficient D_{eff} of methane measured without flow, which we measured in the same foams without flow obtaining D_{eff} for 10, 20, and 40 ppi samples as follows [31]: $D_{eff(10\ ppi)}$ = (1.73± 0.02)×10^{-5} m^2·s^{-1}, $D_{eff(20\ ppi)}$ = (1.53 ± 0.05)×10^{-5} m^2·s^{-1}, and $D_{eff(40\ ppi)}$ = (1.48 ± 0.03)×10^{-5} m^2·s^{-1}.

The obtained apparent dispersion coefficients for flow rates ranging from 0.1 to 0.5 L·min^{-1} form a plateau (c.f., Fig. 3.5 and Table 3.2), while for flow rates > 0.75 L·min^{-1} a remarkable increase in apparent dispersion coefficient of 20 and 10 ppi samples can be observed (c.f., Table 3.2). This trend occurs for 40 ppi foam at flow rates > 1.25 L·min^{-1}. Note that the minor differences between the measured D_{app} for low flow rates and D_{eff} determined in the previous study might be due to small variations between the samples from the same production line. For all samples, D_{app} becomes larger than D_{eff} for flow rates > 0.5 L·min^{-1}. This suggests that the diffusional component of flow is still the dominant mechanism of mass transport for the lower flow rates, while at higher flow rates (0.75 L·min^{-1} in case of 10 and 20 ppi and 1.25 L·min^{-1} for 40 ppi foam), mass transport is affected by the mechanically driven share of flow. The observed dependence of the FWHM values as a function of the flow corresponds to the transition from the Darcy regime (Re_p < 1) to the Darcy-Forchheimer flow regime, which occurs for flow rates ranging 1< Re_p <10, i.e., up to flow rate of 0.5 L·min^{-1}. This observation underpins the reliability of the measurements to distinguish the transition between the two regimes based on the theory described in literature [39–41]. It is worth mentioning that for all flow rates a portion of negative displacement is

observed. This can predominantly be caused by diffusion and in part, at least for higher flow rates, by back mixing.

3.4.1.3. Axial dispersion coefficient ($D_{\parallel}$)

The axial dispersion coefficients were determined by two methods. First, based on the obtained FWHM of the propagators (Eq. 3.5) and second, from the slope of log-linear fit of the peak area versus $b.$, i.e., signal attenuation (Eq. 3.2) versus the applied b-value in each q step (Fig. 3.6). The linear part of the attenuation indicates Gaussian displacement, typically found as long as $b \cdot D << 1$ [23]. For the latter method, the frequency domain data was phase and baseline corrected to suppress flow effects on the methane spectra in all measurements (cf. section 3.3.3).

Inspection of the signal attenuation in a 20 ppi sample in Fig. 3.5 shows steady increase in dispersion as a consequence of increased flow rate. The dispersion coefficients measured from FWHM of gas propagators were chosen based on two reasons. First, only the lowest four or five q values fulfill $b \cdot D < 1$ and could be used for the log-linear fit. Second, for higher flow rates a non-linear signal decay can be observed even in this low b-values range (c.f., Fig. 3.6). The determined axial dispersion coefficients can be compared with the effective diffusion coefficients reported in the previous publication [31]. As expected, the dispersion coefficients increase with increasing flow rate. The highest and the lowest $D_{\parallel}$ always belong to 10 and 40 ppi samples at identical flow rates, respectively.

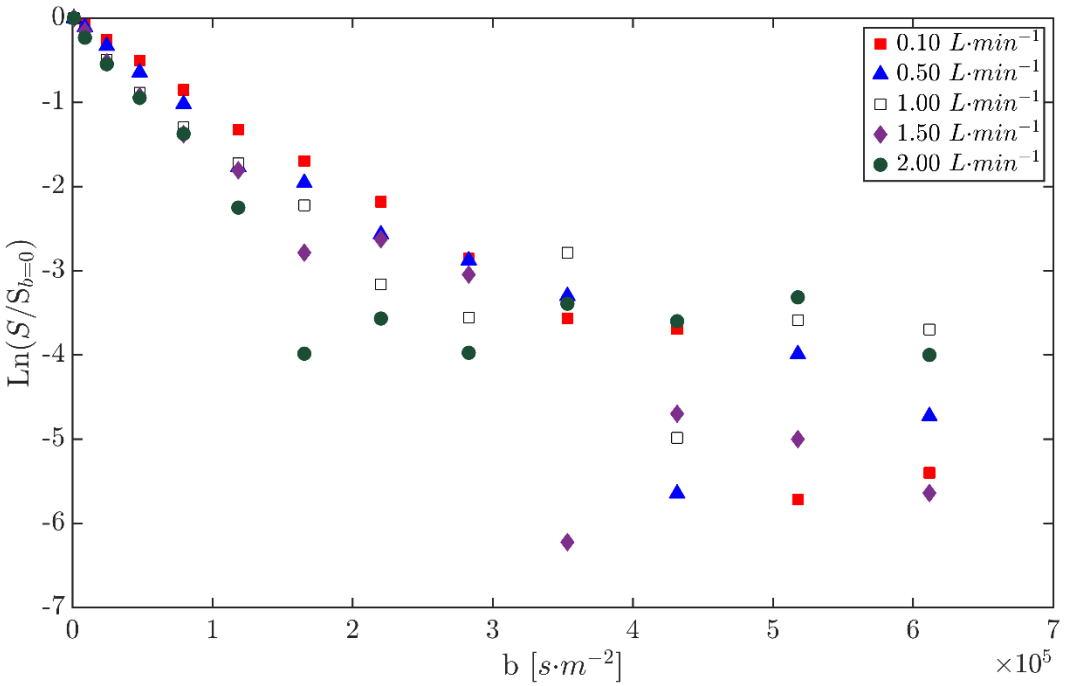

Figure 3.6. Natural logarithm of the signal (peak area) as a function of *b*-value for the 20 ppi foam.

Table 3.2. Axial dispersion coefficient ($D_{\parallel}\times10^5$ $m^2{\cdot}s^{-1}$) obtained for three structures using FWHM values for flow rates ranging from 0.1 to 2.25 $L{\cdot}min^{-1}$.

L·min^{-1}	**0.10**	**0.20**	**0.30**	**0.40**	**0.50**	**0.75**	**1.00**	**1.25**	**1.50**	**1.75**	**2.00**	**2.25**
10 ppi	1.71	1.66	1.65	1.71	1.79	2.00	2.12	2.54	2.86	3.35	3.79	4.31
20 ppi	1.43	1.41	1.45	1.42	1.51	1.59	1.77	1.98	2.20	2.71	3.14	3.62
40 ppi	1.12	1.07	1.08	1.17	1.16	1.28	1.32	1.67	1.84	2.13	2.67	3.02

3.4.1.4. Foam geometry and $D_{\parallel}$

The dispersion coefficient can be correlated to the geometry of each foam as a function of the flow rate or velocity (c.f., Fig. 3.4). Montillet et al. proposed a linear correlation between superficial velocity and axial dispersion of liquid flow in foams [44]. In some studies [25,45], the axial dispersion coefficient has been correlated to the flow-dependent Reynolds number using a power function, $D_{\parallel} = c \cdot Re_p^n$, for fitting data measured for different pore sizes. $D_{\parallel}/D_m$ is illustrated for different flow rates as a

function of Re being the usual scale for industrial approaches (Fig. 3.7). In addition, the ratio between $D_{\parallel}$ and self-diffusion of free methane gas D_m = 2.24×10^{-5} m^2·s^{-1} is plotted [31] against Pe in the Appendix in Fig. S2. The Peclet number describes the ratio of mechanically driven flow to the rate of diffusion. An exponential function (Eq. 3.8) is used to relate the Re or volumetric flow rate to the axial dispersion coefficient in the Darcy-Forchheimer regime as it gave a higher R^2 value compared to other tested functions.

$$D_{\parallel} = \alpha \cdot e^{\beta \cdot Re} \tag{3.8}$$

The values for α are detailed in Table 3.3 for 10, 20, and 40 ppi samples ($R^2 > 0.97$). For all fitted functions β was equal to 0.01. The proposed correlation shows a high precision for fitting $D_{\parallel}$ in the Darcy-Forchheimer regime, where the flow rate ranges between 0.5 and 2.25 L·min^{-1}, corresponding to Re_p values between 2.40 and 24.80 for the samples analyzed.

Table 3.3. Fitting constants for $D_{\parallel}$ versus Re using Eq. 3.7.

Sample	α (mm^2·s^{-1})
10 ppi	1.36
20 ppi	1.11
40 ppi	0.86

The obtained results enabled a precise correlation between axial dispersion coefficient and Re within the measured flow in the Darcy-Forchheimer regime. The exponential fitting was chosen since it gave the best fitted curve (higher R^2 value) compared to linear or power functions mentioned in literature for dispersion of water in mesh wired metal foams [25]. Thus, the given correlation and the exponential fitting is merely achieved based on empirical data, without theoretical background. We do not claim that the exponential fit is suitable for extrapolation to higher flow rates of gas in foams.

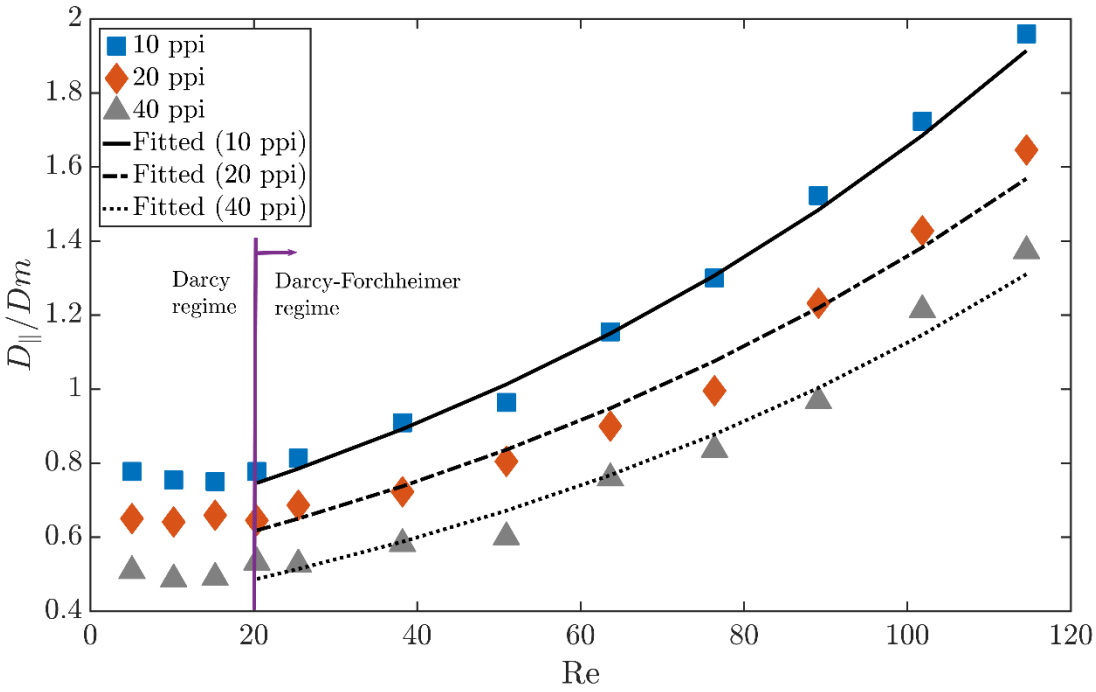

Figure 3.7. Normalized axial dispersion coefficient as a function of *Re* number determined for the three foam types. The superimposed curves are exponential fits to the data.

3.4.1.5. Window size and porosity effect

Beside intrinsic velocity, window size and open porosity are the most important parameters for characterizing mass transport in foams [46]. The first parameter primarily regulates the mixing length of dispersive flow in the structure, whereas the second mainly controls the flow hydrodynamics in the void space of the foam. However, since there is an interaction between window size and open porosity as reported in the literature [46], their effect cannot be fully decoupled and evaluated separately. Minor alteration in the morphology of foams may affect dispersion in both axial and radial directions. Accordingly, we analyzed the effect of window size and porosity on axial dispersion at different *Re* numbers. The window size effect on axial dispersion is compared in Fig. 3.8 for two *Re* numbers. For *Re*~25 (Re_p= 2.41-5.44), corresponding to flow rate of 0.5 L·min^{-1}, the dispersion is still dominated by diffusion (c.f., Fig. 3.8a). For *Re*~76 (Re_p= 7.24-16.34) using a flow rate of 1.5 L·min^{-1}, the dispersion is more

affected by advection (c.f., Fig. 3.8b). Fig. 3.8 also contains the propagators measured on free methane gas with and without flow [31].

The results suggest that the extent of the hindrance of the gas molecules is connected to the windows size in foams considering that the peak of the displacement curves (c.f., Fig. 3.8b, flow rate of 1.5 L·min^{-1}) is observed at 156 µm, 312 and 877 µm for 10, 20 and 40 ppi samples, respectively. The gas propagator for the 40 ppi sample ($\varepsilon = 0.79$) forms the highest and narrowest peak. The pore connectivity also plays a significant role in dispersion of gas in the interconnected network of the foams as the tortuosity ($\tau = {D_m}/{D_{eff}}$) of the foam samples was measured ($\tau_{10\ ppi} < \tau_{20\ ppi} < \tau_{40\ ppi}$) for methane gas [31]. This shows that dispersion is affected by pore distribution and local heterogeneity of foams [47]. Furthermore, the comparison of the maximum displacement ($\Delta L_{max(10\ ppi)} > \Delta L_{max(20\ ppi)} > \Delta L_{\max(40\ \mathrm{ppi})}$) is in agreement with the properties of foams reported in Table 3.1. This trend remains consistent at different flow rates. On the other hand, the possibility of backflow and reflection of gas molecules in the reverse direction of flow is connected to the pore density of samples at a certain flow rate. This can be elucidated by comparing the probability of negative displacement in Fig. 3.8b.

It is worth mentioning that in Fig. 3.8b, which shows data measured at higher Re, the gas flow in the 20 ppi foam forms the maximum at a similar position as for the flowing free gas. In addition, the obtained $D_{\parallel}$ is almost identical to the dispersion coefficient of flowing free gas. This behavior can be associated with the moderate window diameter of 20 ppi samples. A point-wise comparison of the displacement probabilities in propagators of free gas and gas flowing through the 20 ppi sample at 1.5 L·min^{-1} shows an enhanced movement of gas toward the net direction of the gas flow. This finding is in remarkable agreement with a numerical µ-CT based simulation performed to obtain velocity fields in foams of the same production line as those used in the current study [48].

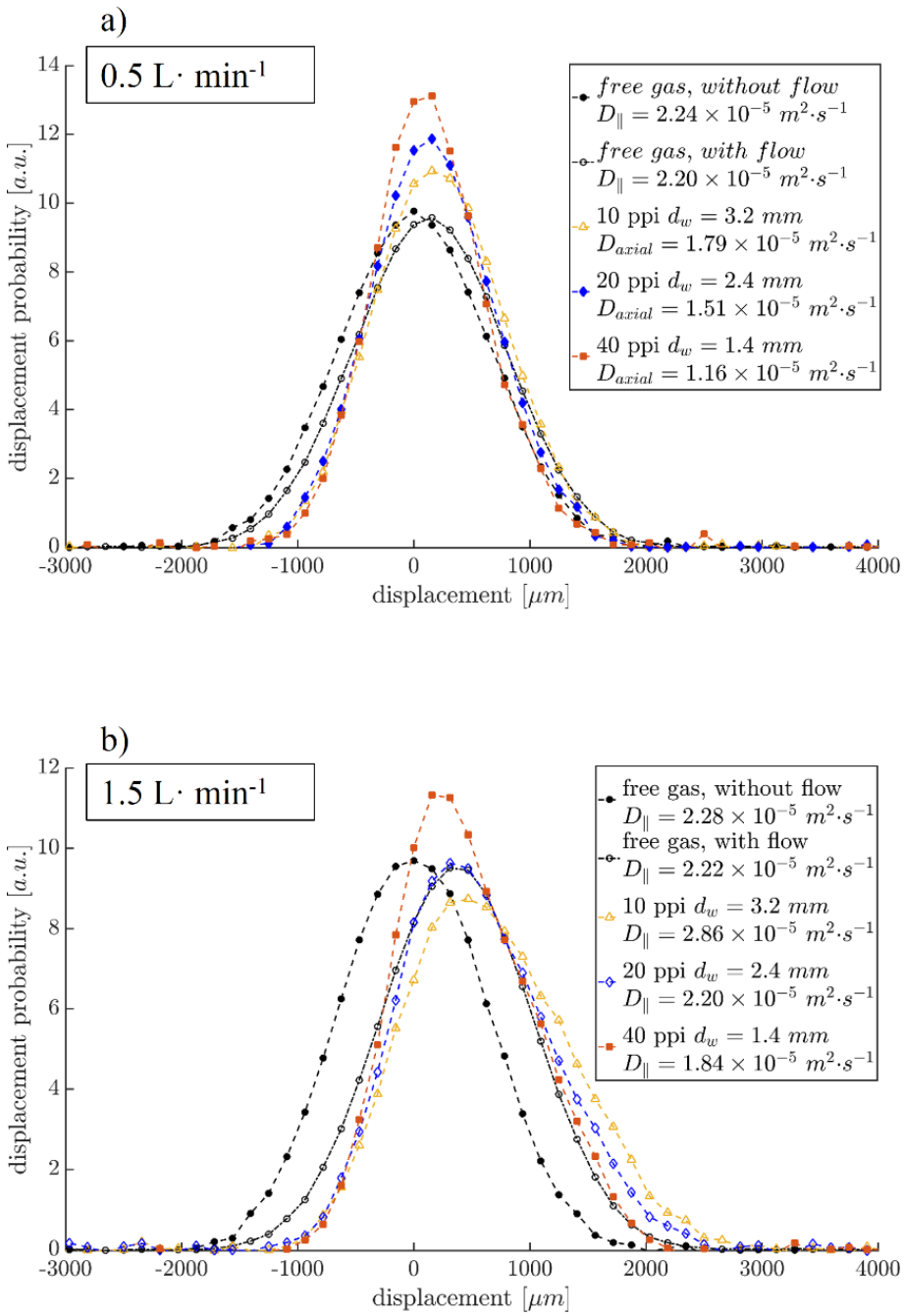

Figure 3.8. Gas propagator of methane measured in samples with different pore density at (a) 0.5 and (b) 1.5 L·min^{-1}. For comparison, the values for free gas measured without and with flow are given. Note that the different values for free gas in *a* and *b* reflect the experimental error.

3.4.2. Radial dispersion

In this section, gas propagators in the radial direction of the foams are presented and radial dispersion coefficients are calculated. Finally, the effect of VOI size and position on the radial dispersion coefficient is discussed.

The gas propagators measured at an observation time of 10 ms are depicted in Fig. S3 in the Appendix. The stagnant peaks at zero and symmetric shapes of the curves confirm that there is no net flow in the radial direction. However, the propagators slightly broaden with increasing flow rate, but maintain their Gaussian shape (R^2 > 0.98). Yet the degree of the hindrance of gas in the samples can be related to the pore window and strut diameter of the foams reported in Table 3.1. The propagators of 10, 20, and 40 ppi samples reach the baseline at about 2.0, 1.8, and 1.3 mm, respectively.

The obtained values for radial dispersion coefficients are given in Table 3.4. Additionally, Fig. S4 of the appendix shows a plot of $D_{\perp}$ versus the applied flow rates. Although the radial dispersion is less sensitive to the alteration of velocity as compared to axial dispersion, it increases (flow rate < 1.5 L·min^{-1}) when flow velocity increases (c.f., Table 3.4). The rise in dispersion coefficients can also be linked to the geometry of the foams in radial direction. In the majority of the measurements (0.1 L·min^{-1} < flow rate < 1.5 L·min^{-1}), the radial dispersion measured for the samples with bigger window size is larger than for foams with smaller window size ($D_{\perp(10\,ppi)} > D_{\perp(20\,ppi)} > D_{\perp(40\,ppi)}$). Although no mathematical correlation between Re and $D_{\perp}$ can be drawn, a lower bound for radial dispersion can be seen (c.f., Fig. S4). A stepwise increase in flow rate increases the radial dispersion. However, the increase in $D_{\perp}$ is not pronounced as compared to $D_{\parallel}$.

Table 3.4. Radial dispersion coefficient ($D_\perp \times 10^5$, in $m^2 \cdot s^{-1}$) obtained for three structures.

L·min^{-1}	**0.10**	**0.20**	**0.30**	**0.40**	**0.50**	**0.75**	**1.00**	**1.25**	**1.50**	**1.75**	**2.00**	**2.25**
10 ppi	1.46	1.38	1.43	1.48	1.43	1.46	1.66	1.61	1.63	1.39	1.53	1.42
20 ppi	1.35	1.36	1.39	1.45	1.36	1.34	1.38	1.39	1.40	1.43	1.43	1.49
40 ppi	1.33	1.31	1.25	1.34	1.37	1.36	1.37	1.40	1.37	1.43	1.49	1.54

3.5. Dependency on size and position of VOI

The conducted measurements determined the gas propagators at the central volume of the foams (VOI as shown in Fig. 3.2b). To show that the results are representative of the averaged behavior of gas in the foams, some experiments were performed with different size and position of the VOI. First, the position of the standard VOI (12×12×12 mm^3) was shifted by 20 mm in axial direction of the sample. Second, the size of the VOI was enlarged to 16×16×16 mm^3. For both cases, almost identical gas propagators were measured, indicating that the results with the standard VOI are representative of the foams and allow consistent dispersion analysis.

The evaluation of VOI size effects on the radial dispersion is crucial since it shows that the chosen VOI for the measurement is not affected by the reactor wall. Thus, an enlarged VOI (16×16×16 mm^3) was used to measure the gas propagators again and compare the results to those obtained on the standard VOI (12×12×12 mm^3). This comparison can be found in the Appendix (Fig. S5). Both propagators show a stagnant peak at zero in radial direction. Minor differences in the baseline of the propagators lead to minor increase of $D_\perp$. This increase in $D_\perp$ can be explained by small contributions of the bypass flow between wall and foams. The gas molecules near the wall may move with lower hindrance due to the open edges of the sample and the reactor wall. To illustrate the extent of wall effects on radial dispersion, a larger VOI, which covers the entire radius of foam in x- and y-axes was chosen. The displacement length of the gas ensemble increases more than for the VOI of 16×16×16 mm^3 showing a lower probability of zero displacement, indicating the effect of wall interactions and flow bypass in these measurements. These measurements confirm that the chosen standard

VOI is suitable for radial dispersion measurements in foams, not including the wall interactions.

3.6. Conclusion

An optimized PFG-STE NMR sequence was applied in order to determine mass transport properties of thermally polarized gas flowing through commercial foam structures. The localized pore-scale analysis was used to determine dispersion coefficients in the both axial and radial directions for different flow rates. The analysis allowed investigating the effect of foam geometry, such as pore density, porosity, and window size on the gas dispersion and the underlying dispersion mechanism.

For the investigated foams and used flow rates, it can be concluded that, unlike radial dispersion coefficients, axial dispersion coefficients increase exponentially with flow rate. In addition, it was shown that, at higher flow rates > 0.5 $L \cdot min^{-1}$, the axial apparent dispersion coefficients are larger than the effective diffusion coefficients of methane in the foam structures. Both axial and radial apparent dispersion coefficients increase with window size.

It was shown that the NMR-based measurement technique is a reliable method for a quantitative determination of dispersion measurements. Furthermore, the concept presented here now allows a pore-scale analysis of gas flow within ceramic foams. As another advantage of volume selective NMR displacement measurements, artifacts caused by wall interactions and flow bypass can be avoided by adjusting the VOI.

Acknowledgments

The project was supported by German Research Foundation (DFG) in the frame of Research Training Group GRK 1860 “Micro-, meso- and macro-porous nonmetallic Materials: Fundamentals and Applications” (MIMENIMA).

References

[1] P.D. Eggenschwiler, D.N. Tsinoglou, J. Seyfert, C. Bach, U. Vogt, M. Gorbar, Ceramic foam substrates for automotive catalyst applications: Fluid mechanic analysis, Exp. Fluids. 47 (2009) 209–222. https://doi.org/10.1007/s00348-009-0653-2.

[2] M.V. Twigg, J.T. Richardson, Theory and applications of ceramic foam catalysts, Trans IChemE. 80 (2002) 183–189. https://doi.org/https://doi.org/10.1205/026387602753501906.

[3] Y. Peng, J.T. Richardson, Properties of ceramic foam catalyst supports: one-dimensional and two-dimensional heat transfer correlations, Appl. Catal. A Gen. 266 (2004) 235–244. https://doi.org/10.1016/j.apcata.2004.02.012.

[4] S. Zuercher, K. Pabst, G. Schaub, Ceramic foams as structured catalyst inserts in gas-particle filters for gas reactions-Effect of backmixing, Appl. Catal. A Gen. 357 (2009) 85–92. https://doi.org/10.1016/j.apcata.2009.01.020.

[5] M. V. Twigg, J.T. Richardson, Fundamentals and applications of structured ceramic foam catalysts, Ind. Eng. Chem. Res. 46 (2007) 4166–4177. https://doi.org/10.1021/ie061122o.

[6] F. Lucci, A. Della Torre, G. Montenegro, P.D. Eggenschwiler, On the catalytic performance of open cell structures versus honeycombs, Chem. Eng. J. 264 (2015) 514–521. https://doi.org/10.1016/j.cej.2014.11.080.

[7] R.M. Heck, S. Gulati, R.J. Farrauto, The application of monoliths for gas phase catalytic reactions, Chem. Eng. J. 82 (2001) 149–156. https://doi.org/https://doi.org/10.1016/S1385-8947(00)00365-X.

[8] B. Kreitz, G.D. Wehinger, T. Turek, Dynamic simulation of the CO_2 methanation in a micro-structured fixed-bed reactor, Chem. Eng. Sci. 195 (2019) 541–552. https://doi.org/10.1016/j.ces.2018.09.053.

[9] L. Lebon, J. Leblond, J.P. Hulin, Experimental measurement of dispersion processes at short times using a pulsed field gradient NMR technique, Phys. Fluids. 9 (1997) 481–490. https://doi.org/10.1063/1.869208.

[10] J.M. Van Baten, J. Ellenberger, R. Krishna, Radial and axial dispersion of the

liquid phase within a KATAPAK-S(R) structure: Experiments vs. CFD simulations, Chem. Eng. Sci. 56 (2001) 813–821. https://doi.org/10.1016/S0009-2509(00)00293-1.

[11] J.S. Chen, J.T. Chen, C.W. Liu, C.P. Liang, C.W. Lin, Analytical solutions to two-dimensional advection-dispersion equation in cylindrical coordinates in finite domain subject to first- and third-type inlet boundary conditions, J. Hydrol. 405 (2011) 522–531. https://doi.org/10.1016/j.jhydrol.2011.06.002.

[12] P.M. Singer, J. Mitchell, E.J. Fordham, Characterizing dispersivity and stagnation in porous media using NMR flow propagators, J. Magn. Reson. 270 (2016) 98–107. https://doi.org/10.1016/j.jmr.2016.07.004.

[13] L. Kiewidt, J. Thöming, Multiscale modeling of monolithic sponges as catalyst carrier for the methanation of carbon dioxide, Chem. Eng. Sci. X. 2 (2019). https://doi.org/10.1016/j.cesx.2019.100016.

[14] L. Kiewidt, J. Thöming, Pareto-optimal design and assessment of monolithic sponges as catalyst carriers for exothermic reactions, Chem. Eng. J. (2019) 496–504. https://doi.org/10.1016/j.cej.2018.11.109.

[15] P. Benz, P. Hütter, A. Schlegel, Radiale Stoffdispersionskoeffizienten in durchströmten keramischen Schäumen, Wärme- Und Stoffübertragung. 29 (1993) 125–127. https://doi.org/10.1007/BF01560081.

[16] C.L. Hackert, J.L. Ellzey, O.A. Ezekoye, M.J. Hall, Transverse dispersion at high Peclet numbers in short porous media, Exp. Fluids. 21 (1996) 286–290. https://doi.org/10.1007/BF00190679.

[17] J.C.F. Pereira, I. Malico, T.C. Hayashi, J. Raposo, Experimental and numerical characterization of the transverse dispersion at the exit of a short ceramic foam inside a pipe, Int. J. Heat Mass Transf. 48 (2005) 1–14. https://doi.org/10.1016/j.ijheatmasstransfer.2004.08.001.

[18] M. Saber, C. Pham-Huu, D. Edouard, Axial dispersion based on the residence time distribution curves in a millireactor filled with β-sic foam catalyst, Ind. Eng. Chem. Res. 51 (2012) 15011–15017. https://doi.org/10.1021/ie3017829.

[19] P. Habisreuther, N. Djordjevic, N. Zarzalis, Statistical distribution of residence

time and tortuosity of flow through open-cell foams, Chem. Eng. Sci. 64 (2009) 4943–4954. https://doi.org/10.1016/j.ces.2009.07.033.

[20] C. Hutter, A. Zenklusen, S. Kuhn, P.R. von Rohr, Large eddy simulation of flow through a streamwise-periodic structure, Chem. Eng. Sci. 66 (2011) 519–529. https://doi.org/10.1016/j.ces.2010.11.015.

[21] R. Häfeli, C. Hutter, M. Damsohn, H.M. Prasser, P.R. von Rohr, Dispersion in fully developed flow through regular porous structures: Experiments with wire-mesh sensors, Chem. Eng. Process. Process Intensif. 69 (2013) 104–111. https://doi.org/10.1016/j.cep.2013.03.006.

[22] A.J. Onstad, C.J. Elkins, F. Medina, R.B. Wicker, J.K. Eaton, Full-field measurements of flow through a scaled metal foam replica, Exp. Fluids. 50 (2011) 1571–1585. https://doi.org/10.1007/s00348-010-1008-8.

[23] J.D. Seymour, P.T. Callaghan, Generalized approach to NMR analysis of flow and dispersion in porous media, AIChE J. 43 (1997) 2096–2111. https://doi.org/doi.org/10.1002/aic.690430817.

[24] O. Levenspiel, Chemical reaction engineering, John Wiley & Sons, 1998.

[25] C. Hutter, A. Zenklusen, R. Lang, P.R. von Rohr, Axial dispersion in metal foams and streamwise-periodic porous media, Chem. Eng. Sci. 66 (2011) 1132–1141. https://doi.org/10.1016/j.ces.2010.12.016.

[26] M. Ferrari, C. Moyne, D. Stemmelen, Study of dispersion in porous media by pulsed field gradient NMR: Influence of the fluid rheology, Transp. Porous Media. 123 (2018) 101–124. https://doi.org/10.1007/s11242-018-1027-0.

[27] F. Stallmach, J. Kärger, The potentials of pulsed field gradient NMR for investigation of porous media, Adsorption. 133 (1999) 117–133. https://doi.org/10.1023/A:1008949607093.

[28] A.T. Watson, C.T.P. Chang, Characterizing porous media with NMR methods, Prog. Nucl. Magn. Reson. Spectrosc. 31 (1997) 343–386. https://doi.org/10.1016/S0079-6565(97)00053-8.

[29] J.D. Seymour, P.T. Callaghan, “Flow-diffraction” structural characterization and measurement of hydrodynamic dispersion in porous media by PGSE NMR, J.

Magn. Reson. - Ser. A. 122 (1996) 90–93. https://doi.org/10.1006/jmra.1996.0182.

[30] S.L. Codd, S.A. Altobelli, A PGSE study of propane gas flow through model porous bead packs, J. Magn. Reson. 163 (2003) 16–22. https://doi.org/10.1016/S1090-7807(03)00111-3.

[31] M. Mirdrikvand, J. Ilsemann, W. Dreher, J. Thöming, Spatially resolved characterization of the gas propagator in monolithic structured catalysts using NMR diffusiometry, Chem. Eng. Technol. 41 (2018) 1871–1880. https://doi.org/10.1002/ceat.201800201.

[32] R. Kimmich, F. Winter, W. Nusser, K.H. Spohn, Interactions and fluctuations deduced from proton field-cycling relaxation spectroscopy of polypeptides, DNA, muscles, and algae, J. Magn. Reson. 68 (1986) 263–282. https://doi.org/10.1016/0022-2364(86)90243-X.

[33] I. Tkáč, Z. Starčuk, I.Y. Choi, R. Gruetter, In vivo ^{1}H NMR spectroscopy of rat brain at 1 ms echo time, Magn. Reson. Med. 41 (1999) 649–656. https://doi.org/10.1002/(SICI)1522-2594(199904)41:4<649::AID-MRM2>3.0.CO;2-G.

[34] D.G. Cory, A.N. Garroway, Measurement of translational displacement probabilities by NMR: An indicator of compartmentation, Magn. Reson. Med. 14 (1990) 435–444. https://doi.org/10.1002/mrm.1910140303.

[35] E.H.M.S.G. de Figueiredo, A.F.N.G. Borgonovi, T.M. Doring, Basic concepts of mr imaging, diffusion MR imaging, and diffusion tensor imaging, Magn. Reson. Imaging Clin. N. Am. (2011). https://doi.org/10.1016/j.mric.2010.10.005.

[36] P.T. Callaghan, D. MacGowan, K.J. Packer, F.O. Zelaya, High-resolution q-space imaging in porous structures, J. Magn. Reson. 90 (1990) 177–182. https://doi.org/10.1016/0022-2364(90)90376-K.

[37] J. Kärger, Transport phenomena in nanoporous materials, ChemPhysChem. 16 (2015) 24–51. https://doi.org/10.1002/cphc.201402340.

[38] A. Inayat, H. Freund, T. Zeiser, W. Schwieger, Determining the specific surface area of ceramic foams: The tetrakaidecahedra model revisited, Chem. Eng. Sci.

66 (2011) 1179–1188. https://doi.org/10.1016/j.ces.2010.12.031.

[39] D.B. Ingham, I. Pop, Transport Phenomena in Porous Media III, 1998. https://doi.org/10.1016/B978-0-08-044490-1.X5003-0.

[40] A. Della Torre, G. Montenegro, G.R. Tabor, M.L. Wears, CFD characterization of flow regimes inside open-cell foam substrates, Int. J. Heat Fluid Flow. 50 (2014) 72–82. https://doi.org/10.1016/j.ijheatfluidflow.2014.05.005.

[41] D. Seguin, A. Montillet, J. Comiti, F. Huet, Experimental characterization of flow regimes in various porous media-II: Transition to turbulent regime, Chem. Eng. Sci. 53 (1998) 3897–3909. https://doi.org/10.1016/S0009-2509(98)80003-1.

[42] C.J. Jamson, A.K. Jameson, N.C. Smith, J.K. Hwang, T. Zia, Carbon-13 and proton spin relaxation in methane gas, J. Phyiscal Chem. 95 (1991) 1092–1098.

[43] I. V. Koptyug, A.A. Lysova, A. V. Matveev, V.N. Parmon, R.Z. Sagdeev, NMR imaging of mass transport processes and catalytic reactions, Top. Catal. 32 (2005) 83–91. https://doi.org/10.1007/s11244-005-9256-1.

[44] A. Montillet, J. Comiti, J. Legrand, Axial dispersion in liquid flow through packed reticulated metallic foams and fixed beds of different structures, Chem. Eng. J. 52 (1993) 63–71. https://doi.org/10.1016/0300-9467(93)80050-X.

[45] D.R.F. Harleman, R.R. Rumer, Longitudinal and lateral dispersion in an isotropic porous medium, J. Fluid Mech. 16 (1963) 385–394. https://doi.org/10.1017/S0022112063000847.

[46] L. Kiewidt, Solid sponges as support for heterogeneous catalysts in gas-phase reactions, Doctoral dissertation, University of Bremen, 2017. https://d-nb.info/1150833947/34.

[47] C. D'Agostino, J. Mitchell, L.F. Gladden, M.D. Mantle, Hydrogen bonding network disruption in mesoporous catalyst supports probed by PFG-NMR diffusometry and NMR relaxometry, J. Phys. Chem. C. (2012). https://doi.org/10.1021/jp2123295.

[48] M. Niemeyer, Simulation der Strömungsverteilung in gleichfoermigen und gradierten Schwaemmen, Master Thesis, Univ. Bremen. (2016).

Appendix 1:

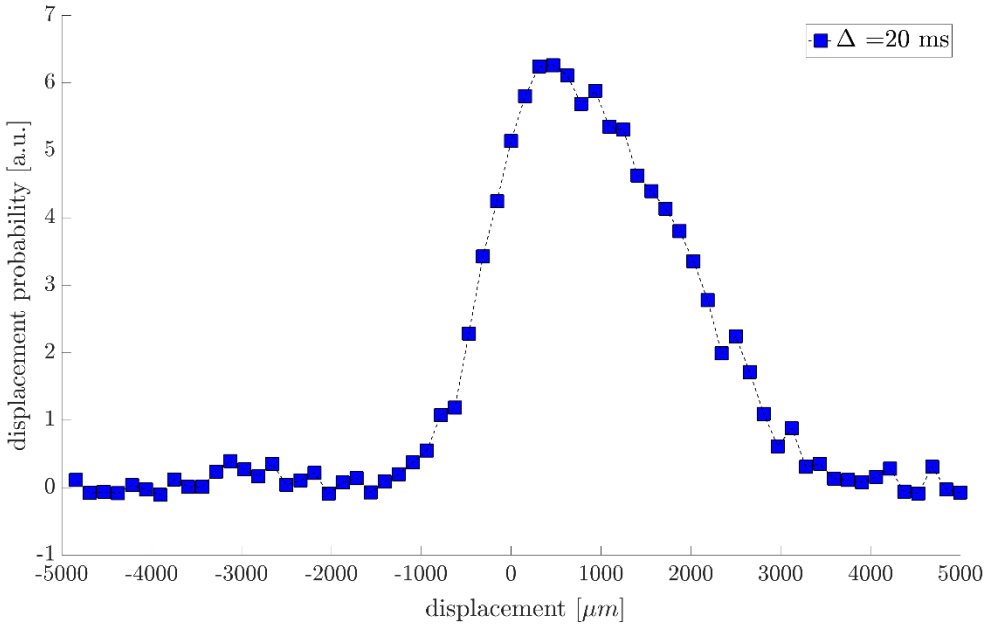

Figure S1. Gas propagator measured at an observation time of 20 ms and a flow rate of 1.5 L· min^{-1}.

Appendix 2:

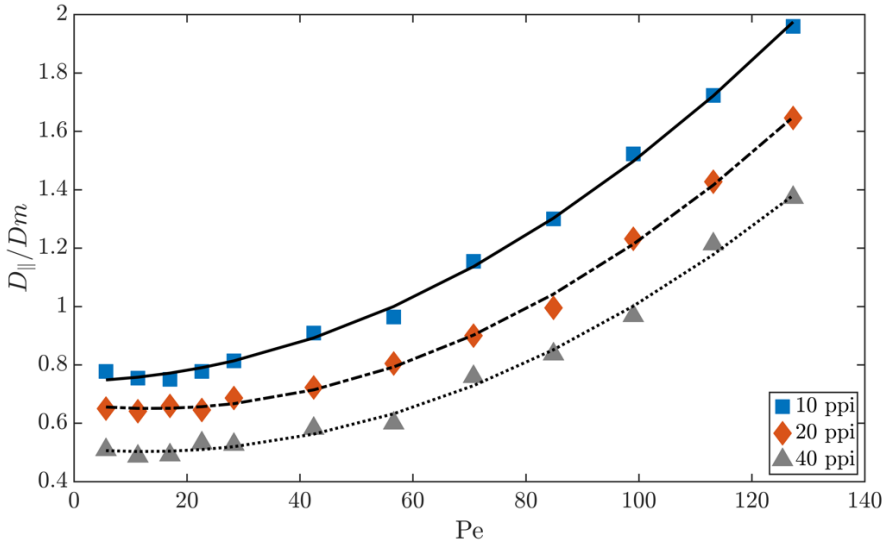

Figure S2. Normalized axial dispersion coefficient as a function of *Pe* number determined for the three foam types. The superimposed curves are polynomial fits to all data points.

Appendix 3:

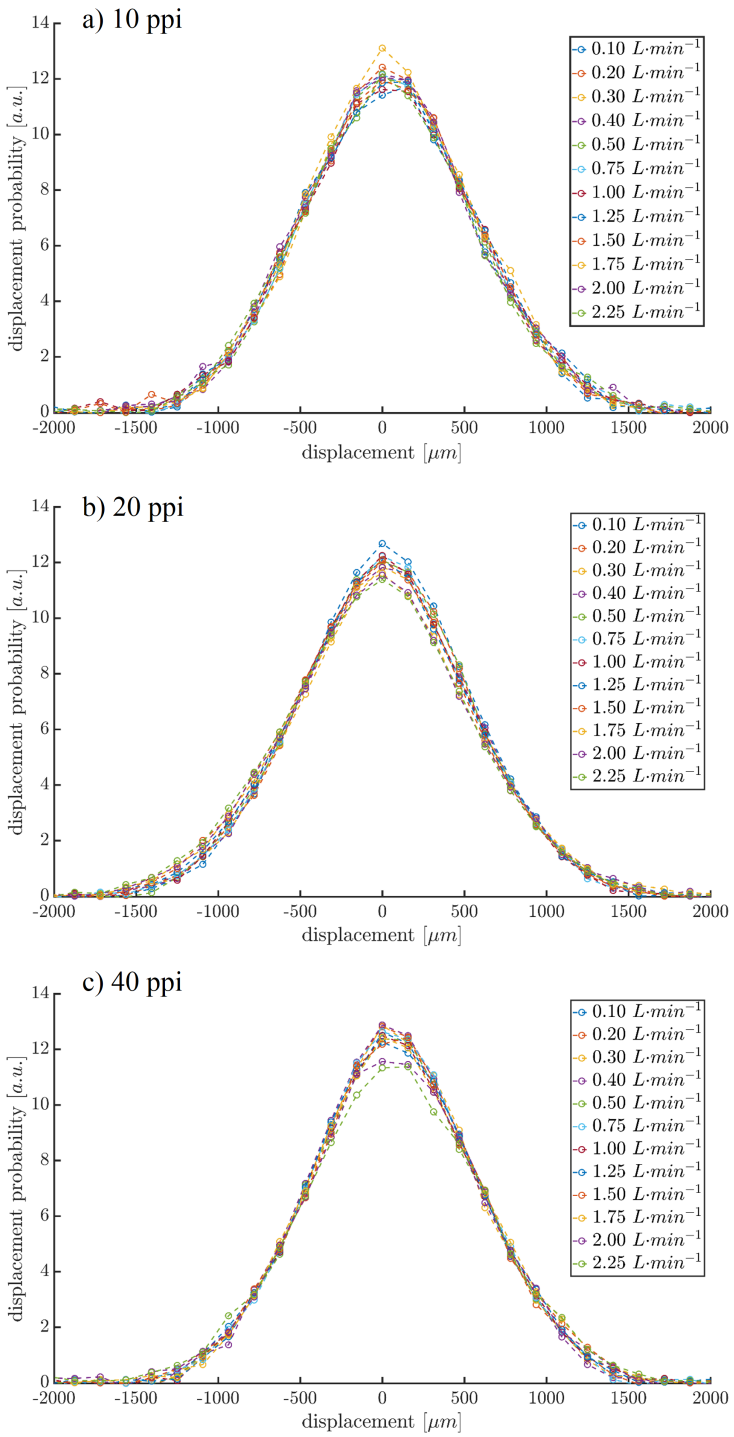

Figure S3. Displacement curves in radial direction at different flow rates for (a) 10 ppi, (b) 20 ppi, and (c) 40 ppi sample.

Appendix 4:

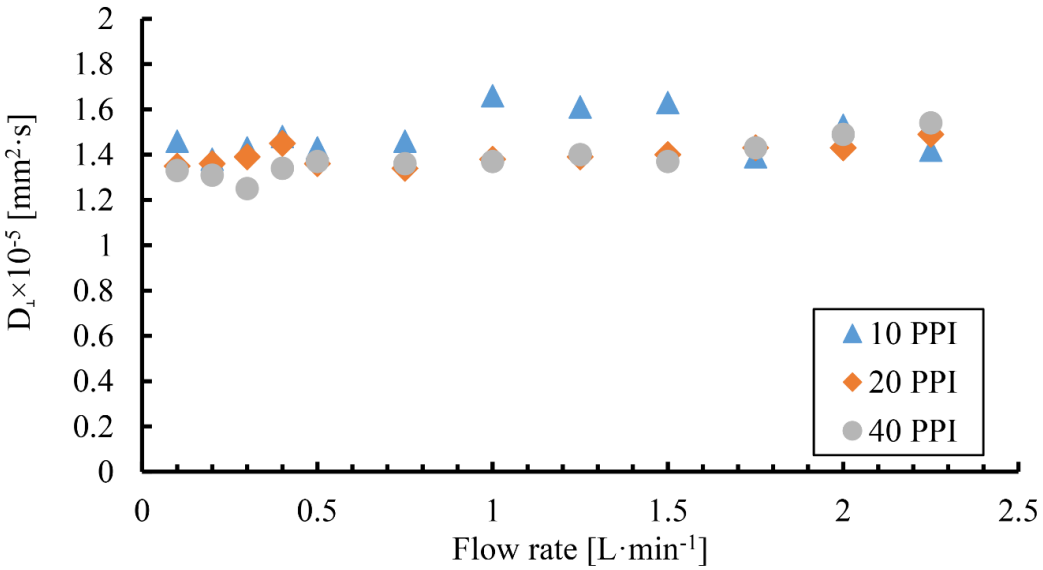

Figure S4. Dispersion coefficient in radial direction for all foam samples.

Appendix 5:

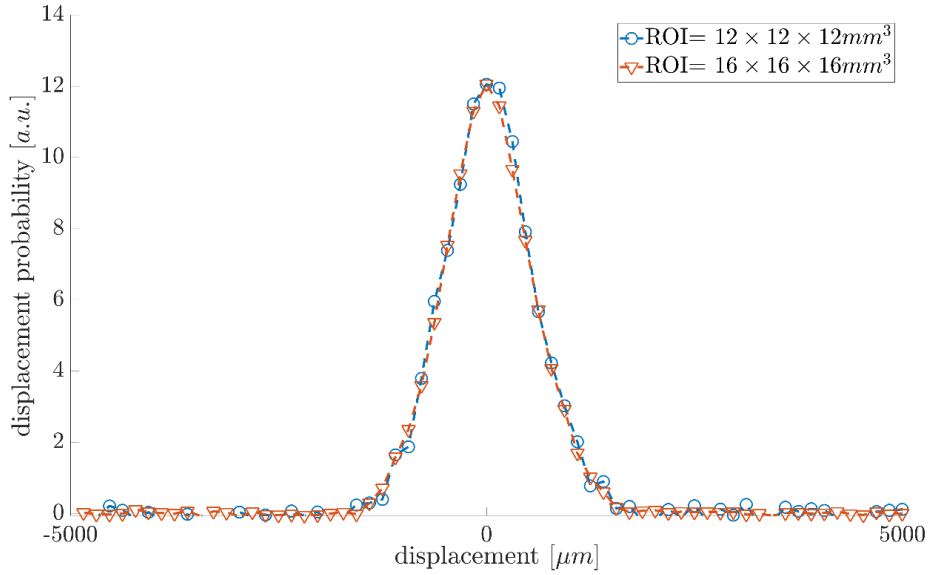

Figure S5. Effect of VOI size on radial dispersion.

Chapter 4

Flow*

Abstract: NMR velocimetry allows spatially resolved and non-invasive studies of mass transport in opaque monoliths. The velocity field of thermally polarized methane gas was measured in the regular and irregular monoliths using NMR velocimetry (MRV). Furthermore, gas velocity was investigated to characterize the gas flow in commercial 20 ppi open-cell foams, although not shown in the present chapter. The results of the MRV analysis were compared to computed microtomography-based Computational Fluid Dynamics (CFD) simulations for methane flow in identical monoliths. The study also gives a clear comparison between MRV and CFD velocity fields at the entrance, throughout, and exit regions of honeycomb catalyst carriers.

Keywords: flow measurement; gas; NMR; CFD; velocity; diffusion

* Sadeghi, M., **Mirdrikvand, M.**, Pesch, G., Dreher, W., Thöming, J. Full field analysis of gas flow within open-cell foams: comparison of microtomography-based CFD simulations and experimental MRV flow mapping data, *Experiments in Fluids* (*in press*)

* Sadeghi, M., Thöming, J., Dreher, W., **Mirdrikvand, M.**, MRV and CFD of Gas Flow Through Regular Monolithic Structures with Emphasis on Dispersion and Maldistribution (*in preparation*).

4.1. Introduction

There is growing interest in using regularly and irregularly structured monoliths as catalyst support or exhaust filters in chemical and automotive industries. The regular monoliths are often exposed to the high throughput of gas in case of exhaust filters or to moderate gas flow rates in case of catalyst supports in heterogeneously catalyzed reactions [1–4]. A majority of heterogeneously catalyzed reactions such as methanation or hydrogenation of alkenes occur in the gas phase and over monolithic catalysts such as open-cell foams and honeycomb structures. Thus, accurate analysis of the gas-solid phase helps to understand the mass transport mechanism of gases throughout the monolithic supports in gaseous reactions. The accurate analysis of mass transport also helps to reassess the theoretical assumptions that generally describe the structured monoliths as an ideal network of square channels. Gulijk et al. [5] illustrated that mass transport of gas is severely affected by minor geometrical alteration of monolith channels. For instance, the channel wall thickness, cracks, skewed, and defected walls cause deviation from an ideal distribution of gas in a honeycomb monolith.

The potential capability of Nuclear Magnetic Resonance (NMR) for the investigation of mass transport of gas in opaque systems has turned NMR into a powerful technique in engineering communities [6–10]. The reason for this interest is the possibility of non-invasive analysis of the gas hydrodynamics, i.e., velocity and diffusion, or even temperature and concentration for an operating system under the same experimental conditions. Newling [11] reviewed the efforts taken to measure gas flow by Magnetic Resonance Velocimetry (MRV). Since then, excellent studies have been published on mass transport of gas, particularly for monolithic structures [12–15]. Magnetic Resonance Imaging (MRI) of thermally polarized gases has always been a challenging issue because of the low Signal-to-Noise ratio (SNR) caused by low density, fast diffusivity, and short NMR relaxation times [6]. As solutions, hyperpolarization techniques [10] or the usage of SF_6 as an alternative and NMR friendly gas has been considered to perform a similar but not identical conditions in exhaust filters. SF_6 is favorable due to its high MRI signal compared to other thermally polarized gases [10,16–18]. For instance, Ramskill et al. [17] have used SF_6 to investigate velocity fields

in exhaust filters. More recently, Cooper et. al. succeeded in obtaining images of velocity fields and turbulent diffusivity of SF_6 gas in wall-flow channels by applying compressed sensing imaging [19]. However, the vital aspect of measuring thermally polarized gases is the possibility of investigating directly technically relevant gases, such as methane gas for methanation reaction. Thus, realistic information on diffusivity and flow of the gas in monoliths can be obtained. Despite the difficulties in MRI of thermally polarized gases, there is still free room to improve SNR obtained in MRI of gases. Recently, a straightforward technique for full field analysis of thermally polarized gases in porous media was proposed [20]. The method uses a trade-off between excitation angle, echo time (TE), and repetition time (TR) in order to improve SNR of MRI images. In the present study, the flow of thermally polarized methane gas is measured using this optimized MRV method. Eventually, the full field MRV was compared to CFD results performed for the identical monoliths. The CFD and MRV velocity fields are compared in three regions to highlight the key differences and coordination of both methods. The current measurements can answer the question regarding the mal-distribution of gases in regular monoliths. The results of this work can be immediately used to improve numerical predictions for gas-solid systems as a detailed comparison of MRV and CFD data for identical gas and monoliths reveals useful information on gas distribution affected by monoliths.

4.2. Theory and method

4.2.1.1. MRV sequence

3D MRI of the gas was conducted using a spin-echo based phase contrast MRV sequence. A scheme of the implemented pulse sequence is given in Fig. 4.1. Two phase encoding gradients were applied in transversal direction (x, y) accompanied by a read gradient in the axial direction (z) to obtain the 3D spatial resolution. Three steps were taken to optimize velocity measurements of methane gas in the porous structure, including TR and excitation flip angle adjustment, choice of TE based on transversal relaxation time (T_2) and diffusion coefficient D, and finally implementation of RF phase cycling. Accordingly, the excitation angle was chosen based on the Ernst angle to

increase the SNR [20]. A pair of unipolar velocity encoding gradients were applied prior and after the refocusing pulse to determine velocity vectors in the Regions of Interest (ROI)s. The velocity encoding gradients also act as crusher gradients to suppress unwanted coherence pathways. The velocity encoding gradients were applied in four steps according to the Hadamard approach [21,22]. Using a flip angle of 127°, TE of 3.15 ms, and TR of 50 ms, the total measurement time for measurement was about three hours. Field of View (FOV) was set to 96 × 64 × 64 mm^3 in a matrix 120 × 80 × 80 giving a resolution of 0.8 × 0.8 × 0.8 mm^3. A velocity encoding range [-VENC, +VENC] with $VENC$ = 300 $mm \cdot s^{-1}$ was used according to the expected maximal velocity for flow rates of 1.5 $L \cdot min^{-1}$. Flow encoding duration and flow encoding delay were δ = 0.37 ms and Δ = 1.69 ms, respectively. The measurements were averaged 8 or 16 times for each flow rate to improve SNR.

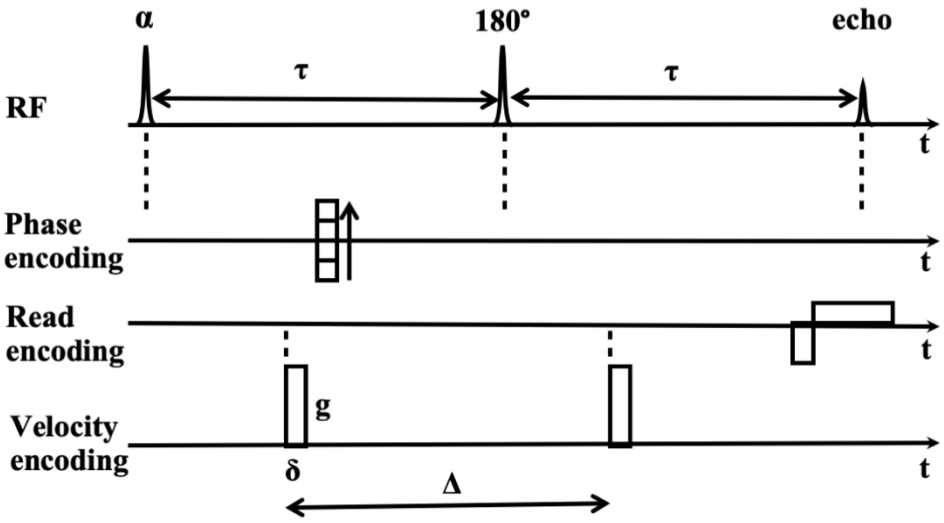

Figure 4.1. Implemented single-SE PC MRV pulse sequence for 3D MRV of methane in the monoliths (not to scale). For slice-selective 2D imaging, soft RF pulses with slice-selection and slice-rephasing gradients in the slice direction are used instead of rectangular RF pulses, and phase encoding is only performed in one direction.

4.2.1.2. Error estimation in MRV measurements

MRV precision was referred to as the standard deviation (STD) of velocities in the region of honeycomb. Theoretically, it could be estimated by an ideal model given by Pelc et al.[22]:

$$\sigma(v) = \frac{2\,VENC}{\pi \cdot SNR} \tag{4.1}$$

In the present study, an appropriate SNR (~14) with high reproducibility was obtained. According to Eq. 4.1 and with opted VENC = 300 mm·s^{-1}, such SNR resulted in a nominal σ of about 14 mm·s^{-1}. The Velocity-to-Noise Ratio (VNR) was nominally determined as π·SNR/2 ~23 and was estimated as the ratio of average velocity ($\bar{V}_{\mathrm{measured}}$ =100 mm·s^{-1}) and its STD in the central pixel of arbitrarily chosen honeycomb channels (5.5 mm·s^{-1}) in the MRV measurements: ($\bar{V}_{\mathrm{measured}}/\sigma_{measured}$) ~18. To analyze the reproducibility of the MRV as well as the SNR and VNR, absolute differences between three repetitive scans were computed.

Thus, the mean velocities in x- and y- directions in both honeycomb channels and sidewall regions that are substantially under such threshold were regarded as negligible, i.e., no net transversal flow was found in both regions. However, the mean velocity in z-direction in the sidewall region was non-negligible compared to such threshold, implying possible bypass in this region.

4.2.1.3. CFD model

CFD simulations were carried out by Mehrdad Sadeghi from the Chemical Process Engineering Department at the Center for Environmental Research and Sustainable Technology, Faculty 04 (Production Engineering), University of Bremen, to determine velocity fields within the utilized structures. For this purpose, the finite volume-based commercial CFD software OpenFOAM was chosen to simulate the incompressible flow of methane (since Mach number is less than 0.2) in the laminar flow regime. Reynolds number Re of the flow based on vessel diameter was computed ($Re = ud/n$ = 74.5), where u is the average bulk velocity, d stands for the diameter of the vessel, and ν is the

dynamic viscosity of methane. Such a Re number confirms that no turbulence or formation of eddies can occur, neither at entrance nor at terminal regions of the sample [4,23]. Monoliths with different morphologies were studied, a 3D-printed honeycomb, commercial honeycombs, and open-cell foams with 20 ppi pore density. The commercial structures were scanned by μ-CT imaging, and CFD simulations were run on the reconstructed structure. The 3D-printed honeycomb with the channel size and wall thickness of 2.4 mm and 0.8 mm was firstly designed in CAD software and then printed from PLA. For generating the computational network, CfMesh software was used, and the mesh with 17.2 and 4.7 million cells was chosen for commercial and printed structure, respectively.

4.3. Experimental setup

A glass made vessel (ID: 25 mm, length: 80 cm) was used for the gas flow measurements. The 3D-printed honeycomb had the following properties: made of Polylactic acid PLA with an inner channel size of 2.4 mm, a diameter of 25 mm, and a length of 40 mm. The honeycomb and foam samples were measured separately. The samples were put tightly in the cylindrical glass vessel to prevent bypass flow. Methane flow was supplied into the cylindrical vessel through a mass flow controller (FMA-2618-A, Omega Engineering, Norwalk, CT, USA). Finally, the experimental setup illustrated in Fig. 4.2 was inserted into the 7T Bruker superconducting magnet. The horizontal 7-Tesla scanner (BioSpec 70/20 USR, Bruker BioSpin MRI, Ettlingen, Germany) was equipped with a 114 mm inner bore gradient system (B-GA 12S2) enabling a maximum gradient strength of 440 $mT \cdot m^{-1}$ in each direction (x, y, z). All measurements were performed at ambient temperature and a pressure of 1.5 bar. Various volumetric flow rates were applied (0.5, 1.0, 1.5, and 2.0 $L \cdot min^{-1}$) for PFG-STE experiments, and a constant flow rate of 1.5 $L \cdot min^{-1}$ was applied for the MRV measurements.

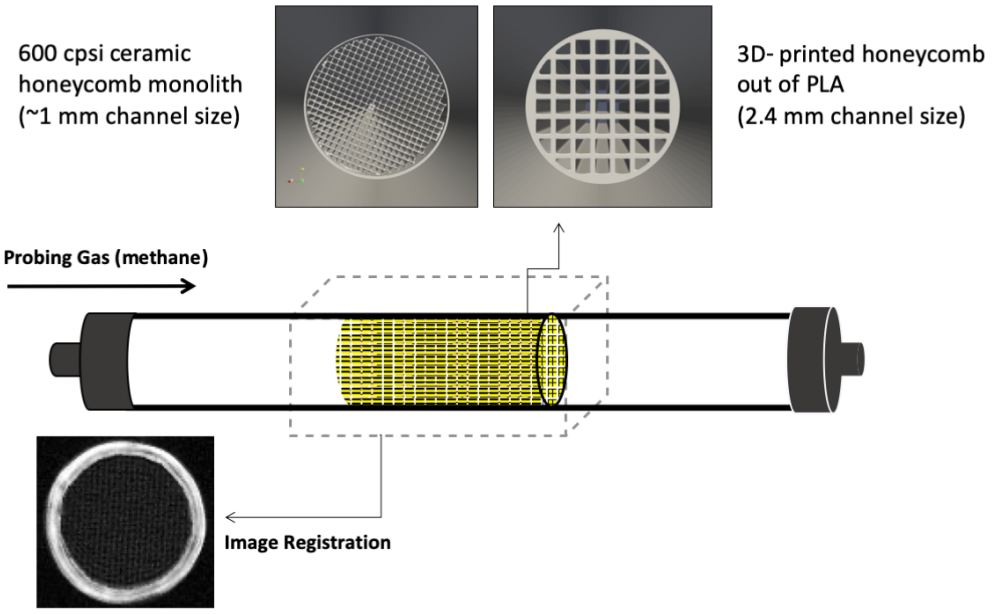

Figure 4.2. The experimental setup used for gas flow measurements.

4.4. Result and discussion

The results are described in two main sections. A channel-wise comparison of the MRV measurements and CFD simulations is given for the 3D-printed honeycomb in section 4.4.1. Afterward, velocity fields are compared at two main regions, upstream and downstream flow for the same structures. We skip the obtained results for commercial open-cell foams since they have been presented in a manuscript published in the journal of *Experiments in Fluids.* The author of this thesis is the second contributor to this manuscript.

4.4.1 Comparison of velocity field in the 3D-printed honeycomb monolith

Full field comparison of the MRV and CFD data is given here, unlike in some previous studies that compared the NMR results with available predictions reported in literature data [17,19]. MRV results for the 3D-printed monoliths are illustrated in Fig. 4.3. In general, the average velocity computed using CFD for the whole cross-section of the ceramic monolith in both methods is in good agreement with their MRV counterparts.

However, a general difference in mean velocity can be seen. The difference can be elucidated by comparison of the flow velocity between walls, which evidences a slight mismatch between simulation and experiments. The mismatch can be explained by two points. Firstly, there might be a bypass flow initiated from a non-ideal insertion of the sample to minimize the voids between the wall and the monolith. Secondly, diffusion related displacement of gas molecules is not included in the numerical solution, unlike the obtained results in NMR displacement measurements that support the comparison of both data.

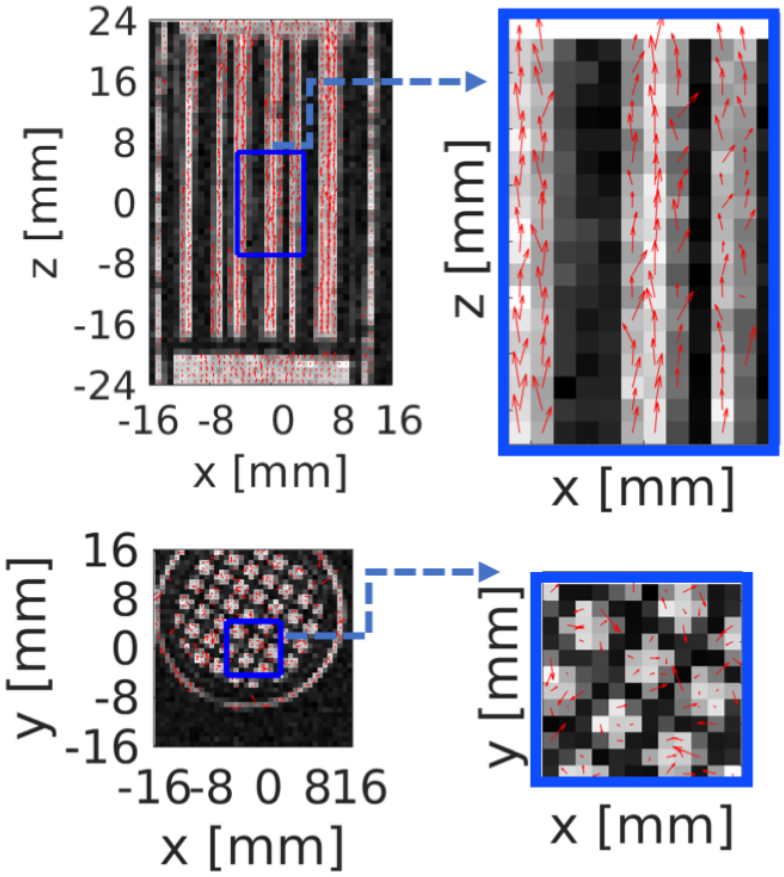

Figure 4.3. The velocity fields obtained from MRV data for 3D-printed monolith in axial (top) and radial (bottom) directions. The magnified regions are added to show magnitude of velocity in transversal and axial directions.

As expected, in the majority of cases, the velocity vectors lay in positive and straight, i.e., axial direction. The vectors obtained in CFD data are entirely straight and no drift or wave or zigzag motion can be observed in the channels (c.f., Fig. 4.4a). The reason for the smooth flow in the simulation can be related to the median filter applied for the reconstruction of μ-CT images which can ease the generation of the computational network. The filter smoothed the surface roughness and resulted in a ideal geometry at the wall channels. In contrast, the deviations from an ideal velocity distribution in axial direction highlight the gas-solid interaction within the monolith channels in MRV data. These interactions can be seen better in the 3D-printed channels.

The 3D-printed monolith was used to compare results within the channels as well as inlet and outlet regions. According to the resolution achieved in the MRI and the channel size (2.4 mm, wall thickness 0.8 mm) of the 3D-printed honeycomb monolith, each channel is characterized by nine pixels in MRV, allowing a more efficient comparison of experimental data and simulations. Note that the CFD simulations were performed for an ideal honeycomb structure without μ-CT data (see Fig. 4.2). Therefore, the results of the simulations can be considered as theoretical predictions for the flow field. For a detailed comparison of the experimental and numerical results, two main ROIs were considered (c.f., Fig. 4.4a). The velocity distribution in the ROI(1), i.e., the central area of a cross-section of honeycomb monolith with a diameter of 10 mm, including nine channels is shown in Fig. 4.5a. In the majority of points, the axial component (z) of velocity of CFD and MRV data are in very good agreement. Although the mean computed velocity in the axial direction of channels perfectly matches the CFD results, it may not fully describe the effect of a single channel on the velocity field. Thus, ROI(2) was chosen to compare the velocities in a single channel as a representative volume of the 3D-printed honeycomb. The velocity fields of both methods were compared in several arbitrarily chosen channels. Figure 4.5 shows one example of this comparison. In contrary to CFD data, which gives an ideal velocity in the axial direction, the vectors in MRV data seem to be more affected by the channel walls even in the central parts of the channels. A higher mean velocity was obtained in MRV and CFD results in ROI(2) as compared to ROI(1) (c.f., Fig.4.5ab). This difference can be regarded to the effect of

monolith walls in ROI(1) hindering the gas in the axial direction and resulting in lower mean velocities. The deviation between CFD and MRV can also be partially explained by the noise in the NMR data.

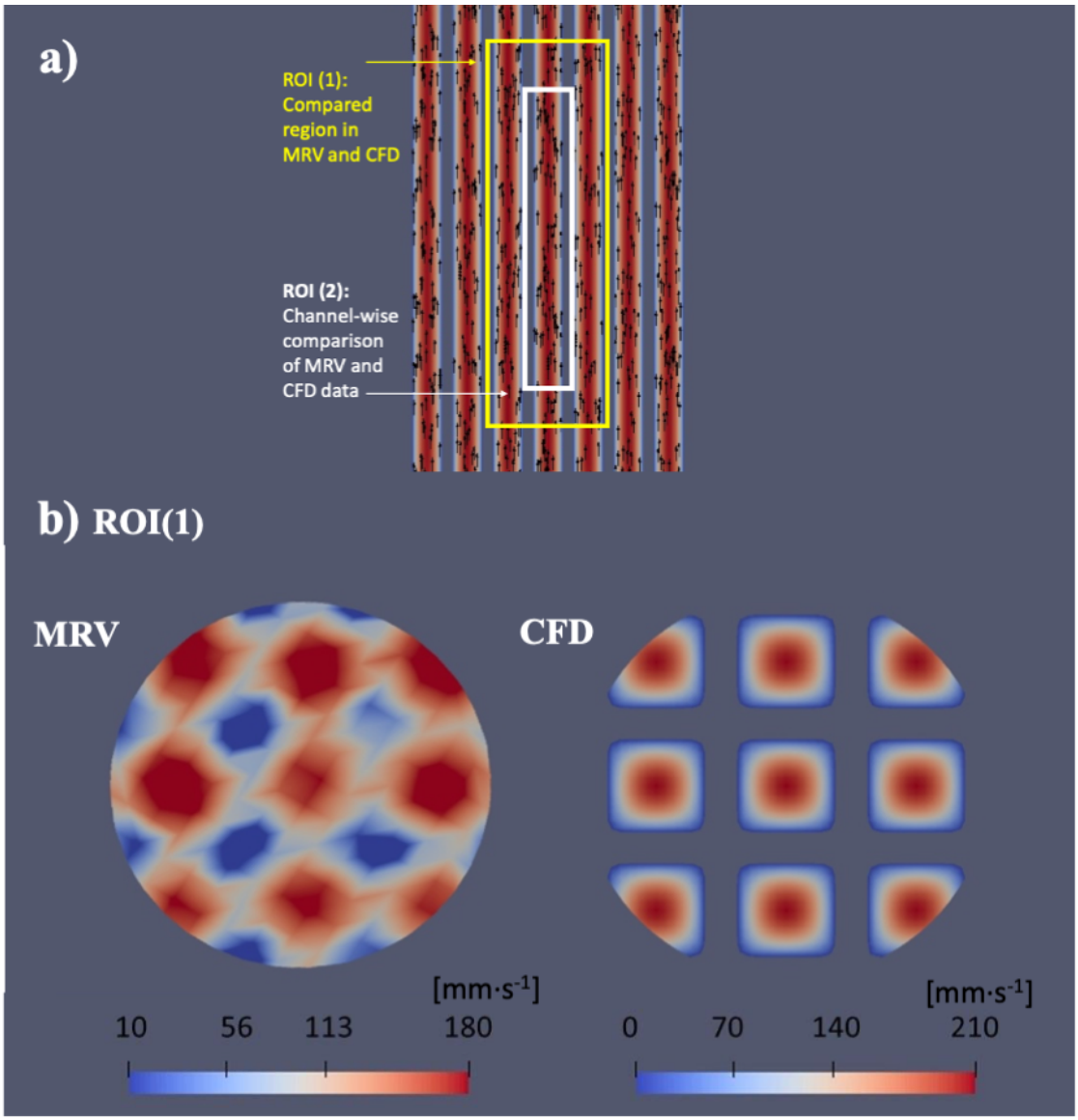

Figure 4.4. (a) The chosen ROIs selected to compare NMR and CFD data. (b) *z*-component of velocity in a central slice (ROI(1)) in experimental and numerical data. The depicted ROI for MRV data is tilted.

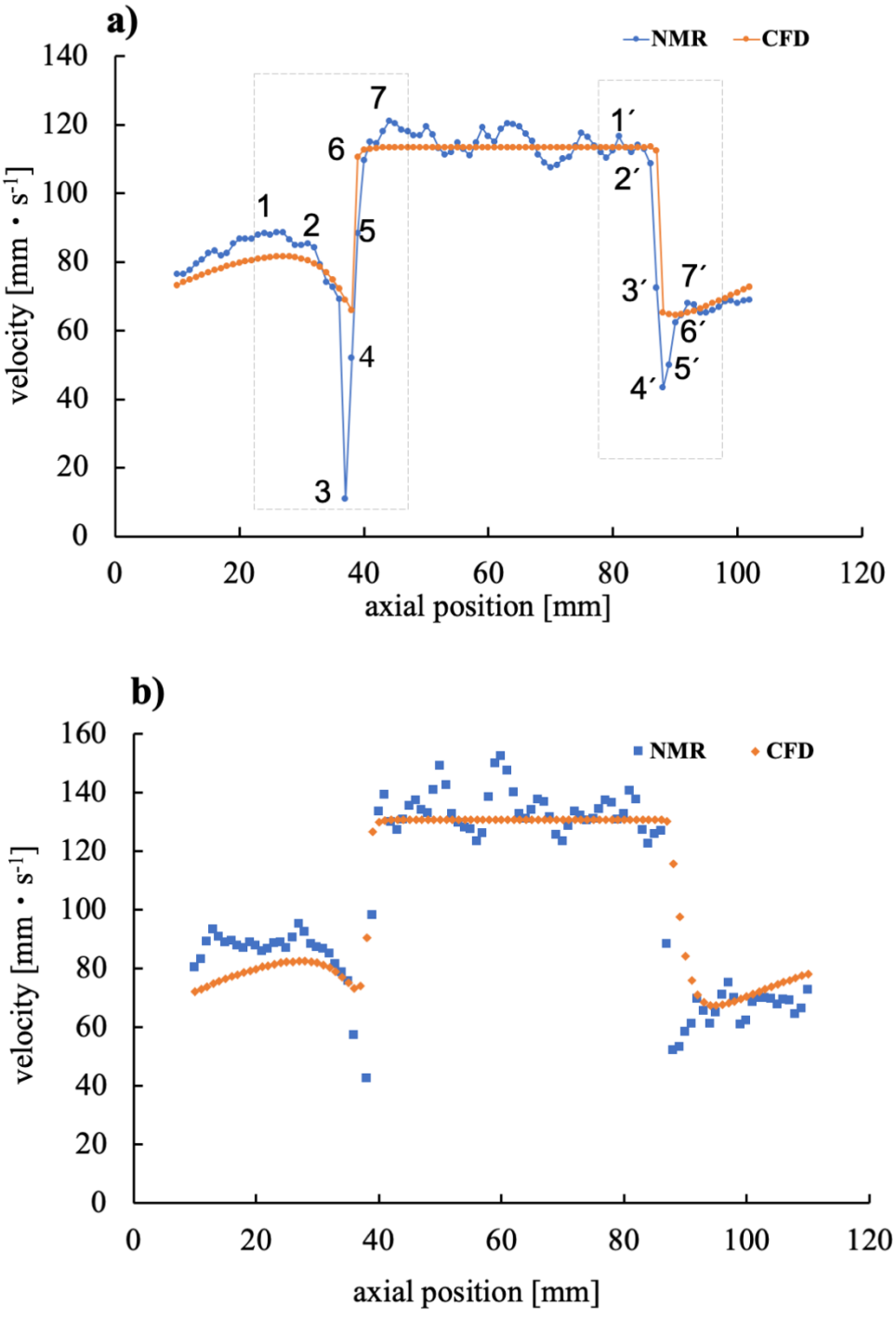

Figure 4.5. Comparison of the axial velocity component obtained by CFD and MRV (a) ROI(1) and (b) ROI(2). The axial position on the x-axis covers the entrance, inside, and exit region of the 3D-printed structure.

4.4.2. Upstream flow and downstream flow

The major pressure loss in honeycomb monoliths is expected to occur at the entrance and exit regions due to the contraction and expansion of flows [5]. In the present study, the pressure drop was computed through the CFD simulation within a channel in the flow direction. Due to the regularity of the structure, a linear pressure drop (shown in Fig. S2) of $\Delta P = 0.37$ Pa was calculated.

The upstream field was investigated, as shown in Fig. 4.6, to specifically focus on the entrance region, where the gas enters the honeycomb structure. The given numbers 1 to 7 in Fig. 4.6 correspond to the numbers in Fig. 4.5a showing methane at the entrance region. A detailed comparison of MRV and CFD results shows a good agreement in the velocity trends. As the bulk flow (1) approaches the monolith, the mean axial velocity component gradually decreases (1-2) until it reaches point (3) where the velocity sharply drops and the flow field experiences 'contraction'. The velocity bottoms out in slice (3) and increases again in slices (4-6) as the flow enters the honeycomb channels. The same trend for flow can be observed for a single channel of the honeycomb monolith as well. The mean axial velocity reaches a local maximum (7) compared to the entrance region as a result of honeycomb channels. Then the flow levels off and continues throughout the structure, maintaining a constant velocity.

A corresponding behavior is observed at the exit region of the monolith, as depicted in Fig. 4.7 with numbers 1′to 7′. The flow encounters a drop during (2′-4′) and partially recovers the loss in axial velocity (5′-7′).

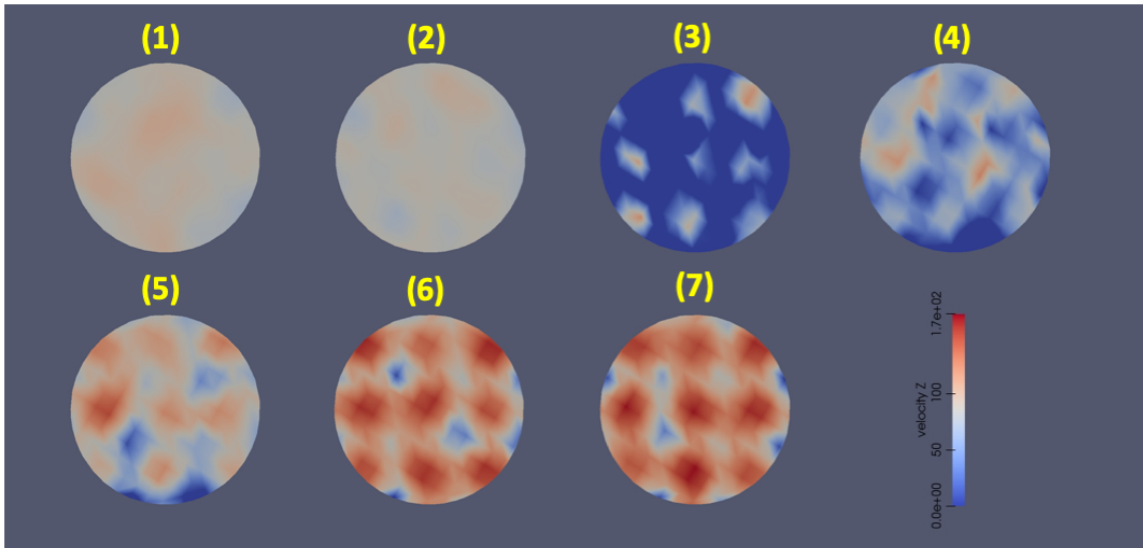

Figure 4.6. Axial velocity distribution at the entrance region along the honeycomb monolith determined by MRV.

The flow pattern can be shown by the local velocity vectors for both experimental and numerical data. The contraction in the gas velocity vectors can clearly be shown in NMR data as the overall axial velocity is very low as compared to the bulk velocity and the flow velocity in the honeycomb channels. The color map of the velocity in cross-sectional slices of MRV data in Fig. 4.6 and Fig. 4.7 also illustrates this fact. There is a deviation between CFD and MRV data at the entrance of the 3D-printed sample, especially at points (3-4) in Fig. 4.5a. The drop in the axial component of the velocity at the entrance region is more pronounced in MRV as compared to CFD data. Detailed investigation of the velocities at point 3 (Fig. S1 and Fig. 4.6) confirms the sudden drop in the velocity profile at a central channel of the monolith in MRV measurements (c.f., the brown line in Fig. S1). The figure illustrates the axial component of the velocity along lines 1 to 4 in Fig. 4.6. The NMR data elaborate on the effect of channels at the exit region as well (c.f., Fig. 4.7). The velocity profile of gas after the monolith shows flow expansion at the outlet over a longer distance compared to the entrance. Therefore, in both MRV and CFD data, it was observed that the flow does not develop its axial component again soon enough as the occurrence of jet after flow leaves the structure [19]. The flow velocities in slices 3′ to 7′ (Fig. 4.7) show an uneven distribution of axial

velocity even at 3.2 mm after leaving the velocity keeping the direction of flow as in channels. This effect can be observed even after eight millimeters after the honeycomb by analyzing the cross-sections in CFD data.

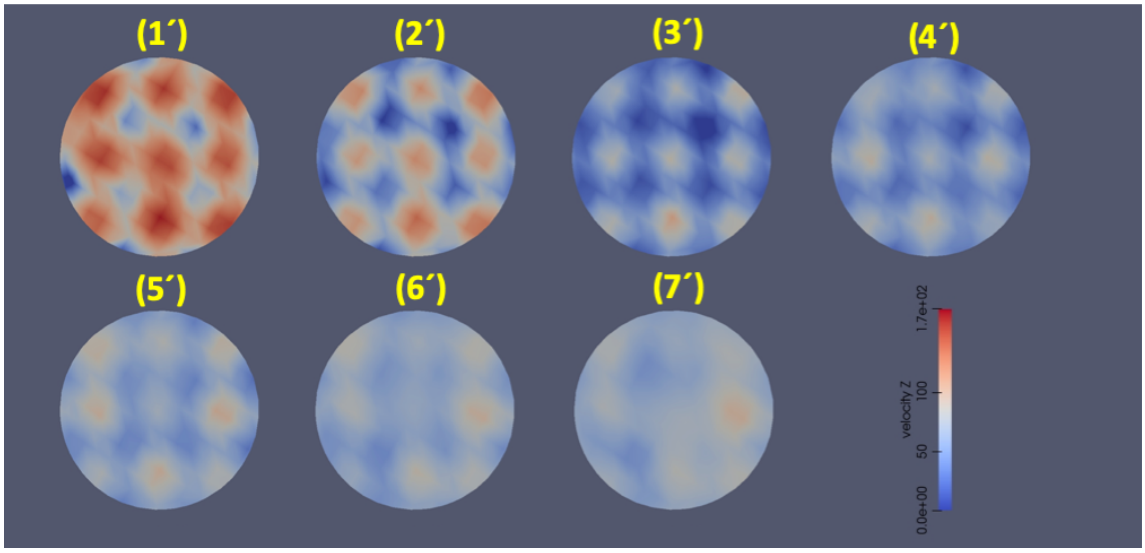

Figure 4.7. Axial velocity distribution at the exit region along the honeycomb monolith determined by MRV.

4.5. Conclusion

In summary, we have used an optimized phase-contrast MRI, which allowed a spatially resolved study of mass transport of methane gas through regular honeycomb monoliths. The measurements clearly showed the flow field through the monolith. A channel-wise analysis of flow velocity was also carried out by comparing MRV and CFD results. The comparison of the MRV results with CFD simulations suggests the cause of maldistribution in monoliths. MRV data can validate or even improve predictions made by CFD models, while it gives an insight into the gas hydrodynamics in the monoliths. The comparison of gas displacement profiles as well as MRV results emphasizes the importance of considering diffusional transport in such systems for a more accurate prediction of gas behavior in gas-solid reactive systems at the entrance and exit region.

Acknowledgments

The project was supported by the German Research Foundation (DFG) in the frame of Research Training Group GRK 1860 “Micro-, meso- and macro-porous nonmetallic Materials: Fundamentals and Applications” (MIMENIMA). We are grateful to Dipl.-Ing. Thomas Ilzig from the Department of Mechatronic Engineering (Tomography division) at the Technical University of Dresden for performing micro-tomography analyses of honeycomb monoliths used in the experiments. In addition, we would like to appreciate the support of Philip Kemper for providing us with 3D-printed honeycomb samples.

References

[1] P.D. Eggenschwiler, D.N. Tsinoglou, J. Seyfert, C. Bach, U. Vogt, M. Gorbar, Ceramic foam substrates for automotive catalyst applications: Fluid mechanic analysis, Exp. Fluids. 47 (2009) 209–222. https://doi.org/10.1007/s00348-009-0653-2.

[2] F. Donsì, S. Cimino, A. Di Benedetto, R. Pirone, G. Russo, The effect of support morphology on the reaction of oxidative dehydrogenation of ethane to ethylene at short contact times, Catal. Today. 105 (2005) 551–559. https://doi.org/10.1016/j.cattod.2005.06.016.

[3] B. Neumann, T.W. Elkins, W. Dreher, H. Hagelin-Weaver, J.C. Nino, M. Bäumer, Enhanced catalytic methane coupling using novel ceramic foams with bimodal porosity, Catal. Sci. Technol. 3 (2013) 89–93. https://doi.org/10.1039/C2CY20458D.

[4] F. Lucci, A. Della Torre, G. Montenegro, P.D. Eggenschwiler, On the catalytic performance of open cell structures versus honeycombs, Chem. Eng. J. 264 (2015) 514–521. https://doi.org/10.1016/j.cej.2014.11.080.

[5] C. Van Gulijk, M.J.G. Linders, T. Valdés-Solís, F. Kapteijn, Intrinsic channel maldistribution in monolithic catalyst support structures, Chem. Eng. J. 109 (2005) 89–96. https://doi.org/10.1016/j.cej.2005.03.013.

[6] B. Newling, ‘“Gas flow measurements by NMR,”’ 52 (2008) 31–48. https://doi.org/10.1016/j.pnmrs.2007.08.002.

[7] S.I. Han, K.L. Pierce, A. Pines, NMR velocity mapping of gas flow around solid objects, Phys. Rev. E - Stat. Nonlinear, Soft Matter Phys. 74 (2006) 016302. https://doi.org/10.1103/PhysRevE.74.016302.

[8] E. Harel, J. Granwehr, J.A. Seeley, A. Pines, Multiphase imaging of gas flow in a nanoporous material using remote-detection NMR, Nat. Mater. 5 (2006) 321–327. https://doi.org/10.1038/nmat1598.

[9] M. Mirdrikvand, J. Ilsemann, W. Dreher, J. Thöming, Spatially resolved characterization of the gas propagator in monolithic structured catalysts using NMR diffusiometry, Chem. Eng. Technol. 41 (2018) 1871–1880.

https://doi.org/10.1002/ceat.201800201.

[10] K. V. Kovtunov, D. Lebedev, A. Svyatova, E. V. Pokochueva, I.P. Prosvirin, E.Y. Gerasimov, V.I. Bukhtiyarov, C.R. Müller, A. Fedorov, I. V. Koptyug, Robust In Situ Magnetic Resonance Imaging of Heterogeneous Catalytic Hydrogenation with and without Hyperpolarization, ChemCatChem. 11 (2019) 969–973. https://doi.org/10.1002/cctc.201801820.

[11] B. Newling, Gas flow measurements by NMR, Prog. Nucl. Magn. Reson. Spectrosc. 52 (2008) 31–48. https://doi.org/10.1016/j.pnmrs.2007.08.002.

[12] L.-S. Bouchard, S.R. Burt, M.S. Anwar, K. V Kovtunov, I. V Koptyug, A. Pines, NMR Imaging of Catalytic Hydrogenation in Microreactors with the Use of para-Hydrogen, Science. 319 (2008) 442–445. https://doi.org/10.1126/science.1151787.

[13] I. Koptyug, S. Altobelli, E. Fukushima, A. Matveev, R. Sagdeev, Thermally Polarized (1)H NMR Microimaging Studies of Liquid and Gas Flow in Monolithic Catalysts, J. Magn. Reson. 147 (2000) 36–42. https://doi.org/10.1006/jmre.2000.2186.

[14] I. V. Koptyug, L.Y. Ilyina, A. V. Matveev, R.Z. Sagdeev, V.N. Parmon, S.A. Altobelli, Liquid and gas flow and related phenomena in monolithic catalysts studied by1H NMR microimaging, Catal. Today. 69 (2001) 385–392. https://doi.org/10.1016/S0920-5861(01)00396-0.

[15] L.F. Gladden, J. Mitchell, Measuring adsorption, diffusion and flow in chemical engineering: Applications of magnetic resonance to porous media, New J. Phys. 13 (2011) 035001. https://doi.org/10.1088/1367-2630/13/3/035001.

[16] M.H. Sankey, D.J. Holland, A.J. Sederman, L.F. Gladden, Magnetic resonance velocity imaging of liquid and gas two-phase flow in packed beds, J. Magn. Reson. 196 (2009) 142–148. https://doi.org/10.1016/j.jmr.2008.10.021.

[17] N.P. Ramskill, A.P.E. York, A.J. Sederman, L.F. Gladden, Magnetic resonance velocity imaging of gas flow in a diesel particulate filter, Chem. Eng. Sci. 158 (2017) 490–499. https://doi.org/10.1016/j.ces.2016.10.017.

[18] N.P. Ramskill, L.F. Gladden, A.P.E. York, A.J. Sederman, J. Mitchell, K.A.

Hardstone, Understanding the operation and preparation of diesel particulate filters using a multi-faceted nuclear magnetic resonance approach, Catal. Today. 216 (2013) 104–110. https://doi.org/10.1016/j.cattod.2013.06.023.

[19] J.D. Cooper, A.P.E. York, A.J. Sederman, L.F. Gladden, Measuring velocity and turbulent diffusivity in wall-flow filters using compressed sensing magnetic resonance, Chem. Eng. J. (2019) 119690. https://doi.org/10.1016/j.cej.2018.08.076.

[20] L. Huang, Methods for Characterization of Mass Transport in Porous, Doctoral dissertation, University of Bremen, 2017.

[21] C.L. Dumoulin, S.P. Souza, R.D. Darrow, N.J. Pelc, W.J. Adams, S.A. Ash, Simultaneous acquisition of phase-contrast angiograms and stationary-tissue images with Hadamard encoding of flow-induced phase shifts, J. Magn. Reson. Imaging. 1 (1991) 399–404. https://doi.org/10.1002/jmri.1880010403.

[22] N.J. Pelc, M.A. Bernstein, A. Shimakawa, G.H. Glover, Encoding strategies for three-direction phase-contrast MR imaging of flow, J. Magn. Reson. Imaging. 1 (1991) 405–413. https://doi.org/10.1002/jmri.1880010404.

[23] A. Della Torre, G. Montenegro, G.R. Tabor, M.L. Wears, CFD characterization of flow regimes inside open-cell foam substrates, Int. J. Heat Fluid Flow. 50 (2014) 72–82. https://doi.org/10.1016/j.ijheatfluidflow.2014.05.005.

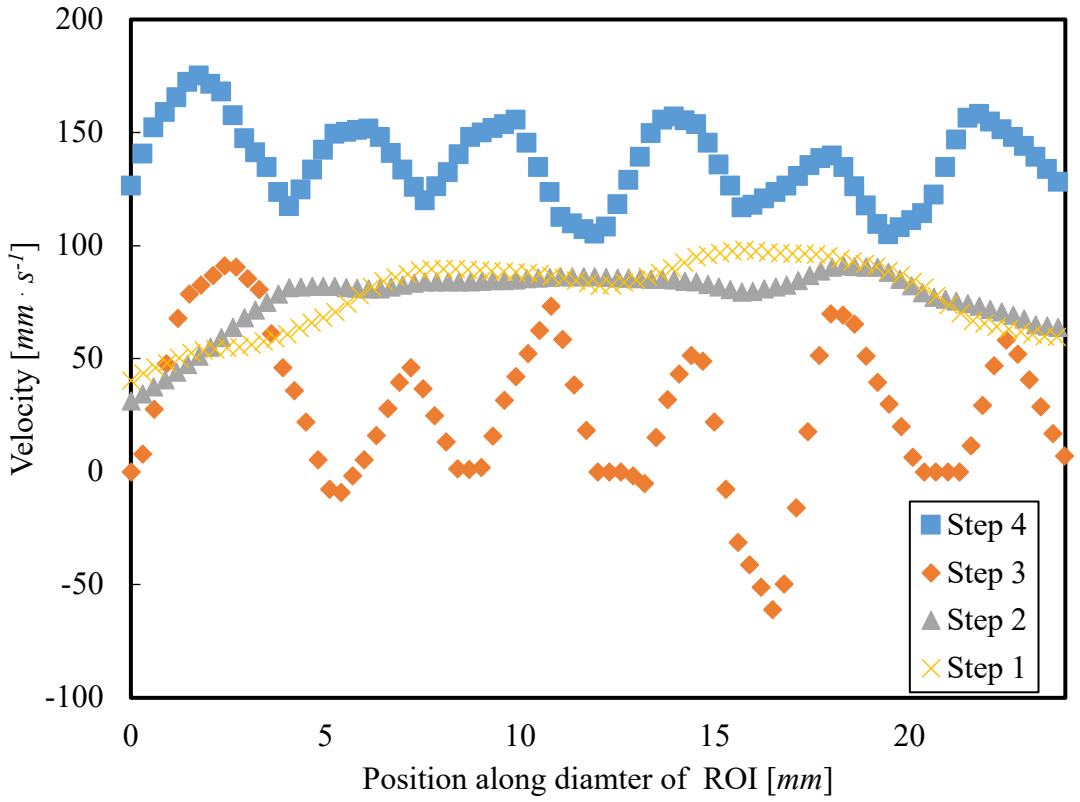

Figure S1. The axial component of flow at inlet region for ROI(1) along lines 1 to 4 in Fig. 4.8 determined by MRV. Yellow and gray show the bulk flow approaching the honeycomb. Brown shows the flow at the interface of flow and solid structure, where the contraction takes place. Blue represents the velocity profile in the monolith channels.

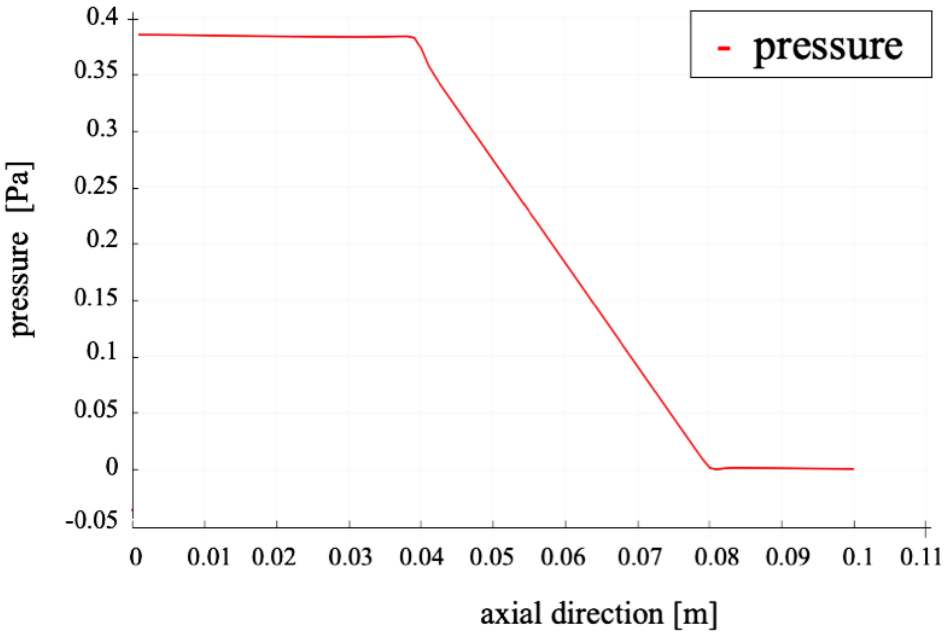

Figure. S2. Pressure drop curve obtained for 3D-printed honeycomb in CFD simulations along the length of the sample, including the entrance and exit regions represented on x-axis.

As described in the literature [19] the major pressure loss in honeycomb monoliths is expected to occur at entrance and exit region due to the contraction and expansion of flow. Here the pressure drop was computed by the CFD simulation within a channel in the flow direction. Due the regularity of the structure a linear pressure drop of 0.37 Pa was obtained. Although not shown, in a cross sectional cut of the channels the pressure remains unchanged in each channel. However, the pressure varies in radial orientation of each channel.

Chapter 5

Temperature*

Abstract: *In situ* thermometry of catalytic gas phase reactions allows for determining temperature profiles in the catalyst bed. In NMR imaging systems used for measuring the chemical composition of species in model reactors, temperature measurements by NMR spectroscopy are technically challenging and confined to a rather low temperature range. In this study, an optimized NMR *in situ* technique is proposed, which will allow to determine the temperature distribution in highly exothermic reactions on structured catalysts. Diffusion weighted magnetic resonance imaging (DW-MRI) was successfully applied as an alternative method for temperature measurements commonly performed by chemical shift measurements using ethylene glycol. DW-MRI applied with different diffusion sensitizing gradients allows high-resolution imaging of the temperature dependent diffusion coefficient, without the need for high spatial homogeneity of the magnetic field. Using 3D DW-MRI on ethylene glycol, glycerol, and the temperature stable ionic liquid Pyr_{13} [TFSI] (decomposition temperature 400 °C) as NMR thermometer, measurements were performed in a temperature range from 20 to 160 °C. The proposed method can be used in reaction engineering approaches performed in NMR systems.

Keywords: temperature, *in situ*, NMR, diffusion-weighted imaging DW-MRI, heterogeneous catalyst.

* The content of this chapter has already been published: **Mirdrikvand, M.**, Ridder, H., Thöming, J. and Dreher, W., 2019. Diffusion weighted magnetic resonance imaging for temperature measurements in catalyst supports with an axial gas flow. *Reaction Chemistry & Engineering*, *4*(10), pp.1844-1853.

5.1. Introduction

In chemical industry, a large number of processes includes reactions driven by heterogeneous catalysts. Heterogeneous catalysts are consistently involved with complex gas-solid or liquid-solid interfaces that occur in pores and channels of the catalyst supports. This complex nature leads to an uneven distribution of temperature and composition in exothermic reaction systems such as the Sabatier process, Fischer-Tropsch synthesis or hydrogenation reactions [1,2]. Therefore, proper *in situ* characterization methods are of great interest to extract vital information from these processes and to validate numerical simulations at micro and macro scale. The latter helps to achieve higher process efficiency and reduced industrial costs as well as to predict possible risks at large-scaled reactors. In particular, measuring temperature profiles in radial and axial direction of a reactor filled with catalysts helps to better understand the variation of temperature in the catalyst body, define realistic values for boundary conditions in numerical simulations, and reduce the threat of thermal runaway by predicting the formation of hot spots in reactors.

Different techniques have been applied to measure temperature of monolithic catalysts under reaction conditions. Conventional tracers give a limited point-wise information about the temperature by inserting thermocouples through the catalyst body [3]. Unlike conventional methods, the other *in situ* techniques including infrared thermography, near-infrared diffuse transmittance tomography, and X-ray diffraction (XRD) are non-invasive and the use of them has grown tremendously in recent years [4–7]. However, all these methods have certain limitations, especially when an opaque reactor is studied [8–11]. Nuclear Magnetic Resonance (NMR) methods are another well-known non-destructive approach for the quantitative characterization of transport processes and chemical reactions in chemical engineering. NMR is even more advantageous when a spatially resolved study of opaque reactors is performed. Moreover, NMR allows measurements of many different process characteristics such as temperature, velocity, diffusion and composition of species under identical reaction conditions.

NMR thermometry is based on the measurement of indirect parameters such as chemical shift difference, relaxation time of longitudinal magnetization, self-diffusion coefficient,

and signal intensity. All these parameters can affect the NMR signal in case of a variation in temperature.

Among the aforementioned approaches, localized NMR spectroscopy and Magnetic Resonance Spectroscopic Imaging (MRSI) are most often the method of choice to analyze temperature of the catalyst bed in reaction engineering approaches [8,12–15]. To perform these experiments, very thin glass made capillaries or capsules, referred to as "NMR thermometers", are filled with a probing liquid. In each volume element (voxel), the chemical shift difference between different spectral peaks of the probing liquid is determined. The temperature can be measured using the known relation between temperature and the chemical shift difference between two peaks. Therefore, the method does not depend on an external reference.

In reaction engineering, ethylene glycol has been used as a temperature probe in the catalyst support, measuring the chemical shift difference between the OH and the CH_2 signals [8,14–16]. It could be shown that the measurements were in very good agreement with simulations of temperature profiles in a heterogeneous catalytic reaction [17]. However, the applicability of this approach is limited by the liquid's boiling point (197.3 °C at ambient pressure) and the limited separation of both signals caused by the decreasing chemical shift difference with increasing temperature. Additionally, MRSI highly depends on the spatial homogeneity of the static magnetic field, which limits the applicability of the method at elevated temperatures, where the spectral peaks overlap one another and hamper accurate temperature measurements. Thus, only temperatures up to 150-160 °C can be measured by MRSI of ethylene glycol.

Therefore, an alternative method is essential to extend the temperature range and overcome the need for high field homogeneity. For biomedical MRI, several techniques have been proposed for temperature mapping. In particular, the temperature dependence of the chemical shift, the diffusion coefficient or the spin-lattice relaxation time T_1 of water has been exploited for spatially resolved temperature measurements in humans and animals [18–22]. Since diffusion weighted MRI (DW-MRI) has found widespread use in biomedical and clinical MRI [20,23], numerous fast DW-MRI pulse sequences have been developed [24]. Hence, DW-MRI can be a solution for temperature

measurements in an extended temperature range using NMR thermometers filled with liquids exhibiting high boiling points, such as glycerol (boiling temperature of 289 °C) or ionic liquids (chemical decomposition at temperatures above 400 °C).

The aim of this work is to support the hypothesis that DW-MRI can be used as a tool for determining temperatures in broad and high temperature ranges. Since DW-MRI is more robust against magnetic field inhomogeneities as compared to MRSI, temperature measurements by DW-MRI might also be an interesting alternative for temperature ranges to which MRSI of ethylene glycol can be applied. A comparison of MRSI and DW-MRI, which displays the dependency of MRSI to field inhomogeneities is included in the Chapter 6. An optimized DW-MRI sequence was applied to measure the diffusion coefficient and, thus, the temperature using three NMR thermometers filled with ethylene glycol, glycerol or the ionic liquid Pyr_{13} [TFSI]. MRSI of ethylene glycol was used for comparison. Furthermore, fiber optical temperature sensors were placed in the reactor, allowing an estimation of the temperature stability during the measurements. Optimized 3D DW-MRI acquires images with high spatial resolution using different diffusion sensitizing gradients corresponding to different diffusion weightings. The acquired NMR data were analyzed automatically to accelerate the evaluation of the NMR data in a robust and reliable way.

5.2. Theory and method

The effect of diffusion on the NMR signal amplitude was already recognized in an early publication by Hahn [25]. Stejskal and Tanner proposed accurate diffusion measurements by incorporating a pair of diffusion sensitizing gradients into a spin echo sequence (cf., Fig. 5.1) [26]. Diffusion characterized by the diffusion coefficient D causes a damping of the NMR signal amplitude according to

$$S = S_0 \cdot e^{-b \cdot D} \tag{5.1}$$

where S and S_0 are the signal amplitudes measured with and without diffusion sensitizing gradients, respectively. The so-called "b-value" b, which determines the strength of diffusion weighting, is given by

$$b = \gamma^2 \cdot G^2 \cdot \delta^2 \cdot \left(\Delta - \frac{\delta}{3}\right) \tag{5.2}$$

with the gyromagnetic ratio γ, the gradient strength G, the duration δ of each diffusion sensitizing gradient, and the delay Δ between the gradient pulses (cf. Fig. 5.1). The diffusion coefficient D can be determined by fitting the signal intensities, which are measured in at least two scans with different b-values, to Eq. 5.1.

To estimate the temperature dependence of the diffusion coefficient D, different approaches are reported in the literature. For instance, in case of self-diffusion of ethylene glycol, the temperature dependence of the diffusion coefficient can be predicted based on the following equation validated by Mitchell et al. [27]:

$$D(T)_{ethylene\ glycol} = A_0 \cdot T \cdot \ exp\ \left(-\frac{E_a}{RT}\right), \tag{5.3}$$

with the pre-exponential factor A_0, the activation energy E_a and the universal gas constant R.

For glycerol, the glass transition temperature of T_0 = −93.15 ˚C has to be considered, leading to the following relation proposed by Tomlinson [28].

$$D(T)_{glycerol} = A_0 \cdot T^{1/2} \cdot exp\ \left(-\frac{E_a}{R\ (T-T_0)}\right). \tag{5.4}$$

As described by Lesch et al. (Lesch et al, 2014), a similar consideration can be done for temperature stable ionic liquids, where the diffusion coefficient for the ionic liquid Pyr_{13} [TFSI] can be described by

$$D(T)_{ionic\ liquid} = A_0 \cdot exp\left(-\frac{E_a}{R(T-T_0)}\right), \tag{5.5}$$

with the glass transition temperature of $T_0 = -112.15$ °C.

For each liquid, the corresponding diffusion-temperature dependence is used, so the acquired data can be compared over the whole temperature range to literature data.

Mapping the local diffusion coefficient and consequently the temperature by DW-MRI is of great use in engineering science, e.g. for temperature measurements in a model reactor filled with an opaque catalytic material. However, for such applications the pulse sequence used for DW-MRI has to be chosen carefully. First, 3D spatial resolution is required to avoid restriction as to the geometry and position of the NMR temperature probes. Second, pulse sequences with a spin echo preparation period should be used to allow diffusion sensitization and avoid signal losses by magnetic field inhomogeneities. Third, data acquisition by a multi-echo train will reduce the minimum total measurement time because more spatial encoding steps can be performed per excitation. Fourth, for the echo train, radiofrequency (RF) refocusing should be preferred over gradient refocusing because rather low B_0 homogeneity and thus short effective transverse relaxation times T_2^* are expected for experimental setups such as NMR compatible model reactors.

Following these requirements, a 3D DW-SE-U-FLARE sequence (diffusion weighted spin echo ultrafast low angle rapid acquisition with relaxation enhancement) [29,30] was implemented (cf., Fig. 5.1). After the 90° excitation pulse, unipolar diffusion sensitizing gradients of strength G_d and duration δ are applied prior to and after the 180° refocusing pulse. Optionally, slice selection gradients can be applied if the object does not fit into the FOV and only a certain part of the object is to be measured (zoom). The diffusion weighted transverse magnetization is refocused by a train of RF pulses with flip angle α. After N_d dummy cycles used to stabilize the echo amplitude, N_pe1 echoes are acquired under a read gradient, each sampled with different spatial phase encoding using the phase encoding gradient G_pe. In N_pe2 experiments, additional spatial phase encoding is applied prior to the echo train for spatial resolution in the slice direction.

Displaced U-FLARE exploiting only one echo parity was used to avoid image artifacts in case of off-resonance effects [30].

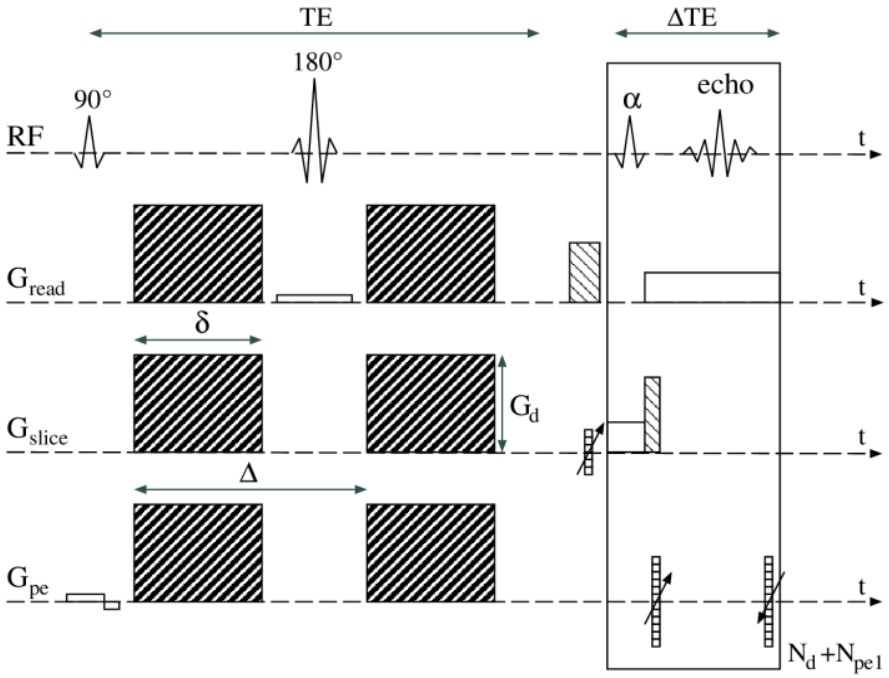

Figure 5.1. Scheme of the DW-SE-U-FLARE sequence (not to scale). The four rows display the applied radiofrequency pulses and the detected echo signals as well as the gradient pulses used for diffusion weighting and spatial localization. All acronyms are explained in detail in the text.

5.3. Materials

This section describes the chemicals used as NMR thermometers and the design of the NMR compatible vessel as a model reactor, which was used for measurements at fixed temperature points.

5.3.1. Chemicals

Three liquids were investigated as NMR thermometers. Ethylene glycol (≥ 99.7% purity, VWR International GmbH, Germany) was used as reference substance. Ethylene glycol was also used for MRSI measurements for comparison with DW-MRI. However,

since the rather low boiling point of ethylene glycol limits the fields of application, liquids with higher boiling point or high decomposition temperature are needed. Thus, glycerol (≥ 99.5% purity, Carl Roth GmbH, Germany) and 1-Methyl-3-propylpyrrolidinium bis (trifluoromethylsulfonyl)imide (Pyr_{13} [TFSI]) (99% purity, Ionic Liquids Technologies (IoLiTec) GmbH, Heilbronn, Germany) were chosen as alternative NMR thermometers. The choice of the ionic liquid was due to its high decomposition temperature (above 400 °C), which facilitates temperature measurements for a variety of reactions taking place up to this level. The liquids were each filled into capillaries (OD = 0.7 mm, ID = 0.55 mm) made of borosilicate and then sealed by melting the edges.

The capillaries were aligned through the channels of a cordierite honeycomb monolith used as catalyst support (length: 38 mm, diameter: 25 mm, 600 cells per square inch (cpsi); NGK, Poland). In some experiments, two capillaries were used for each probing liquid to assess the consistency of the measured data for individual capillaries in a thermally homogenous system.

Ambient temperature was used as a starting point. Then, the temperature was increased in different steps. At each step waiting for a time of approx. Forty-five minutes were required, until the fiber optical thermometer indicated that steady state is achieved. After the steady state was achieved the NMR measurements were performed as described in section 5.3.3.

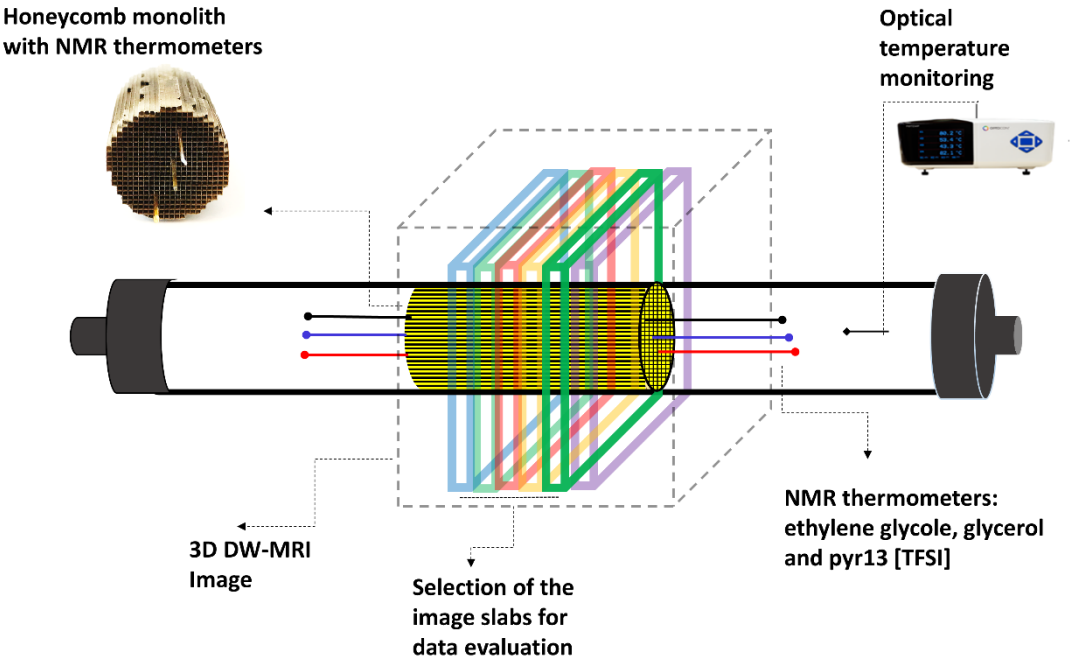

Figure 5.2. Scheme of the setup for thermometry using aligned NMR thermometers in the monolith support and an optical temperature monitoring system. 3D DW-MRI enables spatially resolved temperature measurements from the catalyst bed using NMR thermometers. Arbitrary slices can be analyzed from 3D images to determine the temperature.

5.3.2. Model reactor

An NMR compatible model reactor (length: 80 cm, inner diameter: 26 mm) was developed to operate at elevated temperature conditions in the MRI scanner. Pressurized air was heated up and led to the vessel to obtain the desired temperature. It was preferred to use this external heating mechanism over heating by reaction, as each reaction is only applicable in a specific temperature range. Furthermore, possible spatial temperature inhomogeneities due to an inhomogeneous concentration profile can be avoided. The setup was also equipped with a cooling system to prevent damage or detuning of the RF coil. For this purpose, a bank of PTFE tubes, in which a hydrogen-free coolant was circulating, was used. A cryostatic temperature regulator was used to cool the coolant

to −5 °C. The air temperature was measured by a resistance thermometer at the inlet of the setup.

In addition to NMR measurements by MRSI and DW-MRI, an MRI compatible Gallium arsenide-based fiber optic temperature monitoring system (FOTEMP-4, Weidmann Technologies Deutschland GmbH, Dresden, Germany) was used for accurate temperature measurements near the catalyst support. The sensor was placed in the vessel with 10 cm distance from the honeycomb monolith (cf., Fig. 5.2). The sensor was primarily used as a safety monitoring element and to check the temperature stability during NMR measurements.

5.3.3. NMR Measurements

A 7 Tesla preclinical NMR imaging system (Biospec 70/20, Bruker Biospin GmbH, Ettlingen, Germany) equipped with a gradient system BGA12S2 (441 $mT \cdot m^{-1}$ maximum gradient strength in each direction, 130 μs rise time) was used for all measurements. A quadrature birdcage RF coil (inner diameter of 72 mm) was used for RF excitation and signal detection. The NMR pulse sequences were implemented using the software platform Paravision 5.1.

DW-MRI: SE-DW-U-FLARE was used with the following parameters: FOV = 48×48×48 mm^3; matrix size 128×64×16, slice thickness 48 mm; 4 averages to increase the SNR with N_d = 5, 6, 7, or 8 to suppress remaining instabilities of the echo amplitudes; N_{pe1} = 64, interecho delay 5.3 ms with centered phase encoding in the U-FLARE echo train, N_{pe2} = 16, repetition time TR = 3 s; 90° slice selective refocusing pulse. Different sets of measurements, each with four *b*-values, starting at 50 $s \cdot mm^{-2}$ and with an equidistant increment of the applied gradient of Δb = 250, 1000, 2000, 5000, 15000 $s \cdot mm^{-2}$ were used to account for the large range of diffusion coefficients measured for different liquids at different temperatures. For each set of measurements, only four *b*-values were used in the interest of a short total measurement time. During data processing the best suited set of *b*-values was used for each combination of liquid and temperature. The measurement time for each scan with four *b*-values was ~13 min.

MRSI: An optimized 3D MRSI pulse sequence was used and the data were evaluated as described in detail in a previous publication [14]. The main experimental parameters were: echo time TE = 350 µs (delay between RF excitation and start of data acquisition), FOV = 63×63×126 mm^3, matrix size: 42×42×42 with spherically reduced *k*-space sampling, repetition time TR = 12.5 ms, one average yielding a total measurement time of 7 min 32 s.

5.4. Results and discussion

This section is divided into three main parts. In the first part, the automatic evaluation of DW-MRI images and the procedure to obtain diffusion coefficients are described. In the second part, the results are compared to the literature and theoretical predictions. Finally, we suggest a strategy for the selection of *b*-values to make the measurement procedure more efficient.

5.4.1. Automatic data analysis

The MRSI data sets were analyzed using an in-house developed IDL (Interactive Data Language, version 7.0, Exilis Visual Information Solutions, Bolder, USA) software program. After apodization with a Hamming function and Fourier transformation along the three spatial directions, the matrix pencil method (MPM) [31] was used to fit the data for ethylene glycol capillaries. The temperature was determined from the chemical shift values of the two signals detected by the MPM method [14,16]. Since the highest B_0 homogeneity is given in the iso-center of the magnet, the temperatures were determined for three central slices of the ethylene glycol capillaries using the temperature dependent chemical shift difference in the MRSI data. These values were compared to the values determined in the same slices of the 3D DW-MRI data for the three thermometers. No significant temperature differences between the three slices were observed.

The reconstructed DW-MRI images were stored as 32-bit data by the Paravision 5.1 software package. Fig. 5.3 depicts the generated diffusion weighted images of the thermometers. An in-house developed MATLAB (R2017b, The MathWorks, Inc.,

Natick, USA) script was used for automated data analysis of the images in order to locate the capillaries in each slice, select the central position and pick the Regions of Interest (ROI) for the thermometers. To this end, a noise filter was applied for better visualizing the images (cf., Fig. 5.3) and detecting the centers of the capillaries, while the signal intensity of the images stays intact for further evaluations. Those images of slices close to the iso-center of the magnet and possessing lowest *b*-value were used to define the ROI in each data set for further data analysis. Next, the signal intensities within the selected ROIs were added to obtain a value for the total signal intensity. To further increase the accuracy, those slices located far from the iso-center were also reanalyzed by examining neighboring slices to ensure that no physical shift of the thermometers has occurred and the central peak of each capillary was correctly chosen. Note that the size of ROIs remains constant for a given capillary during the analysis. For a central slice of the ethylene glycol capillary, the spatial signal distributions around the signal maxima are illustrated in Fig. 5.4 for four different *b*-values. Note that the four 3D surface plots are uniformly scaled, but the same color map is used in each subfigure for better visibility.

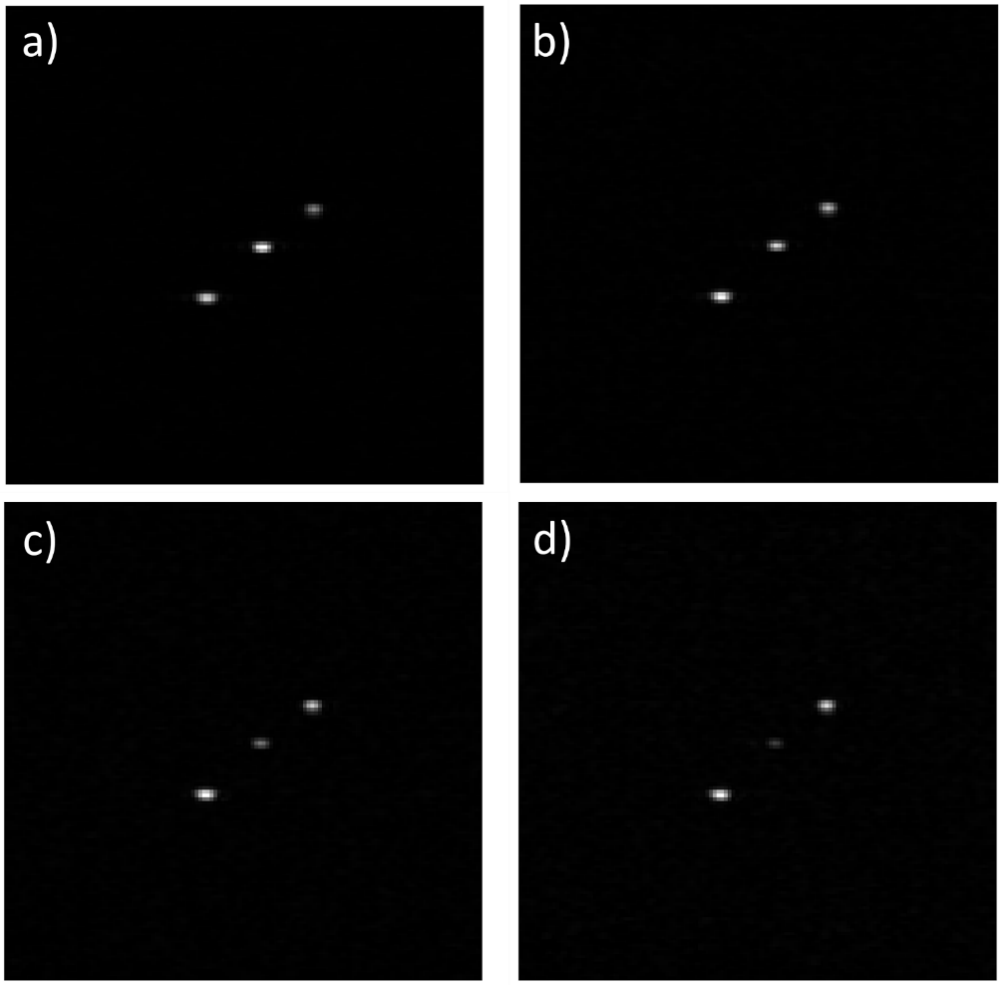

Figure 5.3. Diffusion weighted images for three NMR thermometers filled with ionic liquid Pyr_{13} [TFSI] (top right), ethylene glycol (middle) and glycerol (bottom left) measured at a temperature of 78 °C. The images were measured with different diffusion weighting using *b*-values of 50, 2050, 4050, and 6050 $s \cdot mm^{-2}$ (Δb = 2000 $s \cdot mm^{-2}$) for a, b, c, and d, respectively. Note that the differences in signal intensity correspond to the different diffusion coefficients of the three liquids. The signal intensities are plotted versus b-value in Fig. 5.5.

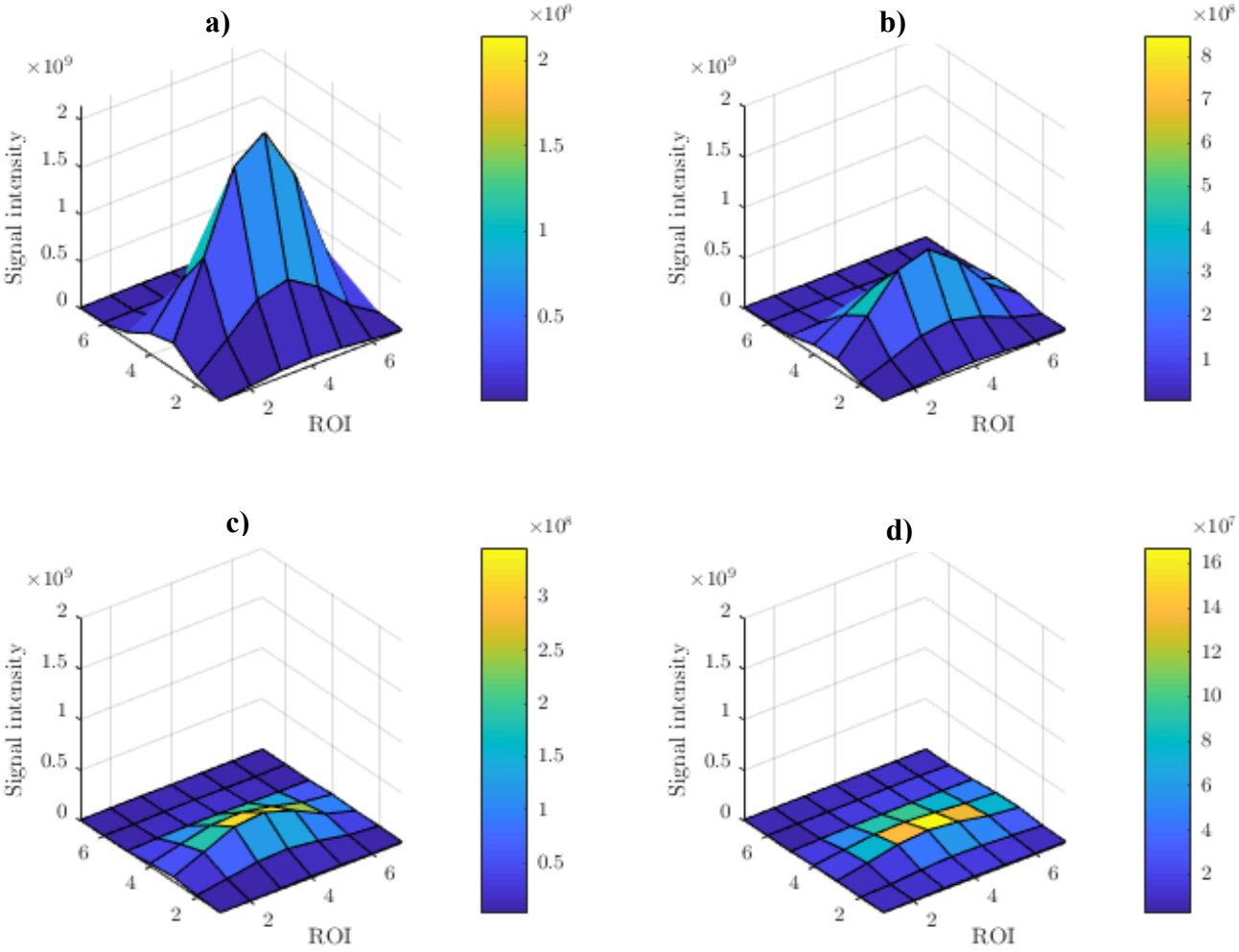

Figure 5.4. Signal intensities around the signal maxima for the ethylene glycol thermometer based on DW-MR images using *b*-values of 50, 2050, 4050, and 6050 s·mm^{-2} for a, b, c, and d, respectively (cf., Fig. 5.3).

Finally, the temperature dependent diffusion coefficients were estimated for each capillary by fitting the signal intensities determined for different *b*-values to Eq. 5.1.

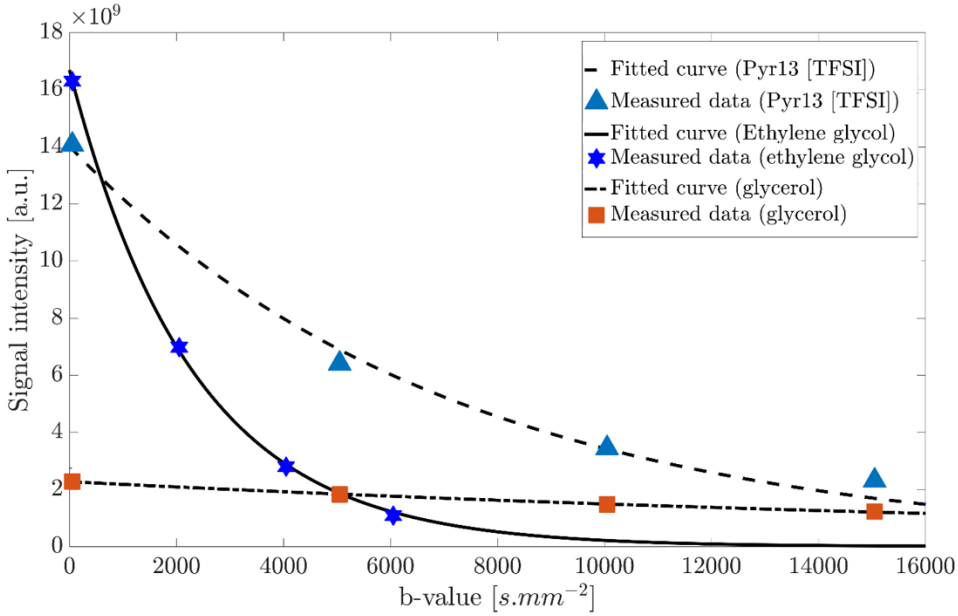

Figure 5.5. Signal intensity versus b-value for Pyr_{13} [TFSI], ethylene glycol, and glycerol measured at 78 °C. The diffusion coefficient can be obtained by fitting the values using Eq. 5.1 ($D_{\mathrm{Pyr13[TFSI]}} = 1.40\times10^{-4}$ mm^2 ·s^{-1}, $D_{ethylene\ glycol} = 4.34\times10^{-4}$ mm^2 ·s^{-1}, and $D_{\mathrm{glycerol}} = 4.20\times10^{-5}$ mm^2 ·s^{-1}, $R^2 > 0.98$). Note that a small offset of the curve may occur due to the mean noise level of the image calculated in the magnitude mode. Optimal Δb values were chosen for fitting the data as discussed later in section 5.4.3.

5.4.2. Diffusion coefficients

In this section, the diffusion coefficients measured at different temperatures are shown and compared to literature data. After the thermal steady state was achieved and prior to the DW-MRI measurements, the temperature values were measured by MRSI of ethylene glycol with a standard deviation of ~1.5 °C.

5.4.2.1. Ethylene glycol

The measured diffusion coefficients for ethylene glycol thermometers as well as literature values [27,32] are plotted in Fig. 5.6a. The curve predicted by Mitchell et al. based on theoretical assumptions [27] (Eq. 5.3) is also superimposed as theory curve.

The diffusion coefficients observed in the current study are in strong agreement with the experimental values published in the literature. In addition, the results match the prediction from theory [27]. The observed agreement between experimental data, literature values and theory proves the accuracy of DW-MRI.

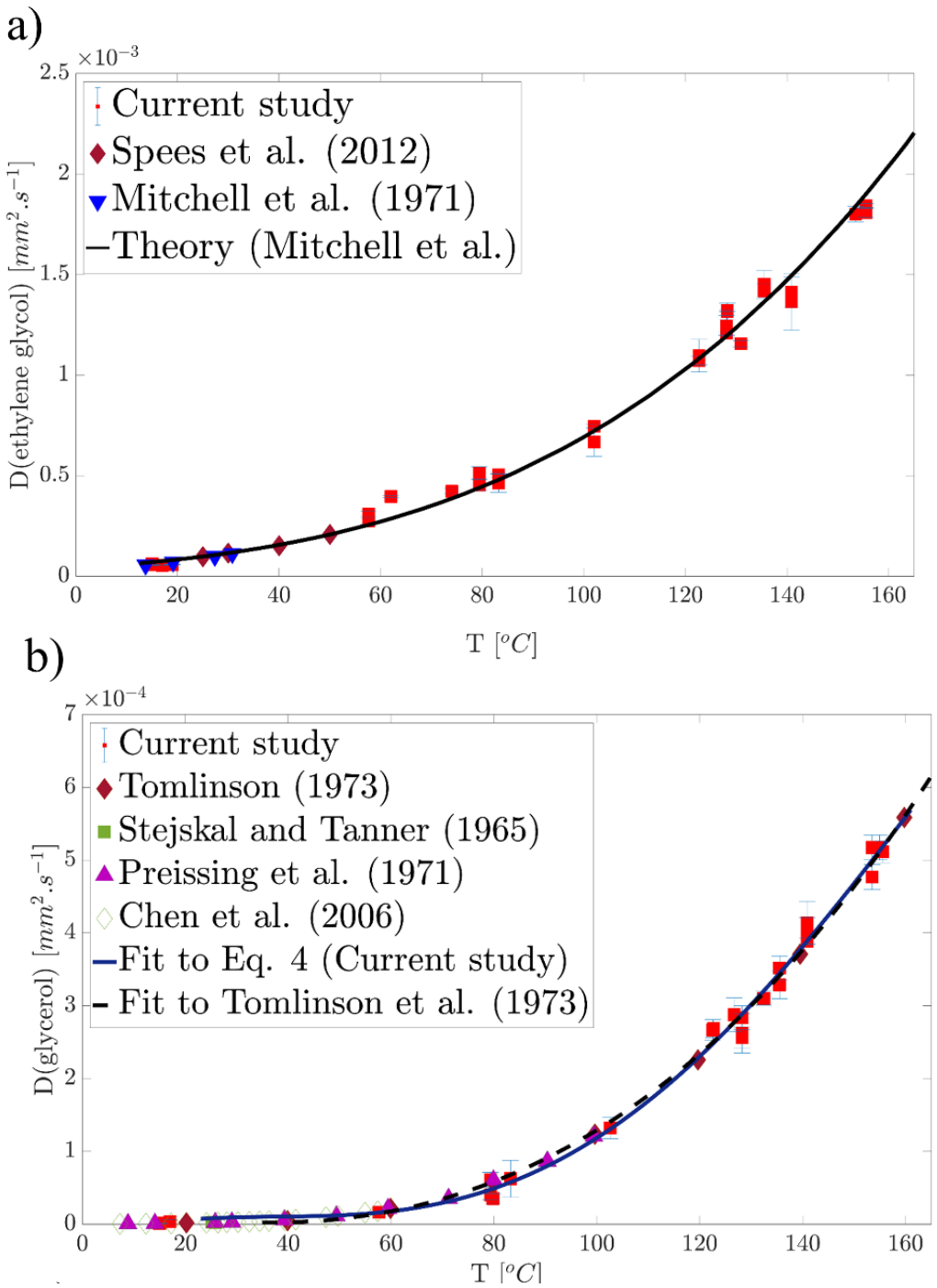

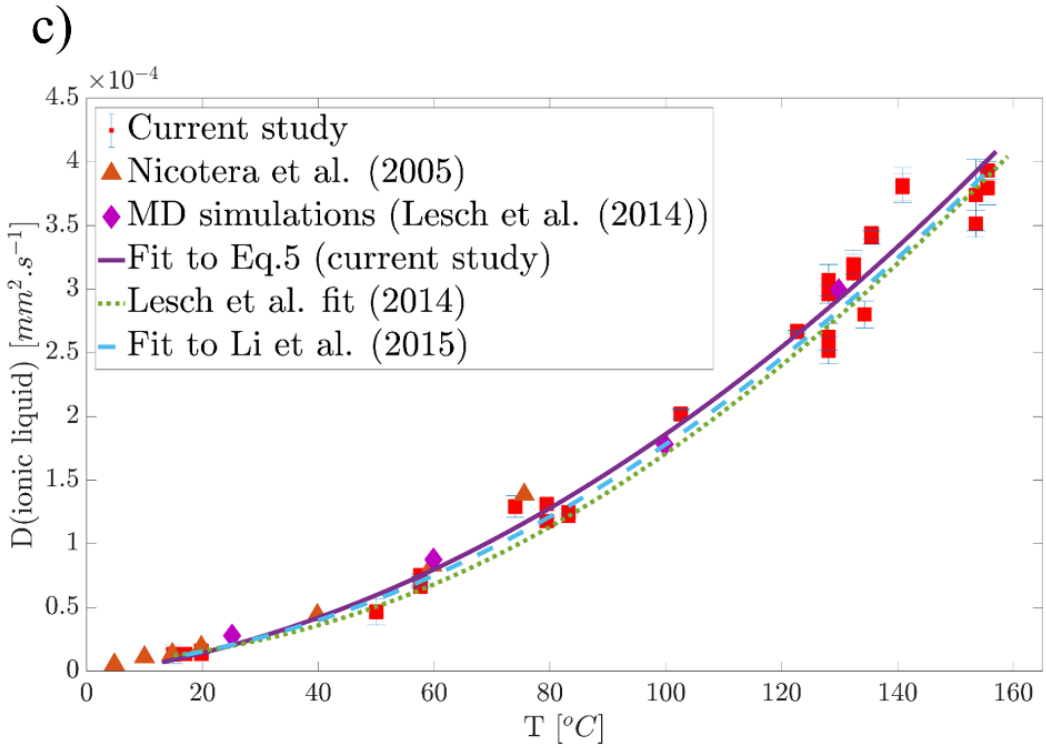

Figure 5.6. Diffusion coefficient of (a) ethylene glycol, (b) glycerol, and (c) Pyr_{13} [TFSI] over temperature.

5.4.2.2. Glycerol

The diffusion coefficients obtained in the current study and literature values [26,28,33,34] are plotted in Fig. 5.6b. The proposed fit of Tomlinson is also shown (Eq. 5.4) with the fitted curve from the current data ($R^2 = 0.99$) with solid and dashed line, respectively. Data measured in the current study shows very good agreement with the literature values and the fitted curve from Tomlinson. The high accuracy obtained in the measurement enables using glycerol as a standard NMR thermometer for reactions that occur with maximum temperature of < 290 °C at ambient pressure.

5.4.2.3. Ionic liquid

The measured diffusion coefficients for the ionic liquid Pyr_{13} [TFSI] are depicted in Fig. 5.6c. This figure also contains results of molecular dynamic simulations performed by Lesch et al. [35,36] as well as Vogel-Tammann-Fulcher (VTF) function [37] (Eq. 5.5)

to predict the temperature dependence of the diffusion coefficient. The diffusion coefficients published by Nicotera et al. were also added to the figure [38]. The diffusion coefficients measured by DW-MRI match experimental data from the literature and show a good agreement with VTF fits (R^2 = 0.98) and MD simulation data. Thus, the chosen ionic liquid is a promising liquid as NMR thermometer for reactions taking place up to 400 °C, a temperature range that is of great interest for studying reactions such as methanation or Fischer-Tropsch reaction.

5.4.3. Selection of *b*-values

Since the diffusion weighted signal decays by a factor of $exp(-b \cdot D)$ and the diffusion coefficients D, of the three liquids vary from each other, appropriate diffusion weighting (b-values) should be applied in order to measure D with high precision. An efficient prediction of the optimal diffusion weighting leads to a better design of experiments and thus shorter total measurement time. In the following, we analyze the use of the different sets of b-values for DW-MRI of the three NMR thermometers. In addition, a comparison between the theoretical assumptions and the applied gradient strengths at each temperature point is conducted. To do this, a theoretical assessment was conducted via the Cramer-Rao Lower Bound Theory (CRLB) [39] to predict optimal Δb values for a given diffusion coefficient if four b-values and a simple exponential model are used. The CRLB values describe the minimum error of estimated parameters of a model function fitted to experimental data. The results of the analysis are illustrated in Fig. 5.7a where the CRLB errors are plotted versus the diffusion coefficients for the different Δb values. Basically, with increasing temperature the desired Δb decreases. This is due to higher diffusivity of the liquids as a result of lower viscosity at higher temperatures. During the measurement an online analysis of the fitted curves was conducted in order to calculate the fitting error for a specific set of b-values. The lowest fitting error was used to determine the optimum diffusion weighting at each temperature. The Δb values applied for the three liquids at different temperatures are illustrated in Fig. 5.7b. The determined optimal Δb values are in very good agreement with CRLB predictions. Thus,

Fig. 5.7 gives a straightforward choice of appropriate Δb values in diffusion measurement for the different NMR thermometers.

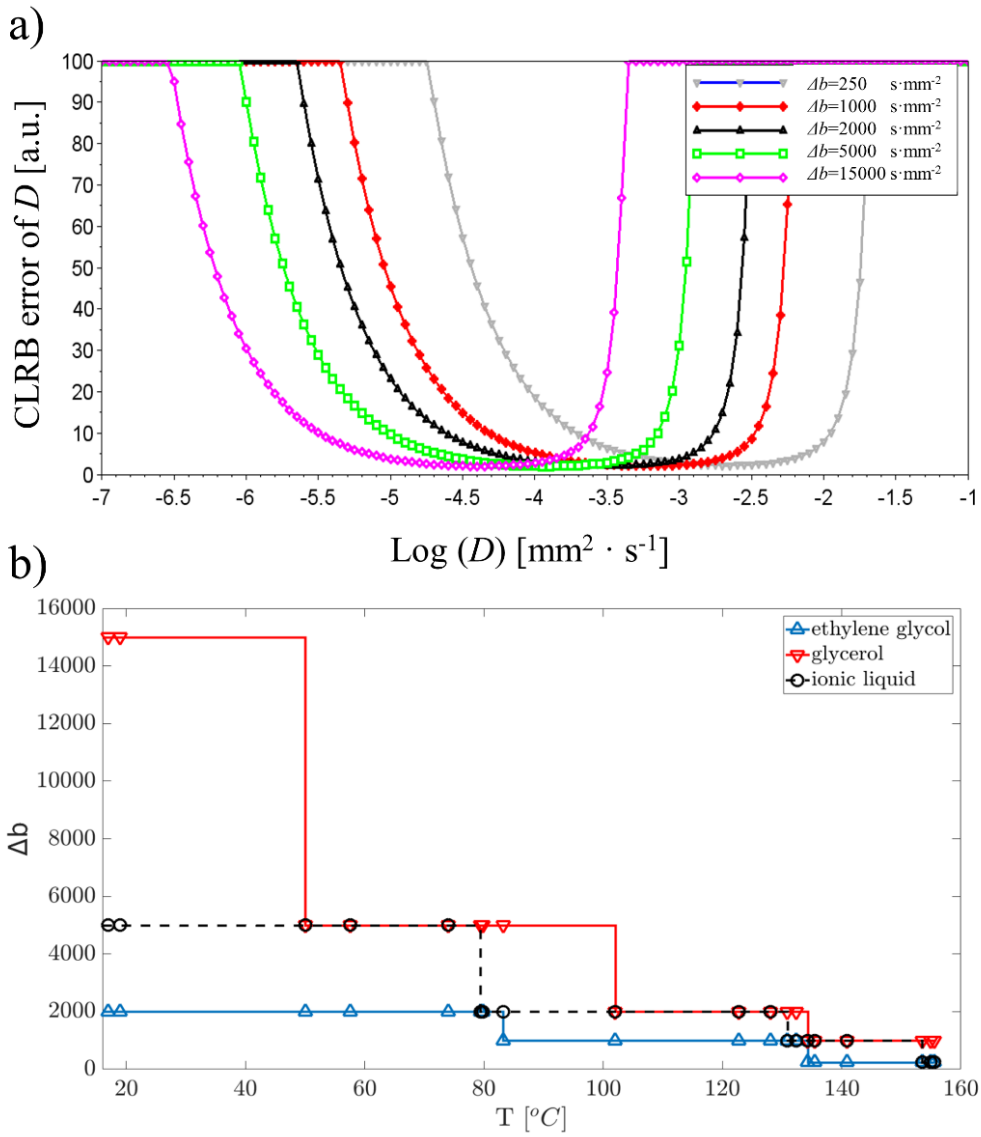

Figure 5.7. (a) Minimum error of the diffusion coefficient determined from the DW-MRI measurements with four *b*-values plotted versus the diffusion coefficient *D*. The error was determined in arbitrary units as Cramer-Rao lower bounds for different Δb values (diffusion weighting). (b) Selection of the optimal Δb out of five applied Δb values for diffusion measurements based on the smallest Cramer-Rao lower bounds. The optimal Δb values are depicted versus temperature for the three NMR thermometers.

5.4.4. General discussion and outlook

The results of the study confirm that the proposed DW-MRI method works very well and can measure the temperature of the catalyst bed. The spatially resolved method enables in-plane measurements of the temperature to provide correct values for boundary conditions in numerical simulation. Three liquids were studied in order to propose three NMR thermometers, which target different temperature ranges for heterogeneously catalyzed reactions.

Comparing the values obtained in the current study and the corresponding data reported in the literature, DW-MRI shows a high accuracy in temperature measurements at elevated temperatures. The reproducibility of this approach has been proven by using different capillaries filled with the same liquid and repeating measurements at certain temperature points three times. The results obtained for the three probing liquids show the broad applicability of the applied method. Which liquid will be the NMR thermometer of choice, will depend on the specific applications. Even though ethylene glycol was mainly used for reference temperature measurements by MRSI, DW-MRI of ethylene glycol has proven its value for a temperature range < 160 °C, in particular in case of low B_0 inhomogeneity. Glycerol with its much lower diffusion coefficients requires strong b-values and is thus hardware demanding, particularly at low temperatures. However, glycerol will enable measurements at higher temperatures due to the boiling point of 289 °C and the large changes in D for a given temperature difference, leading to more precise results. The ionic liquid exhibits a moderate diffusion coefficient ($D_{\text{ethylene glycol}} > D_{\text{ionic liquid}} > D_{\text{glycerol}}$). Although the changes in D for a given temperature difference are smaller than for glycerol (cf. Figures 5.6b and 5.6c), the high decomposition temperature makes the ionic liquid a good candidate for temperature measurements up to 400 °C. The automatic analysis of the results is another advantage of the current approach. The automatic analysis not only increases the accuracy of the results, it also helps to probe temperature in an arbitrary region of the 3D image as soon as the diffusion weighted images are reconstructed.

The sets of b-values applied for the diffusion measurements show that a steady reduction in the chosen Δb is necessary as the temperature increases. The three NMR liquids have

different thermodynamic properties, which hindered the optimization of the measurements for a specific liquid used in an NMR thermometer. Therefore, it will be necessary to find an optimal selection of *b*-values for upcoming studies with a certain liquid.

Compared to the promising work published by Koptyug et al., in which the spin-lattice relaxation time T_1 and the signal intensity were used to measure temperature using ^{27}Al MRI in Al_2O_3 samples [40], the current thermometry by DW-MRI of probing liquids can be applied without using multinuclear NMR hardware. However, since capillaries or capsules have to be inserted into the catalyst support, the proposed approach is not completely non-invasive.

Indisputably, some improvements are necessary to apply the current method as a primary method for temperature measurement of heterogeneous catalysts. For instance, the DW-MRI sequence should be optimized, particularly to reduce the total measurement time and, thus, increase the time resolution of the temperature measurements. Additionally, the number of diffusion weighted experiments and the used *b*-values should be adjusted for a given NMR thermometer and the temperature range of interest.

5.5. Conclusion

A 3D DW-MRI approach for temperature measurements in heterogeneously catalyzed systems was applied. Using MRSI of ethylene glycol as a reference, the applicability of the method was proven. To be able to increase the feasible temperature range, glycerol and the ionic liquid Pyr_{13} [TFSI] were investigated as temperature stable liquids. In this way, measurements in broad and elevated temperature ranges are possible. The obtained results showed high accuracy and consistency with literature data. As compared to MRSI, the method is less sensitive to spatial inhomogeneities of the static magnetic field and allows rapid and robust measurements of high temperatures.

Acknowledgment

This work was supported by the German Research Foundation (DFG) in the frame of the Research Training Group GRK 1860 "Micro-, Meso- and Macro-Porous Nonmetallic Materials: Fundamentals and Application" (MIMENIMA) and by the Federal Ministry for Economic Affairs and Energy (BMWi) and the Federal Ministry of Education and Research (BMBF) in context of the research project "QUARREE 100 - Resilient, integrated and system-friendly energy supply systems in existing urban districts considering the complete integration of renewable energies" (grant number: 03SBE113B).

References

[1] M. V. Twigg, J.T. Richardson, Fundamentals and applications of structured ceramic foam catalysts, Ind. Eng. Chem. Res. 46 (2007) 4166–4177. https://doi.org/10.1021/ie061122o.

[2] L. Kiewidt, J. Thöming, Predicting optimal temperature profiles in single-stage fixed-bed reactors for CO2 methanation, Chem. Eng. Sci. 132 (2015) 59–71. https://doi.org/10.1016/j.ces.2015.03.068.

[3] S.B. Jaffe, Hot spot simulation in commercial hydrogenation processes, Ind. Eng. Chem. Process Des. Dev. 15 (1976) 410–416. https://doi.org/10.1021/i260059a011.

[4] D. Luss, M. Sheintuch, Spatiotemporal patterns in catalytic systems, Catal. Today. 105 (2005) 254–274. https://doi.org/10.1016/j.cattod.2005.02.043.

[5] B.T. Li, K. Maruyama, M. Nurunnabi, K. Kunimori, K. Tomishige, Effect of Ni loading on catalyst bed temperature in oxidative steam reforming of methane over alpha-Al2O3-supported Ni catalysts, Ind. Eng. Chem. Res. 44 (2005) 485–494. https://doi.org/10.1021/ie0493210.

[6] L.M. Plyasova, T.A. Kriger, A.A. Khassin, A.V.N. Parmon, Separate measurement of the active component and support temperatures for the Ni/MgO catalyst in the course of an exothermal reaction by in situ high-temperature X-ray powder diffraction, Dokl. Phys. Chem. 382 (2002) 47–50. https://doi.org/10.1023/A:1014403430436.

[7] G.M. Carlomagno, G. Cardone, Infrared thermography for convective heat transfer measurements, Exp. Fluids. 49 (2010) 1187–1218. https://doi.org/10.1007/s00348-010-0912-2.

[8] L.F. Gladden, F.J.R. Abegão, C.P. Dunckley, D.J. Holland, M.H. Sankey, A.J. Sederman, MRI: Operando measurements of temperature, hydrodynamics and local reaction rate in a heterogeneous catalytic reactor, Catal. Today. 155 (2010) 157–163. https://doi.org/10.1016/j.cattod.2009.10.012.

[9] A.A. Lysova, A. V. Kulikov, V.N. Parmon, R.Z. Sagdeev, I. V. Koptyug, Quantitative temperature mapping within an operating catalyst by spatially

resolved ^{27}Al NMR, Chem. Commun. 48 (2012) 5763–5765. https://doi.org/10.1039/c2cc31260c.

[10] I. V Koptyug, A. V Khomichev, A.A. Lysova, R.Z. Sagdeev, Spatially resolved NMR thermometry of an operating fixed-bed catalytic reactor, J. Am. Chem. Soc. 130 (2008) 10452–10453.

[11] I. V. Koptyug, Magnetic resonance imaging methods in heterogeneous catalysis, Spectrosc. Prop. Inorg. Organomet. Compd. 39 (2014) 1–42. https://doi.org/10.1039/9781782621485-00001.

[12] L.F. Gladden, M.D. Mantle, A.J. Sederman, Magnetic resonance imaging of catalysts and catalytic processes, Adv. Catal. 50 (2006) 1–75. https://doi.org/10.1016/S0360-0564(06)50001-X.

[13] L.F. Gladden, A.J. Sederman, Recent advances in Flow MRI, J. Magn. Reson. 229 (2013) 2–11. https://doi.org/10.1016/j.jmr.2012.11.022.

[14] J. Ulpts, W. Dreher, L. Kiewidt, M. Schubert, J. Thöming, In situ analysis of gas phase reaction processes within monolithic catalyst supports by applying NMR imaging methods, Catal. Today. 273 (2016) 91–98. https://doi.org/10.1016/j.cattod.2016.02.062.

[15] J. Ulpts, W. Dreher, M. Klink, J. Thöming, NMR imaging of gas phase hydrogenation in a packed bed flow reactor, Appl. Catal. A Gen. 502 (2015) 340–349. https://doi.org/10.1016/j.apcata.2015.06.011.

[16] A.L. van Geet, Calibration of the methanol and glycol nuclear magnetic resonance thermometers with a static thermistor probe, Anal. Chem. 40 (1968) 2227–2229. https://doi.org/10.1021/ac50158a064.

[17] J. Ulpts, L. Kiewidt, W. Dreher, J. Thöming, 3D characterization of gas phase reactors with regularly and irregularly structured monolithic catalysts by NMR imaging and modeling, Catal. Today. 310 (2018) 176–186. https://doi.org/10.1016/j.cattod.2017.05.009.

[18] H.E. Cline, K. Hynynen, E. Schneider, C.J. Hardy, S.E. Maier, R.D. Watkins, F.A. Jolesz, Simultaneous magnetic resonance phase and magnitude temperature maps in muscle, Magn. Reson. Med. 35 (1996) 309–315.

https://doi.org/10.1002/mrm.1910350307.

[19] J.C. Hindman, Proton resonance shift of water in the gas and liquid states, J. Chem. Phys. 44 (1966) 4582–4592. https://doi.org/10.1063/1.1726676.

[20] D. Le Bihan, J. Delannoy, R.L. Levin, Temperature mapping with MR imaging of molecular diffusion: application to hyperthermia., Radiology. 171 (1989) 853–857. https://doi.org/10.1148/radiology.171.3.2717764.

[21] Y. Zhang, T. V. Samulski, W.T. Joines, J. Mattiello, R.L. Levin, D. Lebihan, On the accuracy of noninvasive thermometry using molecular diffusion magnetic resonance imaging, Int. J. Hyperth. 8 (1992) 263–274. https://doi.org/10.3109/02656739209021781.

[22] P.A. Bottomley, T.H. Foster, R.E. Argersinger, L.M. Pfeifer, A review of normal tissue hydrogen NMR relaxation times and relaxation mechanisms from 1-100 MHz: Dependence on tissue type, NMR frequency, temperature, species, excision, and age, Med. Phys. 11 (1984) 425–448. https://doi.org/10.1118/1.595535.

[23] S. Warach, D. Chien, W. Li, M. Ronthal, R.R. Edelman, Fast magnetic resonance diffusion-weighted imaging of acute human stroke, Neurology. 42 (1992) 1717–1717. https://doi.org/10.1212/WNL.42.9.1717.

[24] M. Iima, D. Le Bihan, Clinical Intravoxel Incoherent Motion and Diffusion MR Imaging: Past, Present, and Future, Radiology. 278 (2016) 13–32. https://doi.org/10.1148/radiol.2015150244.

[25] E. Hahn, Spin echoes, Phys. Rev. 80 (1950) 580–594. http://link.aps.org/doi/10.1103/PhysRev.80.580.

[26] E.O. Stejskal, J.E. Tanner, Spin diffusion measurements: Spin echoes in the presence of a time-dependent field gradient, J. Chem. Phys. 42 (1965) 288–292. https://doi.org/10.1063/1.1695690.

[27] R.D. Mitchell, J.W. Moore, R.M. Wellek, Diffusion coefficients of ethylene glycol and cyclohexanol in the solvents ethylene glycol, diethylene glycol, and propylene glycol as a function of temperature, J. Chem. Eng. Data. 16 (1971) 57–60. https://doi.org/10.1021/je60048a003.

[28] D.J. Tomlinson, Temperature dependent self-diffusion coefficient measurements of glycerol by the pulsed N.M.R. technique, Mol. Phys. 25 (1973) 735–738. https://doi.org/10.1080/00268977300100661.

[29] D.G. Norris, Ultrafast Low-Angle RARE: U-FLARE, Magn. Reson. Med. 17 (1991) 539–542. https://doi.org/10.1002/mrm.1910170224.

[30] D.G. Norris, P. Börnert, T. Reese, D. Leibfritz, On the application of ultra-fast rare experiments, Magn. Reson. Med. 27 (1992) 142–164. https://doi.org/10.1002/mrm.1910270114.

[31] Y.Y. Lin, P. Hodgkinson, M. Ernst, A. Pines, A Novel detection-estimation scheme for noisy NMR signals: applications to delayed acquisition data, J. Magn. Reson. 128 (1997) 30–41. https://doi.org/10.1006/jmre.1997.1215.

[32] W.M. Spees, S.K. Song, J.R. Garbow, J.J. Neil, J.J.H. Ackerman, Use of ethylene glycol to evaluate gradient performance in gradient-intensive diffusion MR sequences, Magn. Reson. Med. 68 (2012) 319–324. https://doi.org/10.1002/mrm.23201.

[33] G. Preissing, F. Noack, R. Kosfeld, B. Gross, Zur Deutung der Protonenspinrelaxation in Glycerin, Zeitschrift Für Phys. 246 (1971) 84–90. https://doi.org/10.1007/BF01402653.

[34] B. Chen, E.E. Sigmund, W.P. Halperin, Stokes-Einstein relation in supercooled aqueous solutions of glycerol, Phys. Rev. Lett. 96 (2006). https://doi.org/10.1103/PhysRevLett.96.145502.

[35] V. Lesch, S. Jeremias, A. Moretti, S. Passerini, A. Heuer, O. Borodin, A combined theoretical and experimental study of the In fl uence of different anion ratios on lithium ion dynamics in ionic liquids, J. Phys. Chem. B. 118 (2014) 7367−7375. https://doi.org/10.1021/jp501075g.

[36] V. Lesch, Z. Li, D. Bedrov, A. Heuer, coordination and transport in ionic liquid electrolytes : a MD simulation study †, Phys. Chem. Chem. Phys. 18 (2016) 382–392. https://doi.org/10.1039/c5cp05111h.

[37] Z. Li, O. Borodin, G.D. Smith, D. Bedrov, Effect of organic solvents on Li + Ion solvation and transport in ionic liquid electrolytes : a molecular dynamics

simulation study, J. Phys. Chem. B. 119 (2015) 3085–3096. https://doi.org/10.1021/jp510644k.

[38] I. Nicotera, C. Oliviero, W.A. Henderson, G.B. Appetecchi, S. Passerini, NMR investigation of ionic liquid-LiX mixtures: Pyrrolidinium cations and TFSI anions, J. Phys. Chem. B. 109 (2005) 22814–22819. https://doi.org/10.1021/jp053799f.

[39] O. Brihuega-Moreno, F.P. Heese, L.D. Hall, Optimization of diffusion measurements using Cramer-Rao lower bound theory and its application to articular cartilage, Magn. Reson. Med. 50 (2003) 1069–1076. https://doi.org/10.1002/mrm.10628.

[40] I. V Koptyug, D.R. Sagdeev, E. Gerkema, H. Van As, R.Z. Sagdeev, Solid-state 27 Al MRI and NMR thermometry for catalytic applications with conventional (liquids) MRI instrumentation and techniques, 175 (2005) 21–29. https://doi.org/10.1016/j.jmr.2005.03.005.

Chapter 6

Discussion

6.1. Introduction

In the previous chapters, NMR techniques for the non-invasive characterization of mass transport in porous media, in particular for gases were developed and optimized. Accordingly, the optimized NMR methods were applied to determine local velocity fields, molecular diffusion, dispersion, and finally temperature. It is worth mentioning that the measuring techniques were developed and/or optimized based on practical demands in the field of reaction engineering. The results of the investigations allowed us to determine vital engineering parameters and support numerical simulations for gas phase heterogeneously catalyzed systems, such as hydrogenation of ethylene or methanation reaction.

It was successfully shown that NMR can measure molecular diffusion coefficient, chemical composition, and the velocity fields of gases and liquids in the monolithic structures. Based on the aim of the project, three measurement packages using optimized pulse sequences were successfully developed, namely:

- Investigation of the gas displacement using an optimized PFG-STE pulse sequence in monolithic structures to show the window size effect on molecular diffusion and/or dispersion of gases in porous ceramics
- Gas flow measurement using an optimized phase-contrast MRI sequence and validation of CFD simulations

- Localized determination of temperature in catalyst beds in a broad temperature range using DW-MRI sequences

In each measurement package, some aspects can still be improved to acquire more data on porous samples and fluids inside the samples. In the following sections, some of these points are discussed.

6.2. Temperature measurements

Localized determination of temperature in catalyst bed within operating systems (reactors) at high temperature conditions using MRSI and DW-MRI sequence were described in Chapter 5. The obtained SNR in DW-MRI allowed a more precise analysis of temperature compared to MRSI method, in particular for regions with low B_0 homogeneity. A more exhaustive analysis on the comparison between both methods is given below.

6.2.1. Temperature measurement using MRSI

In this project, the capillaries with inner diameters of 0.55 mm were inserted along the total length of the catalyst in order to show a complete spatially resolved temperature profile along the catalyst bed.

Peak analysis of the chemical shift differences was used for the determination of temperature for ethylene glycol and glycerol samples as potential NMR thermometers in MRSI studies. The results of an MRSI measurement for an arbitrary slice of NMR thermometers are depicted in Fig. 6.1. Since the spectral peaks of glycerol overlap one another more than ethylene glycol peaks, the latter material is a more suitable candidate for MRSI measurements in NMR thermometry (see Fig. 6.1). The applied temperature measurements by MRSI for ethylene glycol rely on chemical shift difference of –OH and $–CH_2$ signals of probing materials in NMR thermometers. For ethylene glycol, the temperature of the region of interest can be determined using Eq. 6.1, which relates the chemical shift difference $\Delta\delta$ (in ppm) and the temperature T:

$$T(°C) = 192.85 - 101.64\ \Delta\delta \tag{6.1}$$

The upper part illustrates selected spectra in the catalyst bed and is followed by one spectrum for an arbitrary volume element from the four probing capillaries, (a) to (d).

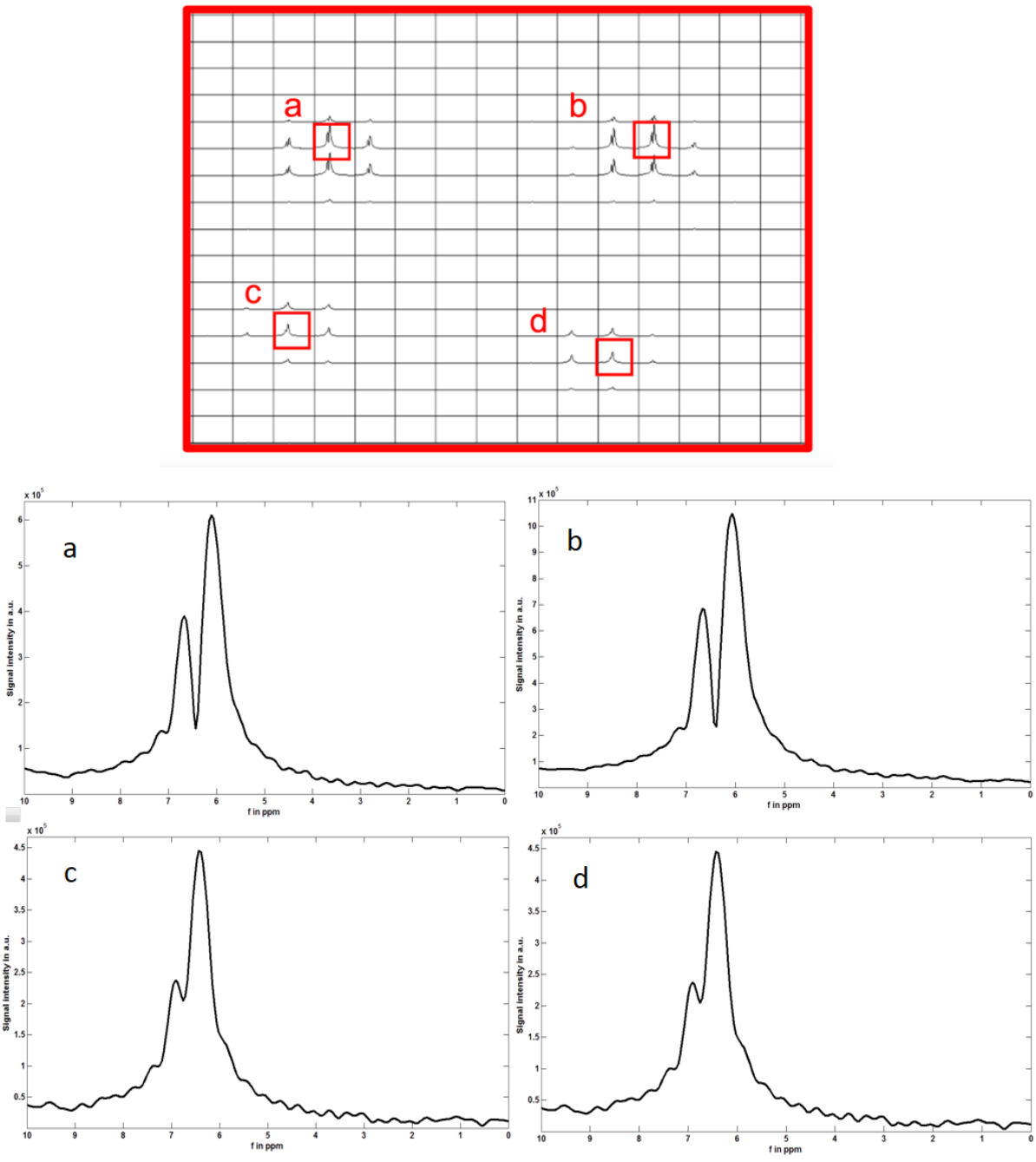

Figure 6.1. MRSI spectra obtained from the magnitude of the signal in the catalyst bed. Spectra (a) and (b) of ethylene glycol and (c) and (d) glycerol capillaries.

6.2.2. Comparison DW-MRI and MRSI

A comparison between temperature measurements by DW-MRI and MRSI is illustrated in the table below (Fig. 6.2). The figure includes corresponding slices measured with both methods at the same temperature (~74 °C). The DW-MRI images display the three NMR thermometers inserted in a monolithic structure (honeycomb), as described in Chapter 5. The DW-MRI images are generated using four equidistant diffusion weighting steps (Δb = 2000 s·mm^{-1}) starting with 50 s·mm^{-1}. Beside the DW-MRI images, the signal intensities of the ethylene glycol capillary are plotted versus *b*. In addition, a simple exponential function is fitted to the data to determine the diffusion coefficients, where R^2 describes the fit quality. Spectra of the ethylene glycol capillary measured by MRSI method at the same slice position is plotted in the right column to compare both methods.

The figure represents three different situations that may be encountered in the measurement of NMR thermometers using DW-MRI and MRSI. In the slices *a* to *d* both methods show good performance where the capillary is perfectly filled with ethylene glycol. The MRSI spectrum shows sharp peaks from (-OH) and (-CH_2) groups. Similarly, DW-MRI images measured and the fitted curves show high values of signal intensity ~ (6-7×10^8) at low diffusion weighting (b-value). The fitted curve to DW-MRI data shows a high coefficient of determination ($R^2 > 0.99$) for all four slices as well. The determined diffusion coefficients are reliable and in very good agreement with diffusion coefficient (D = 4.37×10^{-4} mm²·s^{-1}) obtained at the same temperature from the diffusion-temperature curves in the literature (cf. Fig. 5.6 in Chapter 5).

In the slices *e* and *f* where the NMR thermometer is only partially filled, the obtained signal intensities at low b-value are three or four times lower. However, the reduced signal intensity does not influence the quality of the analysis performed by DW-MRI, where diffusion coefficients D = 4.41×10^{-4} mm²·s^{-1} and D = 4.23×10^{-4} mm²·s^{-1} are obtained for slices *e* and *f*, respectively. The measured diffusion coefficients show the reliability of the method in these cases demonstrating that DW-MRI is less susceptible to magnetic field inhomogeneities compared to MRSI. While correct diffusion coefficients are determined by DW-MRI, MRSI fails to give ethylene glycol spectra in

both slices (*e* and *f*). The spectra are rather unreadable as a result of the higher dependency of MRSI on the spatial homogeneities of the magnetic field. Finally, for nearly empty parts of the ethylene glycol capillary (slices *g* and *h*), the fit quality (R^2) is drastically reduced for the DW-MRI data, and consequently, unreliable diffusion coefficients are obtained. In parallel, MRSI fails to determine the spectra of ethylene glycol. Thus, the quality of the fitted curve in DW-MRI plays a decisive role in the reliability of the obtained diffusion coefficients. In the upcoming studies, this fact should be considered in more detail to avoid systematic errors and ensure reliable temperature measurements by DW-MRI, particularly if an automatic data evaluation is applied.

Slice	**DW-MRI images**	**DW-MRI data (signal versus b-value) and fitted curve**	**Corresponding MRSI spectrum for the same slice position**
a	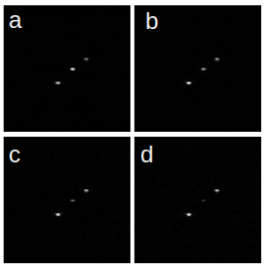	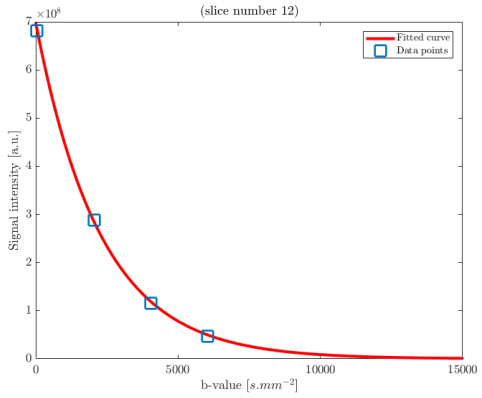 $R^2 = 1.000$ $D = 4.37 \times 10^{-4}\ \mathrm{mm^2 \cdot s^{-1}}$	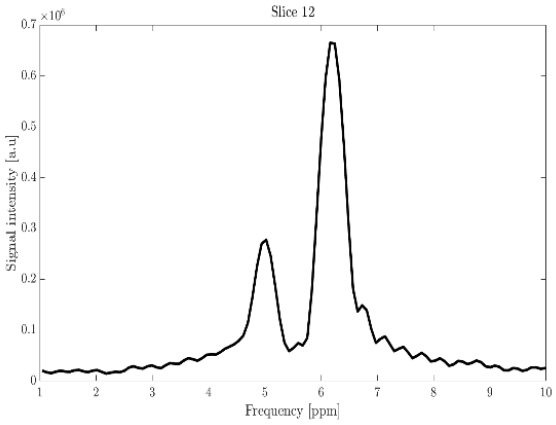

b	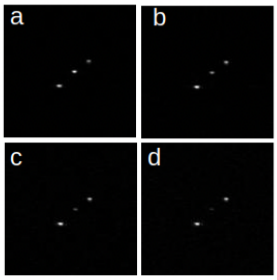	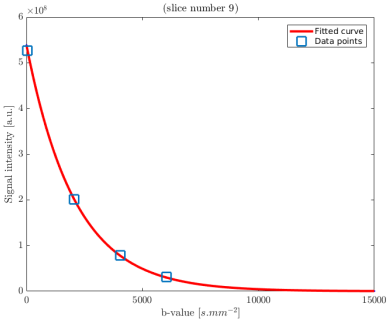 $R^2 = 1.000$ $D = 4.50 \times 10^{-4}\ \mathrm{mm^2 \cdot s^{-1}}$	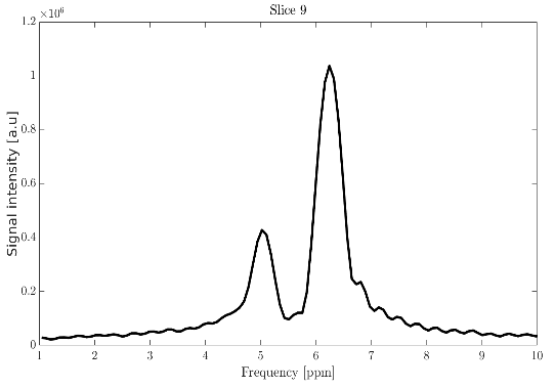
c	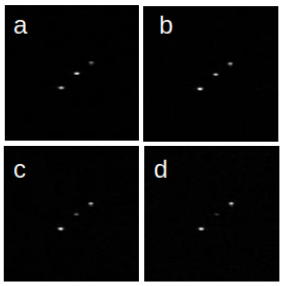	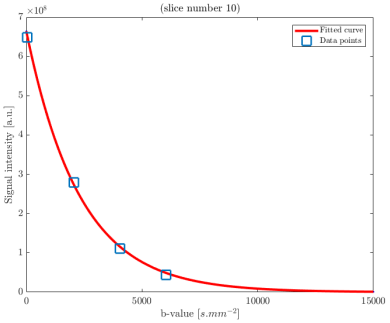 $R^2 = 0.999$ $D = 4.33 \times 10^{-4}\ \mathrm{mm^2 \cdot s^{-1}}$	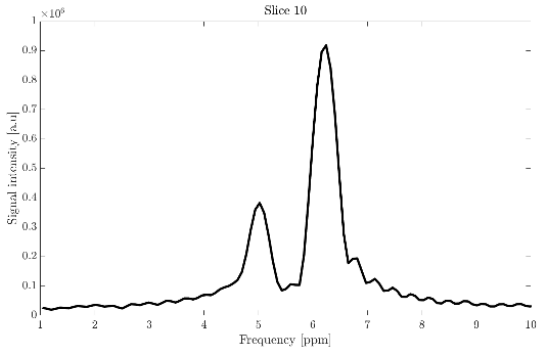
d	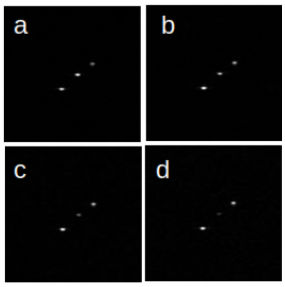	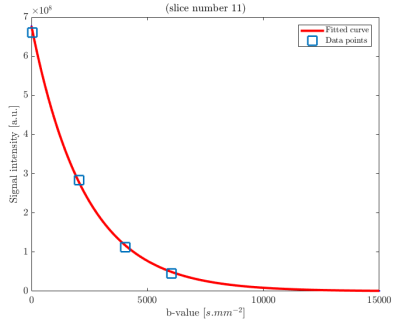 $R^2 = 0.999$ $D = 4.33 \times 10^{-4}\ \mathrm{mm^2 \cdot s^{-1}}$	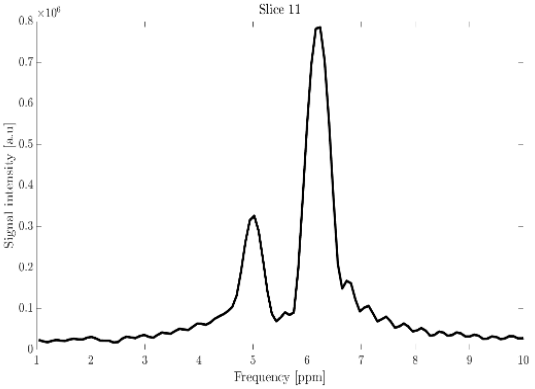

e	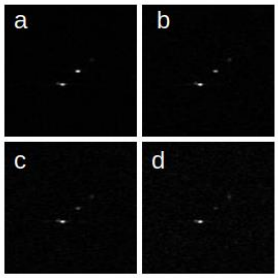	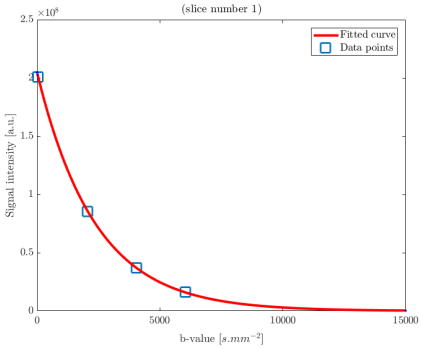 $R^2 = 1.000$ $D = 4.23 \times 10^{-4}\ mm^2 \cdot s^{-1}$	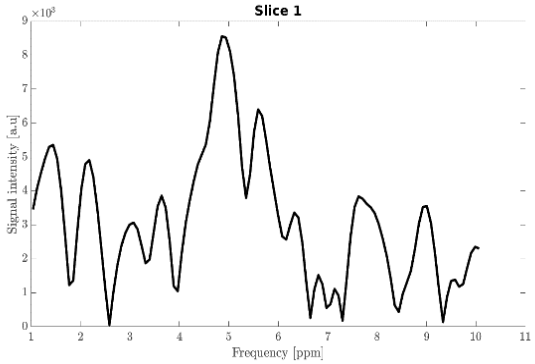
f	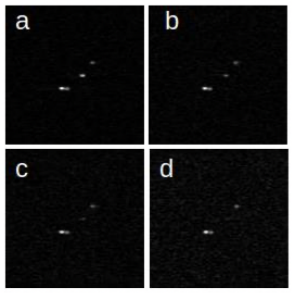	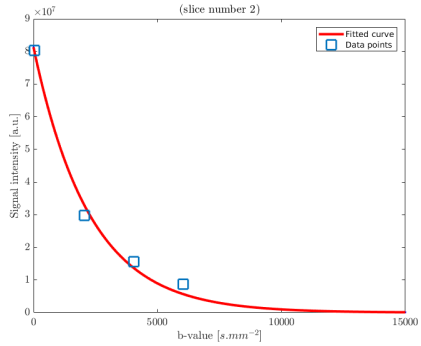 $R^2 = 0.993$ $D = 4.41 \times 10^{-4}\ mm^2 \cdot s^{-1}$	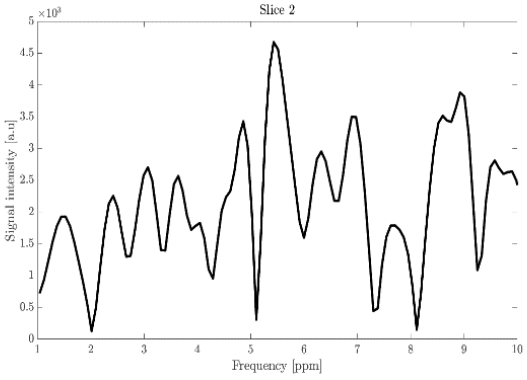
g	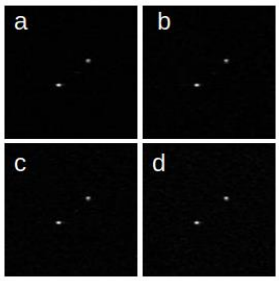	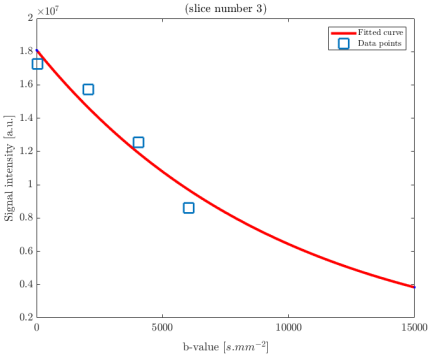 $R^2 = 0.926$ $D = 1.02 \times 10^{-4}\ mm^2 \cdot s^{-1}$	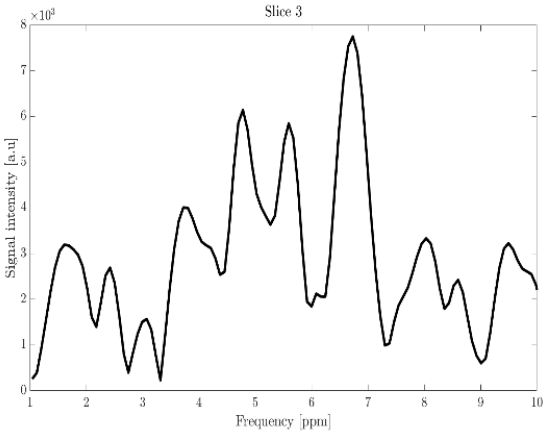

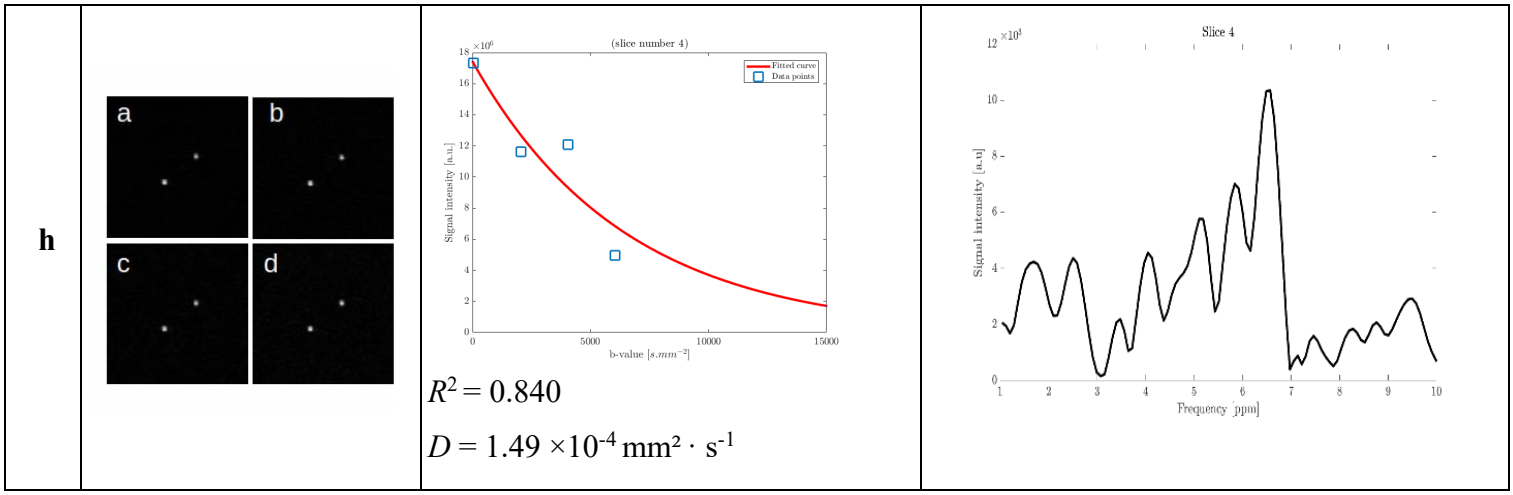

Figure 6.2. Comparison of DW-MRI data and MRSI results.

6.3. Local velocity, diffusion and dispersion coefficient measurements: Limitations and outlook for further studies

6.3.1. Phase-contrast imaging

Optimized spin echo-based MR velocimetry (SE-MRV) and PFG-STE sequences were used to measure flow, diffusion, and dispersion of single hydrogen containing gases in monolithic structures. The single spin-echo MRV pulse sequence is being applied as the simplest MRV method because multi-echo pulse sequences suffer from stronger signal decay due to relaxation and diffusion losses. The results of NMR data were compared with CFD simulations and showed very good agreement. The simplified model used to optimize the MRV measurement estimates the effects of transversal relaxation and molecular diffusion. The maximum observation time of the velocity encoding is linearly dependent on *TE*. The signal behaves in two ways, more diffusion weighting (for a given *b*-value) for a small Δ and more T_2 relaxation weighting for a large Δ. Thus, according to this model, an optimal observation time for flowing gas in the steady-state system is being used.

One of the limiting factors in the gas flow measurements were still the low SNR for a precise comparison of the numerical solutions with MRV data. Besides, the reported velocities at the solid-gas interface need to be more investigated. Further improvements

for increasing SNR obtained in the phase-contrast imaging for gas flow measurements of thermally polarized gas using optimized MRV sequences is also one of the aspects that can be considered for further method developments. To this end, special phase reconstruction algorithms may be implemented to better distinguish phase-change related velocity encoding. A recently published algorithm may help to improve the evaluation of the obtained velocity fields for gas flow more accurately [1]. Such joint frameworks for flow estimation, magnitude reconstruction, and segmentation from undersampled velocity-encoded MRI data lead to accurate visualization of flow velocity fields in porous samples, in particular in gas-solid systems.

6.3.2. Diffusion and dispersion coefficient measurements

The investigation of the displacement function of gas in monolithic structures showed window size effect on molecular gas diffusion in porous ceramics using an optimized PFG-STE pulse sequence. However, the investigation of the propagators of single thermally polarized gases within commercial monolithic catalyst supports may be performed for multiple gases in order to characterize the diffusion process and the structure of catalysts. In the future methodological developments, pore-scale analysis of axial and radial dispersion coefficients of gases such as CH_4/H_2 or CH_4/water in foam catalyst supports using NMR *q*-space imaging may reveal more information on the interaction of gases with the pore walls and between gases. For further investigations, the development of fast MRSI methods for spatially resolved determination of the concentration of substances in gas phase reactions can play a supporting role, as MRSI can measure the concentration of species in a certain volume of interest (VOI) quantitively.

Another limiting factor is the low SNR achieved in local measurements with smaller VOIs. Although the local measurements of gas diffusion have answered important questions about gas mass transport in foams, the method will reveal more information if it could be applied for smaller VOIs.

References

[1] V. Corona, M. Benning, L.F. Gladden, A. Reci, A.J. Sederman, C.-B. Schoenlieb, Joint phase reconstruction and magnitude segmentation from velocity-encoded MRI data, (2019) 1–22. http://arxiv.org/abs/1908.05285.

Chapter 7

Outlook

7.1. MRI of Multiphase systems in porous media

The *in situ* analysis of multiphase flows in porous ceramics can address critical questions on mass transport of flow in such complex systems. However, particular methodological developments need to be considered to perform measurements that are fast enough to follow rapid changes of flow in porous media in spatio-temporal investigations. In addition, improvements of SNR, which result in better segmentation between different phases, seem necessary. The methodological developments may, therefore, consist of both optimization of MRI sequences as well as data processing techniques such as the compressed sensing approach [1].

Some attempts were performed to measure stationary two-phase system of water and medium-chain triglycerides (MCTs) oil. Top left in Fig. 7.1 shows the MRI image obtained using a FLASH sequence with a TR of 100 ms, a TE of 2 ms, a flip angle of 15°, and a slice thickness of 2 mm. Using the read gradient in the x-direction and a bandwidth of 200 kHz, only a small chemical shift artifact between oil and water can be seen. The top right image shows the same sample using TR/TE (100 ms / 2 ms), FA = 90° (partial saturation of water due to longer T_1 relaxation time than for MCT oil). The bottom left in Fig. 7.1 shows the result of the same imaging sequence using a TR of 100 ms, a TE of 2 ms, and a flip angle of 15°. However, as pre-saturation on the MCT oil signal was applied, mainly water can be seen. On the other hand, bottom right shows

the FLASH image using TR/TE (100 ms / 2 ms), and a FA of 15°, with pre-saturation on water, i.e., the MCT oil is mainly observed.

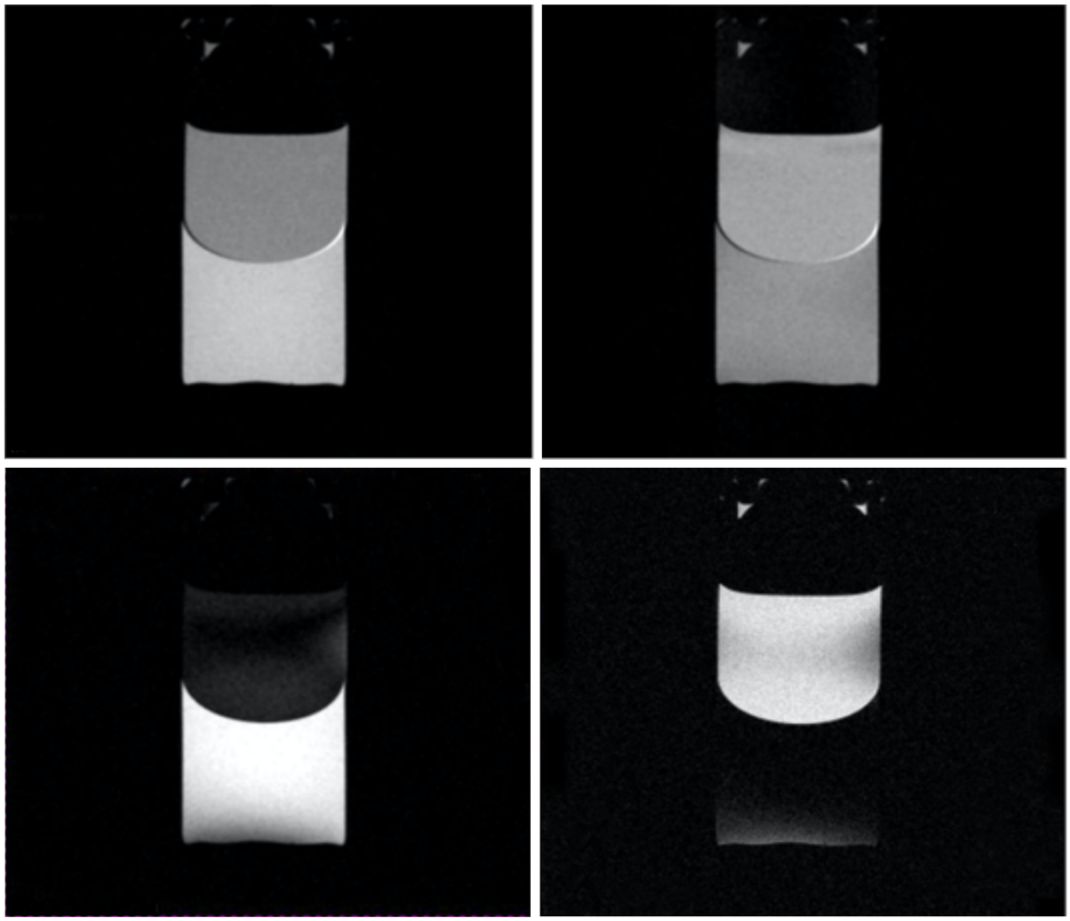

Figure 7.1. FLASH measurements performed for a tube phantom filled with MCT oil (top) and water (bottom) aiming at a suitable visualization of the interface between both liquids.

Although the preliminary results are promising, still considerable modifications are required to perform such measurements for two-phase liquid flow in porous media. On the other hand, the results can be compared to numerical simulations performed with Lattice Boltzmann (LB) or other CFD methods in order to validate numerical predictions of flow field behavior in porous media. The preliminary results were promising and showed that further work can be performed for more complex systems.

Previously and as the first step, single-phase flow simulations were validated by NMR results in order to show the feasibility of the method for investigating mass transport in simple tubes or macroscopic open-cell foams. An example of the obtained data is given in Fig. 7.2. As the second stage, non-Newtonian single-phase flows were also investigated using MRV and LB methods. The LB simulations were performed by Alex Schulz at the Leibniz-Institut für Werkstofforientierte Technologien (IWT) in the Production Engineering Department. The numerical solution for Xanthan was modeled using the power law model suggested by Ostwald and de Waale [2]. In the model, the viscosity μ is a function of the shear rate ($\mu = m\,\gamma^{n-1}$). The power law function was fitted against the viscometer measurements, resulting in m = 0.2 and n = 0.39. The analytical solution for a Newtonian flow behavior (n = 1) is also added in Fig. 7.2a. In future work, two-phase flow will be investigated in porous media numerically and experimentally using LB and MRV, respectively.

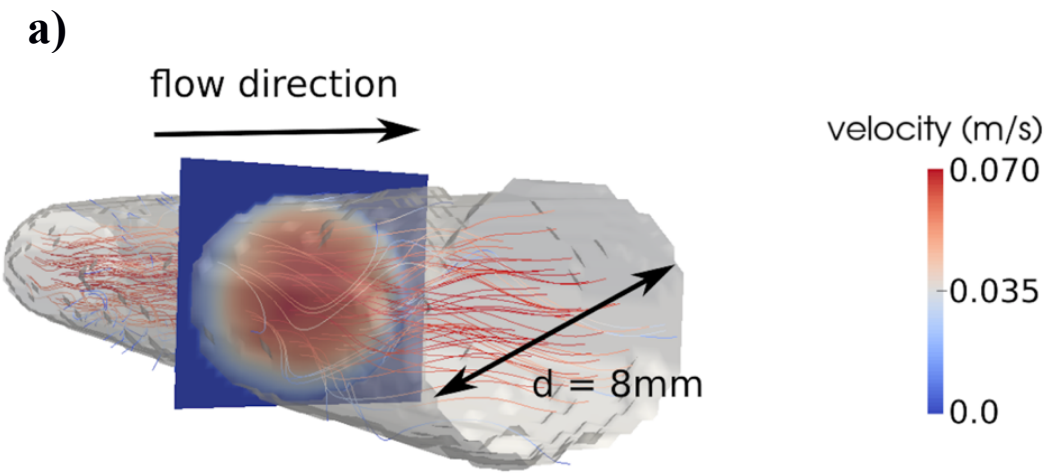

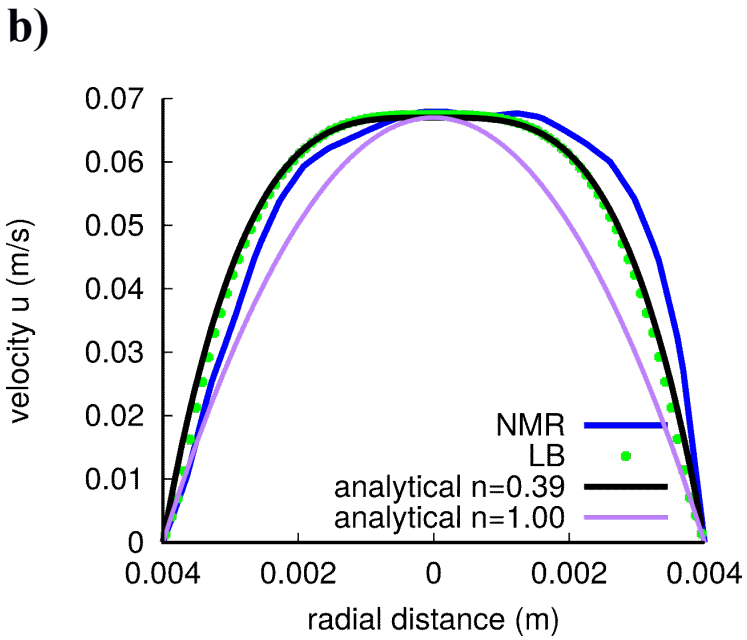

Figure 7.2. (a) Flow NMR measurement of a non-Newtonian liquid in a circular pipe (b) Comparison of LB simulations and MRV for non-Newtonian flow in a tube. LB simulations were performed using a power-law model, $\mu = m\,\gamma^{(n-1)}$ with m = 0.2 Pa s^n and n = 0.3.

7.2. Relaxometry and diffusion analysis for methanation of CO_2

According to the project plans, the author of this thesis had a visit to the Chemical Engineering and Analytical Science School at the University of Manchester in 2018. The primary purpose of the visit was to carry out collaborative research using the magnetic resonance facilities at the University of Manchester to explore new methods for characterizing mass transport properties such as diffusion in porous materials and catalysts. During the visit, relaxometry techniques for the local and non-invasive characterization of heterogeneous catalysts, using low field NMR systems were conducted. The following section presents some results achieved during this visit and plans for more investigation on NMR relaxation times in catalyst pellets used in methanation reaction.

Using relaxation measurements, it can be investigated how the molecular dynamics in porous systems are associated with the bulk phase. This can then be related to the strength of surface interactions. Therefore, the techniques are useful when one wants to quantify interactions of reactants, products, and solvents and see how they relate to chemical reactions. They can also be used to investigate changes in catalyst surface due to chemical treatments, poisoning, or degradation.

Since NMR relaxation times T_1 and T_2 are sensitive to the surrounding environment of the molecules, for instance pores in catalyst pellets, they can be used to characterize molecular dynamics in supported catalysts. Different porous structures yield different relaxation properties based on surface chemistry, pore size, the extent of pore saturation, and the concentration of paramagnetic species (if available) in the pores. Therefore, by measuring T_1 and T_2 in heterogeneous catalysts, one can correlate the structure exposed to certain materials acting as reactant or product in order to obtain useful information on their interactions with catalyst pores or even between the species [3,4]. In this ongoing research project, NMR relaxometry is used to answer questions about the effect of washcoat on the yield of methanation reaction. The methanation reactions were performed in a temperature range of 200-400 °C using two supported catalysts with different catalyst loadings. The conversation rates versus temperature are illustrated in Fig. 7.3. A higher reaction rate is achieved for the samples with 2 w% compared to 0.5 w% Ru.

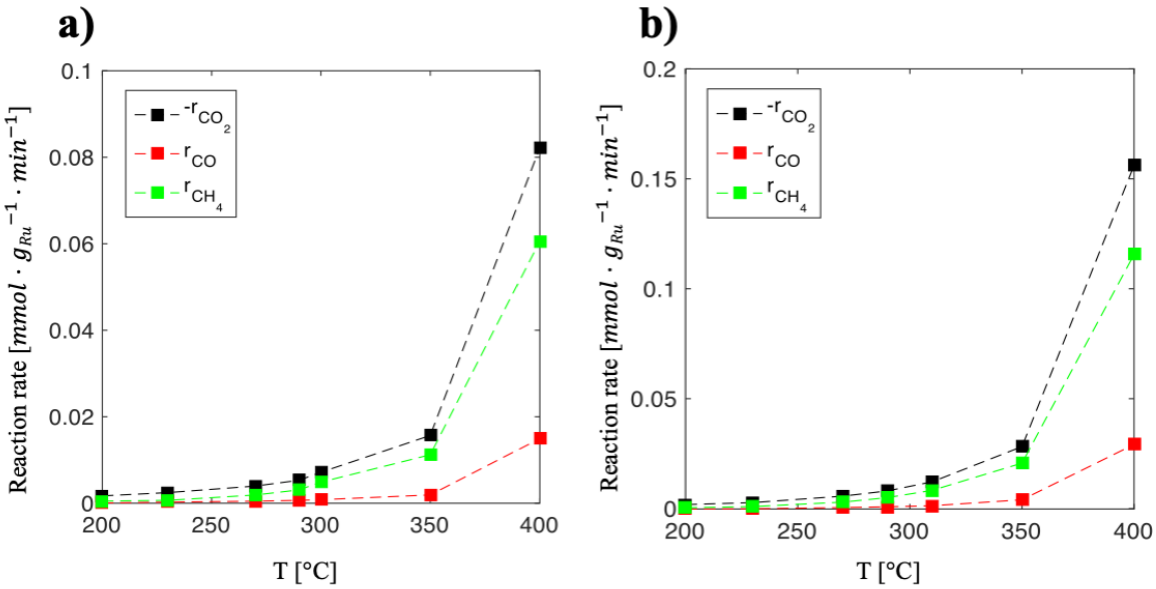

Figure 7.3. Rate of methanation reaction performed using two identical pellets with (a) 0.5 w% and (b) 2.0 w% washcoat of Ru catalyst.

NMR relaxometry was performed for both samples to investigate the effect of washcoat on NMR relaxation times. Table 7.1 shows the measured T_1 and T_2 for catalyst pellets with 0.5 w% and 2.0 w% catalyst loadings.

A Magritek Spinsolve benchtop NMR spectrometer with an operating frequency of 43 MHz (^{1}H) was used for the relaxation time measurements. The NMR system is shown in Fig. 7.4. Prior to the measurements, pores of the pellets were saturated using distilled water as probing liquid. The pellet catalysts were inserted into 5 mm laboratory tubes. Afterward, the tubes were sealed (see Fig. 7.4) to maintain the initial water content of the samples during the measurements as the data of the measurements were reproduced after several days. To ensure that the moisture within the samples remains unchanged, a 1D ^{1}H sequence consisting of a single 90° excitation pulse was used to record the spectra of water inside samples before and after performing all the relaxation time measurements.

A standard Inversion Recovery (IR) pulse sequence was implemented for T_1 measurements. The IR sequence is illustrated in Fig. 7.5b. Different time delays were set according to the longitudinal relaxation time of the bulk allowing the full coverage

of T_1 recovery. In these measurements, a 180° pulse with a duration of 18 µs was applied to invert the magnetization. Afterward, 90° (9 µs) excitation pulses were applied in α = 41 steps. TR was set to 4 s, and the TE was 1 ms. The total acquisition time for the measurement was 337.2 s. The maximum inversion time was 2 s.

A standard Carr-Purcell-Meiboom-Gill (CPMG) sequence was used for T_2 measurements. A schematic of the pulse sequence is presented in Fig. 7.5b. In the CPMG sequence, a 90° (9 µs) pulse was followed by 180° (20 µs) pulses with a constant time delay (t). T_2 measurements were performed using a total number of 20 steps and 150 echoes per each step. TR was 8.5 s, and TE was minimized to a constant value of 100 µs in order to avoid artifacts and loss of signal due to diffusion of molecules during T_2 measurement echo time.

Figure 7.4. Magritek Spinsolve 43 benchtop NMR spectrometer used for relaxation time measurements (left). The pellet catalysts were measured in 5 mm NMR tubes (right).

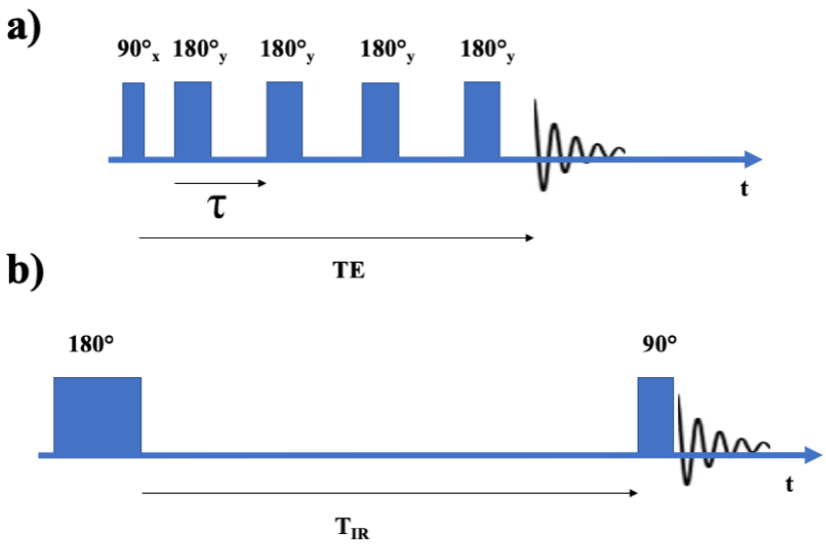

Figure 7.5. (a) CPMG pulse sequence for T_2 measurements, (b) Inversion recovery sequence for T_1 measurements.

The results of relaxation time measurements are given in Table 7.1. The samples with more percentage of Ru also have longer T_1 and shorter T_2 relaxation times in both oxidized and reduced (not shown in Table 7.1) samples. Additional investigation is planned to obtain more information on the pellet catalysts. For instance, Scanning Electron Microscope (SEM) measurements can show the distribution of Ru washcoat in the internal surface area of the pores. The effect of adsorption should also be investigated to relate obtained relaxation times to the reaction performance. In case that plausible results are achieved, the relaxation time measurements can be used as a powerful toolkit for investigating micro-meso properties of supported catalysts. Furthermore, a T_1/T_2 correlation with the reaction rate of methanation reaction can be used as an evaluation parameter in preparation and fabrication of supported catalysts to describe and assess the quality of the coating method in a quantitative way.

Table 7.1. Measured relaxation times for oxidized pellet catalysts with 2% and 0.5 wt% Ru.

Sample	T_1 **(ms)**	T_2 **(ms)**	T_1/T_2
2 w% Ru	339	11.76±0.01	28.81
0.5 w% Ru	280	12.51±0.02	22.38

References

[1] J.D. Cooper, A.P.E. York, A.J. Sederman, L.F. Gladden, Measuring velocity and turbulent diffusivity in wall-flow filters using compressed sensing magnetic resonance, Chem. Eng. J. (2019) 119690. https://doi.org/10.1016/j.cej.2018.08.076.

[2] R.B. Bird, R.C. Armstrong, O. Hassager, Dynamics of polymeric liquids. Volume 1. Fluid mechanics., (1977). https://doi.org/10.1016/0377-0257(78)80009-3.

[3] C. D'Agostino, M.D. Mantle, L.F. Gladden, Inhibitory effect of oxygenated heterocyclic compounds in mesoporous catalytic materials: A pulsed-field gradient NMR diffusion study, Microporous Mesoporous Mater. 269 (2018) 1–5. https://doi.org/10.1016/j.micromeso.2017.02.033.

[4] C. D'Agostino, J. Mitchell, L.F. Gladden, M.D. Mantle, Hydrogen bonding network disruption in mesoporous catalyst supports probed by PFG-NMR diffusometry and NMR relaxometry, J. Phys. Chem. C. 116 (2012) 8975–8982. https://doi.org/10.1021/jp2123295.

Acknowledgment

I would like to express my deep and sincere gratitude to PD Dr. Wolfgang Dreher for his unsparing support in all steps of this project. Indeed, it was a great opportunity to be a member of his research group. He provided me with invaluable guidance during the project. I appreciate him for giving me the chance to feel free to express my ideas and follow them to solve open questions on mass transport in porous media.

I would like to sincerely extend my heartful thanks to Professor Jorg Thöming for his advice and supports on this work. It was my privilege to have the chance to discuss my ideas and the obtained results with him. I was always sure that there is an open door to discuss my plans and get valuable feedback to improve the project.

I would like to thank Dr. Eckehard Küstermann, who helped me quickly learn more about NMR physics in the first year of my project, also for his supports in helping me learn German language as my office mate! I would also like to thank him for his friendship and great sense of humor in our coffee breaks!

I would like to thank Dr. Peter Erhard for his comments on the text of my papers.

I am extending my thanks to Prof. Rezwan for his constant encouragement and management in keeping up this project in the research training group MIMENIMA. I also appreciate Dr. Michaella Wilhelm, the coordinator of MIMENIMA, for her supports in conducting this research.

My Special thanks go to my colleagues, Jan Ilsemann, Harm Ridder, Mehrdad Sadeghi, Alex Schulz, Thomas Ilzig, M.D Nurul Karim, and Adrian Ricke. Especially, I thank Mehrdad and Harm for the sleepless nights we were working together to reach deadlines, find solutions, and have fun together among performing experiments and data evaluation. I thank my fellow lab-mate, Dr. Felizitas Wermter in ‘in-vivo-MR’ group for stimulating discussions and sharing her ideas on my work.

I am very much thankful to my wife Saeedeh for being there for me all the time, for her love, understanding, prayers, and support to complete this research work. Thanks for being the most beautiful part of my life. All the moments we spend together are the best of mine. In particular, these memorable moments that we are waiting for our tiny gift from God. I am sure our baby will be proud to have such a great mother. The greatest love, the greatest mother and the greatest friend ever… I love you...

I am extremely grateful to my parents for their love, prayers, caring, and sacrifices for educating and preparing me for my future.

Finally, my thanks go to all the people who have supported me to complete the research work directly or indirectly.

Publications presented in this work

Author Contributions

• Publication presented in chapter 1

1. Oummadi, S., Nait-Ali, B., Alzina, A., Victor, J. L., Launay, Y., **Mirdrikvand, M.**, ... & Smith, D. S. (2019). Distribution of water in ceramic green bodies during drying. *Journal of the European Ceramic Society*, *39*(10), 3164-3172.

Author	Contribution
Siham Oummadi	Concept and planning of work, design and construction of the experimental setup, preparation of green body samples, data analysis and interpretation, manuscript preparation (design, editing, and writing the manuscript)
Benoit Nait-Ali, Arnaud Alzina, Jean-Louis Victor, Yann Launay	Discussed the plausibility of the obtained data, edited the manuscript
Mojtaba Mirdrikvand	Performed ZTE measurements, helped in writing NMR-related section in the manuscript
Wolfgang Dreher	Development and supervision of ZTE measurements, edited the manuscript
Kurosch Rezwan	Discussed the data, edited the manuscript
David S. Smith	Supervision of the topic, advice and discussed the data; edited the manuscript

• Publication presented in chapter 2

2. **Mirdrikvand, M.**, Ilsemann, J., Thöming, J., & Dreher, W. (2018). Spatially Resolved Characterization of the Gas Propagator in Monolithic Structured Catalysts Using NMR Diffusiometry. *Chemical Engineering & Technology*, *41*(9), 1871-1880.

Author	Contribution
Mojtaba Mirdrikvand	Concept and planning of work, design and construction of the experimental setup, preparation of samples and catalysts, development and validation of diffusion measurement method, NMR experiments, data analysis and interpretation, manuscript preparation (design, editing, and writing the manuscript)
Jan Ilsemann	Preparation of catalysts, edited the manuscript
Jorg Thöming	Conceptual advice and discussed the plausibility of the obtained data, edited the manuscript
Wolfgang Dreher	Supervision of the development of the PFG-STE method and experiments, advice and discussed the data; edited the manuscript

• Publication presented in chapter 3

3. **Mirdrikvand, M.**, Sadeghi, M., Karim, M. N., Thöming, J., & Dreher, W. (2020). Pore-scale analysis of axial and radial dispersion coefficients of gas flow in macroporous foam monoliths using NMR-based displacement measurements. *Chemical Engineering Journal*, *388*, 124234.

Author	Contribution
Mojtaba Mirdrikvand	Concept and planning of work, design and construction of the experimental setup, preparation of samples and catalysts, development and validation of diffusion measurement method, NMR experiments, data analysis and interpretation, manuscript preparation (design, editing, writing)
Mehrdad Sadeghi	Performed related simulations, edited the manuscript
M. Nurul Karim	Helped in data analysis, edited the manuscript
Jorg Thöming	Conceptual advice and discussed the plausibility of the obtained data, edited the manuscript
Wolfgang Dreher	Supervision of the displacement measurement experiments, advice and discussion about the data, edited the manuscript

• Publication presented in chapter 4

4. Sadeghi, M., **Mirdrikvand, M.**, Pesch, G., Dreher, W., Thöming, J. Full field analysis of gas flow within open cell foams: comparison of microtomography-based CFD simulations and experimental MRV flow mapping data, *Experiments in Fluids* (*in press*)

Author	Contribution
Mehrdad Sadeghi	Conceptual design of the cross-validation of CFD and MRV methods, performed CFD simulations, manuscript preparation (design, editing, and writing the manuscript)
Mojtaba Mirdrikvand	Planning of experimental work, design and construction of the experimental setup, performed flow measurements, data analysis and interpretation, helped in writing some part of the manuscript
Georg Pesch	Data analysis, discussed the plausibility of the obtained data, edited the manuscript
Wolfgang Dreher	Supervision of the project, discussed the data, edited the manuscript
Jorg Thöming	Conceptual advice and discussed the plausibility of the obtained data, edited the manuscript

5. Sadeghi, M., Thöming, J., Dreher, W., **Mirdrikvand, M.**, MRV and CFD of gas flow through regular monolithic structures with emphasis on dispersion and maldistribution (*in preparation*).

Author	Contribution
Mojtaba Mirdrikvand	Concept and planning of work, design and construction of the experimental setup, preparation of samples and catalysts, development and validation of diffusion measurement method, NMR experiments, data analysis and interpretation, manuscript preparation (design, editing, and writing the manuscript)
Mehrdad Sadeghi	Performed CFD simulations for honeycomb samples, edited the manuscript
Jorg Thöming	Conceptual advice and discussed the plausibility of the obtained data, edited the manuscript
Wolfgang Dreher	Supervision of the development of the displacement measurement experiments, advice and discussed the data; edited the manuscript

• Publication presented in chapter 5

6. **Mirdrikvand, M.**, Ridder, H., Thöming, J., & Dreher, W. (2019). Diffusion weighted magnetic resonance imaging for temperature measurements in catalyst supports with an axial gas flow. *Reaction Chemistry & Engineering*, *4*(10), 1844-1853.

Author	Contribution
Mojtaba Mirdrikvand	Concept and planning of work, preparation of samples and catalysts, development and validation of DW-MRI method, NMR experiments, automatic data analysis and interpretation of the data, manuscript preparation (design, editing, and writing the manuscript)
Harm Ridder	Design and construction of the experimental setup, Performed the measurements using the setup simultaneously with Mojtaba Mirdrikvand, edited the manuscript
Jorg Thöming	Conceptual advice and discussed the data, edited the manuscript
Wolfgang Dreher	Supervision and development of the temperature measurement experiments, advice and discussed the data; edited the manuscript

Other contributions at conferences as main or co-worker:

7. **Talk:** Spatially Resolved NMR Study of Regular and Irregular Ceramic Catalysts by Thermally Polarized Gas, **Mojtaba Mirdrikvand**, Wolfgang Dreher, *14th International ceramics congress*, June 10-14, (2018) Perugia, Italy.

8. **Talk:** NMR Imaging for Characterizing Mass Transport and Reaction Processes with Automatic Data Analysis, **M. Mirdrikvand**, W. Dreher, *MAPEX Informatics Material Symposium, September* (2017) Bremen, Germany.

9. **Talk:** NMR Methods for Operando Analysis of Heterogeneous Catalytic Processes, **M. Mirdrikvand**, W. Dreher, *5th Edition on Global Conference on Catalysis, Chemical Engineering & Technology*, Sep 16-18, (2019) London, United Kingdom.

As co-worker:

10. Full-field assessment of gaseous flow within open-cell foams: comparison of μCT-based CFD simulations and magnetic resonance velocimetry results, M. Sadeghi et al. *12th European Congress of Chemical Engineering*, Sep 16-18, (2019) Florence, Italy.

11. Spatial characterization of heterogeneously catalyzed gas phase reactions via operando NMR imaging methods, Ridder et al., *Jahrestreffen Reaktionstechnik*, (2018) Würzburg, Germany.

12. Profiles of temperature, velocity and gas composition - matching operando MRI measurements and simulation, Ridder et al., *Catalysis Conference*, (2019) Houston, USA.

Versicherung an Eides Statt

Ich, Mojtaba Mirdrikvand, wohnhaft Hoffmanns Park 12, 28355 Bremen

versichere an Eides Statt durch meine Unterschrift, dass ich die vorstehende Arbeit selbständig und ohne fremde Hilfe angefertigt und alle Stellen, die ich wörtlich dem Sinne nach aus Veröffentlichungen entnommen habe, als solche kenntlich gemacht habe, mich auch keiner anderen als der angegebenen Literatur oder sonstiger Hilfsmittel bedient habe.
Ich versichere an Eides Statt, dass ich die vorgenannten Angaben nach bestem Wissen und Gewissen gemacht habe und dass die Angaben der Wahrheit entsprechen und ich nichts verschwiegen habe.
Die Strafbarkeit einer falschen eidesstattlichen Versicherung ist mir bekannt, namentlich die Strafandrohung gemäß § 156 StGB bis zu drei Jahren Freiheitsstrafe oder Geldstrafe bei vorsätzlicher Begehung der Tat bzw. gemäß § 161 Abs. 1 StGB bis zu einem Jahr Freiheitsstrafe oder Geldstrafe bei fahrlässiger Begehung.

Bremen, 22.04.2020
Ort, Datum Unterschrift

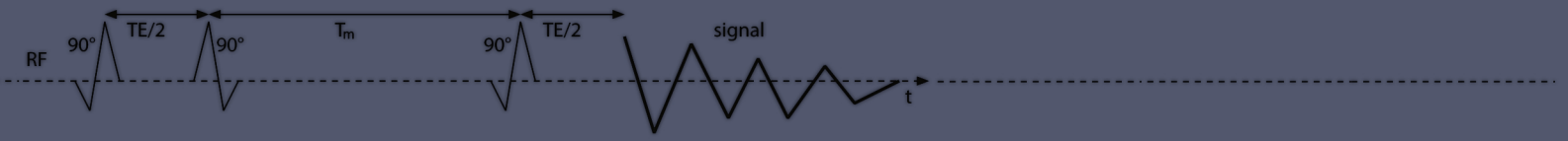
RF
90°
TE/2
90°
T_m
90°
TE/2
signal
t